



HAL
open science

Optical localization of multiple micro-conveyors mobile over smart surfaces

Saly Malak

► **To cite this version:**

Saly Malak. Optical localization of multiple micro-conveyors mobile over smart surfaces. Optics / Photonic. Université de Technologie de Compiègne, 2019. English. NNT : 2019COMP2526 . tel-03175889

HAL Id: tel-03175889

<https://theses.hal.science/tel-03175889v1>

Submitted on 21 Mar 2021

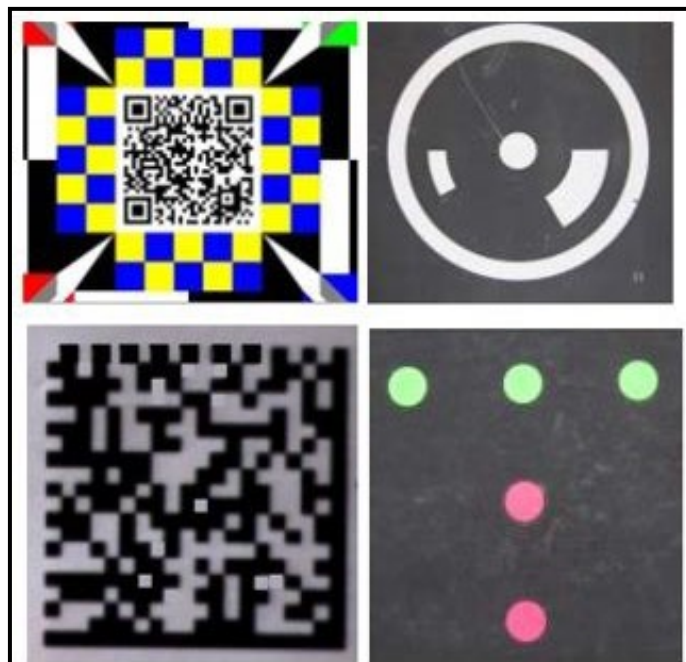
HAL is a multi-disciplinary open access archive for the deposit and dissemination of scientific research documents, whether they are published or not. The documents may come from teaching and research institutions in France or abroad, or from public or private research centers.

L'archive ouverte pluridisciplinaire **HAL**, est destinée au dépôt et à la diffusion de documents scientifiques de niveau recherche, publiés ou non, émanant des établissements d'enseignement et de recherche français ou étrangers, des laboratoires publics ou privés.

Par Saly MALAK

*Optical localization of multiple micro-conveyors
mobile over smart surfaces*

Thèse présentée
pour l'obtention du grade
de Docteur de l'UTC



Soutenue le 9 décembre 2019

Spécialité : Mécatronique, Photonique et Systèmes : Unité de
recherche en Mécanique - Laboratoire Roberval (FRE UTC -
CNRS 2012)

D2526

PhD
presented for the title of DOCTOR from
Université de Technologie de Compiègne

**Optical localization of multiple
micro-conveyors mobile over smart surfaces**

Saly Malak

Defended on December 09, 2019 in front of a jury composed of:

Reviewers	JULIEN-VERGONJANNE Anne	Université de Limoges anne.julien-vergonjanne@unilim.fr
	HEGGARTY Kevin	IMT Atlantique kevin.heggarty@imt-atlantique.fr
Examiners	LAURENT Guillaume	Institut Femto-st guillaume.laurent@femto-st.fr
	NACE Dritan	Université de Technologie de Compiègne dritan.nace@hds.utc.fr
Invited	FRACASSO Bruno	IMT Atlantique bruno.fracasso@imt-atlantique.fr
	DUPONT Erwan	Université de Technologie de Compiègne Erwan.dupont@utc.fr
Co-directors	AL HAJJAR Hani	Université de Technologie de Compiègne hani.al-hajjar@utc.fr
	LAMARQUE Frédéric	Université de Technologie de Compiègne Frédéric.lamarque@utc.fr

Contents

List of abbreviations	vii
1 State of art on the technology of the localization and tracking of mobile systems	11
1.1 Introduction	11
1.2 Localization and tracking applications	11
1.3 Localization and tracking methods	13
1.3.1 Proximity Detection	13
1.3.2 Triangulation	13
1.3.3 Scene analysis / fingerprints	18
1.4 Performance metrics	18
1.5 Localization and tracking systems	21
1.5.1 Macro-scale localization and tracking:	21
1.5.2 Micro-scale localization and tracking:	38
1.6 Conclusion	39
2 Modeling of the optical localization and tracking method	41
2.1 Introduction	41
2.2 System architecture for localization and tracking	42
2.2.1 Localization phase description	42
2.2.2 Tracking phase description	44
2.3 System modeling of the localization and tracking method	45
2.3.1 Dimensioning of the tracking system	49
2.3.2 Surface coverage	56
2.3.3 Sensitivity of the spot position to the angular variation of the mirror	57
2.4 Scanning phase	57
2.5 Photo-detector types and functionality	59
2.6 Conclusion	61
3 Validation of a closed loop tracking of a mobile micro-conveyor	63
3.1 Introduction	63
3.2 Micro-conveying Actuation Principles	63
3.3 Application of the optical system modeling	66
3.4 Control unit	70
3.4.1 QPD signals	71
3.4.2 Localization and tracking algorithm	72
3.4.3 MEMS mirror control	72
3.4.4 Micro-controller development environment	76

3.4.5	Labview interface	77
3.5	Experimental results	79
3.6	Conclusion	85
4	Closed loop tracking with the smart surface	87
4.1	Introduction	87
4.2	Significance of localization	87
4.3	Electromagnetic conveying surface principle	88
4.3.1	Actuation principle	88
4.3.2	Conveying surface architecture	89
4.4	Conveying surface calibration	90
4.4.1	Homography method	91
4.4.2	Homography matrix calculation	92
4.4.3	Homography applications	94
4.4.4	Vision system camera calibration	96
4.4.5	Optimization of homography matrix	98
4.5	Closed loop tracking of micro conveyor with electromagnetic surface	107
4.5.1	Control chain	107
4.5.2	Experimental results	108
4.6	Multiple micro-conveyors control	114
4.6.1	Time multiplexing method	115
4.6.2	Proof of concept	117
4.7	Conclusion	119
5	Application of the localization and tracking in macro-scale with an active reception system	121
5.1	Introduction	121
5.2	Optical communication system description	122
5.3	Pan-Tilt module (PTM) structure	123
5.4	Optical tracking module (OTM) description	124
5.5	Optical ray propagation model	124
5.6	Telescope block of the OTM	126
5.6.1	Modeling of the optical path and geometric equations	126
5.6.2	Simplified calculation of θ and T from the QPD voltages	128
5.6.3	Telescope control unit	129
5.6.4	Experimental setup of the telescope block	130
5.6.5	Experimental results of the telescope block	130
5.7	MEMS block of the OTM	134
5.7.1	Experimental prototype	134
5.7.2	Results of optical fiber injection during rotation and translation	136
5.8	Conclusion	139
6	Conclusion	141
	List of publications	147

List of Figures

1.1	Positioning based on AoA measurements in 2D example	14
1.2	Positioning based on ToA measurements in 2D example	16
1.3	Positioning based on TDoA measurements in 2D example	17
1.4	Classification of localization methods.	19
1.5	Accuracy vs precision of a system	20
1.6	Different Localization Systems.	22
1.7	(a) Active Bat vs (b) Cricket architecture	27
1.8	(a) Multiple LED 1 photodiode (PD) configuration [Erog 15] vs (b) multiple LED placed at the wall [Saab 16] (c) single LED vs multiple PD with a circular configuration [Naz 18]	29
1.9	(a) FDM protocol vs (b) TDM [Zhua 18]	30
1.10	Architecture of the laser tracker principle [Mura 16]	34
1.11	Localization based on Lidar system [Hu 16]	35
1.12	Model of a room in CityGML [Koho 10]	36
1.13	Example of vision based on image reference [Maut 11]	36
1.14	Four examples of coded targets used for point identification and camera calibration [Maut 11]	37
1.15	Graphical overview for the range versus accuracy of the localization methods in the literature compared to the method proposed in this thesis	40
2.1	Working principle of (a) a corner cube reflector and (b) a beam splitter	43
2.2	Schematic layout of the proposed localization architecture	44
2.3	Top view (a) of the PSD and (b) conveying surface, where the system is optically centralized	45
2.4	Two lenses methodology for changing beam width value	46
2.5	Demonstration of the tracking in one axis for different corner cube's position giving different x_{PSD} values, (a) incident beam trajectory in absence of corner cube, (b) centralized beam $x_{PSD} = 0$, (c) $x_{PSD} < 0$, (d) $x_{PSD} > 0$ and for (c')(d') giving new orientation of the steering device to re-obtain $x_{PSD} = 0$	48
2.6	Model representation of the optical system where the center of the light spot is at the origin of the surface O	50
2.7	Model representation of the optical system where the origin of the surface O superimposed on the end point A of the light beam	52
2.8	Model representation of the optical system where the origin of the surface O superimposed on the end point B of the light beam	54

2.9	Model representation of the optical system for a general case where the spot is at the positive abscissa of the surface	55
2.10	Evolution of the value D_{beam3} compared to θ_x	56
2.11	Scanning pattern compared to the size of the CCR	58
2.12	Schematic of a) a QPD and b) a LEP having an equal measurement range r	60
2.13	Range measurement of the QPD with respect to two different spot sizes	61
2.14	Three different positions of the spot giving same value of X_{QPD} . .	62
3.1	Position of the CCR inside the optical spot	67
3.2	Optical presentation of the system	68
3.3	Control chain of the localization and tracking system	70
3.4	Quadrant photodiode with different spot positions	72
3.5	Block diagram of the localization and tracking algorithm	73
3.6	(a) Schematic description of the MEMS mirror angular variation; (b) detailed description in 2D.	74
3.7	Variation of (a) θ_x as a function of V_{diffx} , (b) θ_y as a function of V_{diffy}	75
3.8	Applied voltages for VX+ vs VY+ for different scanning shapes (a) spiral (b) rectangle, with their corresponding resulting laser scanning pattern (c) and (d), respectively	75
3.9	Schematic layout of the control unit of the MEMS mirror driver. . .	77
3.10	LabVIEW front-end interface	78
3.11	Organizational chart of the entire system	79
3.12	Photography of the control system	80
3.13	Quadrants output voltages during scanning, localization and tracking phase	82
3.14	(a) The micro-conveyor holding a corner cube reflector at the center of the smart surface, (b) micro-conveyor holding a corner cube reflector at the center of the smart surface with light illuminating the corner cube reflector, (c) micro-conveyor with Δy displacement in y direction and light tracking and (d) micro-conveyor with Δx displacement in x direction and light tracking.	83
3.15	(a) Random trajectory of the micro-conveyor being tracked with (b, c, d) three different captures each for different positions of the path	84
4.1	Schematic view of the micro-conveyor placed onto the conveying surface	90
4.2	Projection between the fictive plane π' and the smart surface plane π .	91
4.3	Homographic transformation between the MEMS and the conveying referentials.	92
4.4	Full circular spiral scanning over the conveying surface (a) in the conveying referential; (b) in the MEMS referential; (c) photography of the surface with spiral scanning	95
4.5	Vision system scheme algorithm used for the surface pre-calibration	97
4.6	Implementation of the camera above the conveying surface	98
4.7	Spot template to be acquired	98
4.8	Field of view of the camera for a resolution equal to $45 \mu\text{m}/\text{pixel}$.	99

4.9	The distribution of the 39×39 measured points over the conveying surface	99
4.10	Evolution of the distance error with respect the number of acquisition points	101
4.11	Evolution of the root mean square of the error distance with respect the number of acquisition points	102
4.12	Evolution of the average of distance error with respect the number of acquisition points	103
4.13	The distribution of the 39×39 recalculates points using matrix H of $n = 20 \times 20$	103
4.14	Difference between global (a) and local (b) homography: local homography better fits the distorted measured points	104
4.15	Regions of local homography over the conveying surface	104
4.16	Assembled measured points from the local homography	106
4.17	Field of view of the camera for sensibility equal to $20 \mu\text{m}/\text{pixel}$	106
4.18	Block diagram of the closed loop control of the tracking system	108
4.19	Photography of setup with a zoom in capture of the coordinates system of the conveying surface	109
4.20	Variation of (a) θ_x and (b) θ_y as a function of time during scanning and tracking phase	110
4.21	Micro-conveyor's position in the x -axis with respect to time for horizontal: (a) step response, (b) round trip trajectory and (c) staircase step response.	111
4.22	Micro-conveyor's position in the y -axis with respect to time for vertical: (a) step response, (b) round trip trajectory and (c) staircase step response	112
4.23	Capture of the small micro-conveyor performing the square trajectory	113
4.24	(a) θ_x as function of θ_y during the scanning and tracking of the micro-conveyor moving in a (b) square path.	114
4.25	Localization of multiple micro-conveyors using duplicate system at time t (without multiplexing)	115
4.26	Localization and tracking system block diagram at time t and t' (multiplexing)	116
4.27	Localization and tracking system block diagram	117
4.28	Trajectory of two micro-conveyors	118
4.29	Time multiplexing results showing the resulted trajectory of (a) micro-conveyor number 1 and (b) micro-conveyor number 2.	118
5.1	Generalized approach for the system	122
5.2	(a) Servomotor (b) pan tilt module	123
5.3	Schematic layout of the different components of the OTM	125
5.4	Schematic of the Zemax ray distribution model of the OTM	125
5.5	Schematic description of the ray propagation from the input lens to the two QPDs.	126
5.6	Incident laser beam misalignment effect on the QPD with (a) centered beam, (b) vertically shifted and (c) vertically shifted and outside.	127
5.7	Control block diagram.	129

5.8	Block diagram of the connection layout of the hybrid control approach	130
5.9	(a) Experimental setup with (b) enhanced view of the Telescope block mounted onto the pan-tilt system.	131
5.10	Output voltages of the quadrant photo-detector.	132
5.11	Four different positions of the pan-tilt system following the movement of the laser source	133
5.12	Real view of the assembled OTM design for experimental validation.	135
5.13	Experimental setup of two OTMs.	136
5.14	Pictorial view of the incident laser beam and rotation and translation of the OTM.	136
5.15	Measured output power loss in dB with respect to the angular rotation.	137
5.16	Measured output power loss in dB with respect to the displacement.	138

List of Tables

1.1	Advantages and disadvantages of the different methods of localization	20
1.2	Comparison between the different localization systems	40
4.1	Average (AVG) and root mean square (RMS) of the error distance (ED) for different H matrices calculation using camera sensibility equal to $45 \mu\text{m}/\text{pixel}$	102
4.2	Average (AVG) and root mean square (RMS) of the error distance (ED) for the nine local homography matrices, using camera resolution of $45 \mu\text{m}/\text{pixel}$	105
4.3	Average (AVG) and root mean square (RMS) of the error distance (ED) for different H matrices calculations using a camera resolution of $20 \mu\text{m}/\text{pixel}$	107

List of abbreviations

AoA	Angle of Arrival
AVG	Average
BS	Beam Splitter
CoO	Cell of Origin
DAC	Digital to Analog Converter
DAQ	Data Acquisition
DLT	Direct Linear Transformation
DOF	Degrees of Freedom
ED	Error Distance
EM	Electromagnetic
FCLK	Filter Clock Frequency
FM	Frequency Modulation
FPT	Fixed Pan-Tilt Terminal
LEP	Lateral Effect Photodiode
LM	Linear Motor
LOS	Line Of Sight
MEL	Mechanical Engineering Laboratory
MEMS	Micro-Electro Mechanical System
MPT	Mobile Pan- Tilt Terminal
OTM	Optical Tracking Module
PEDC	Planar Electric Drive Coil
PID	Proportional-Integral Derivative
PM	Permanent Magnet
PMA	Permanent Magnet Array
PSD	Position Sensing Detector
PTM	Pan-Tilt Module
PWM	Pulse Width Modulated
QPD	Quadrant Photodiode
RFID	Radio Frequency Identification
RMS	Root Mean Square
RSS	Received Signal Strength
RTOF	Round-Trip Time of Flight
SM	servomotor
SMA	Shape Memory Alloy
SPI	Serial Parallel Interface
TDoA	Time Difference of Arrival
TOA	Time Of Arrival
UWB	Ultra-Wide Band
WLAN	Wireless Local Area Network

Acknowledgment

Was it not for the effort and great support of the many people surrounding me, this PHD would not have been accomplished. I would like to thank them along these few lines.

First of all, I would like to thank my supervisors Hani Al Hajjar, Erwan Dupont, and Frederic Lamarque, for their never-ending support and their utmost trust in me while pursuing my work. Thanks to their encouragement and their help, I was able to complete this PHD on time with satisfying results. Their wisdom and advices outreached the professional barrier to have also impacted me on the personal level. With their help, I was able to engage in the research field and to be part of supervising master's degree students which in turn leveraged my experience level. Their extensive support, daily guidance, and their open-door policy helped me to pave the way for being self-dependent. Their criticism, remarks and on-spot notes have always motivated me to push further and to be more effective. They have offered their absolute time and effort and have invested their supreme knowledge into helping me in accomplishing my work and completing my tasks. They embraced my questions and responded to my queries promptly and without any hesitation. It was a privilege to have the chance of working in such a professional and skillful framework in Optics and Photonics. To them, I owe the credit of completing this PHD.

I also thank the jury members Anne Julien Vergonjanne, Kevin Heggarty, Dritan Nace, and Guillaume Laurent for agreeing to evaluate this work.

I would like to thank all members of Mechanical Engineering Department especially, to Christine and Laurent I express my great appreciation. They have offered their help and their advice whenever I had trouble. I also would like to thank Muneeb for guiding and sharing his experience in launching the smart surface, and for his general advices and help. I would like to thank Jeremy Terrien for his generous help in electronics, and his thorough advises in this field. I would like also to thank Phylippe Pouille for his advice and knowledge in 3D printing as well as his generous offer and help in using the cutting and drilling machine. I would also like to express my gratitude to all the Administrative team for the paperwork managing that was offered from Anne Sophie and Muriel as well as

the Ecol doctoral administration Julie jarek and Marie lotiquet.

I thank Flavio and Mohammed, the students who have contributed in the simulation and in the experimental work.

It was a tremendous opportunity to have been able to work in the smart cave project alongside IRT BiCOM from Télécom Bretagne, Brest. I extend a special appreciation to Bruno Fracasso for welcoming me in his lab and joining me in many meetings, and Jean-Baptiste and Gauthier for forming an excellent team-work. This project allowed me to implement my acquired skills in the thesis and to project them from the micro-scale to macro-scale.

I thank all my lab colleagues, especially Rita, Georgina, Ajynkia, Simon, and Marcel who have shared with me a lot more than a laboratory workplace, but rather great memories and well spent time along with fruitful interaction of different intellectual knowledge and ideas.

My best friends Boutheina, Aya, Iman, Hanin, and Vivian have become my second family to whom I owe a lifetime of gratitude. The joyous adventures and good times that we shared will ever be engraved in my memories along with the hard times where we stood together and faced all obstacles side by side.

My absolute gratitude to my mother who has always believed in me and has shed her blood, sweat, and tears into raising me to pursue my dreams. Her extraordinary support and endless encouragement was all that I needed to overcome hardships and earn my degree.

To my late father who passed away before witnessing my PhD defense, I dedicate this accomplishment to make him proud and to assure him that I will overcome all difficulties as he raised me to do so.

I thank my brothers and sisters who have been the arms that embraced me throughout all those years, and provided un-conditional support and moral guidance in all matters. Their keen motivation and inspiration was the key to my persistence.

To Ahmad Malak, my backbone and mentor, I owe my deepest love and gratitude, for he has ever believed in me and accompanied me throughout my journey.

Abstract

This thesis aims to develop a method for optical localization and tracking of micro-conveyors moving over a surface in the context of micro-robotics. The principle of the proposed localization method consists of detecting a beam that is reflected on the micro-conveyor and analyzing this optical received signal to obtain the corresponding positions. The main elements of the system are a corner cube reflector, a MEMS mirror and a beam splitter. The corner cube is placed on the micro-conveyor in order to allow the optical signal to be reflected in its incident direction. The MEMS mirror allows the surface to be scanned with the laser. As for the beam splitter, it is an optical component used to guide the reflected light to a photodetector which is in turn used for localization and tracking through the exploitation of the signal that it detects. The important role of localization is to optimize the trajectory followed by the micro-conveyors. This could be achieved by controlling the respective position and speed of each of them in order to be finally able to localize the micro-conveyor with high precision and to avoid possible collisions between them. The surface used is a micro-conveying surface based on an electromagnetic principle, developed at the Roberval laboratory. The surface is used to perform experimental tests and to evaluate the developed sensor. A system calibration, using homography, was carried out in order to ensure the localization and tracking of the micro-conveyor, and then to control its trajectory and speed. Simultaneous localization and tracking of two micro-conveyors using time division multiplexing was also developed and validated in this work.

An application of the thesis at the macroscopic scale is presented as well through applying free space optical communication between two mobile systems controlled by closed-loop optical tracking.

Each system includes an active transmitter and a receiver (instead of a passive corner cube reflector in the case of the micro-conveyor). The system is driven by two servomotors which permit it to have free movement in three-dimensional space. The two modules must be aligned in order to be able to send and receive information by laser and thus communicate. In this case, a high-precision tracking system which is capable of aligning the two moving modules is required.

Résumé

Dans le contexte de la micro-robotique, cette thèse vise à développer une méthode de localisation et de suivi optique de micro-convoyeurs se déplaçant sur une surface. Le principe de la méthode de localisation proposée consiste à détecter un faisceau réfléchi sur le micro-convoyeur et à analyser ce signal optique pour obtenir les positions correspondantes. Les principaux éléments du système sont un rétroreflecteur à coin cube placé sur un micro-convoyeur et qui permet de réfléchir le signal optique dans sa direction incidente, un miroir MEMS qui permet de balayer la surface avec un éclairage laser, un séparateur de faisceau qui est un composant optique utilisé pour guider la lumière réfléchie vers un photodétecteur utilisé pour assurer la localisation et le suivi à travers l'exploitation du signal détecté par ce dernier. L'importance de la localisation est d'optimiser la trajectoire suivie par les micro-convoyeurs en contrôlant leur position et leur vitesse pour finalement pouvoir localiser les micro-convoyeurs avec une grande précision et éviter d'éventuelles collisions entre eux. Pour faire des tests expérimentaux et évaluer le capteur développé, la surface utilisée est une surface de micro-convoyage basée sur un principe électromagnétique, développée au laboratoire Roberval. Une calibration du système, en utilisant l'homographie, a été effectuée afin d'assurer la localisation et le suivi du micro-convoyeur pour après contrôler sa trajectoire et sa vitesse. Une localisation et un suivi simultané de deux micro-convoyeurs en utilisant un multiplexage temporel a été également développé et validé dans ce travail.

Une application de la méthode proposée dans la thèse à l'échelle macroscopique est également présentée pour assurer un suivi optique contrôlé en boucle fermée pour une application de communications optiques en espace libre entre deux systèmes mobiles. Chaque système inclut un émetteur et d'un récepteur actifs (au lieu d'un coin cube passif dans le cas du micro-convoyage) et actionné par deux servomoteurs pour avoir un mouvement libre dans l'espace tridimensionnel. Les deux modules doivent être alignés pour pouvoir envoyer et recevoir des informations par laser, donc communiquer. Dans ce cas, un système de localisation et de suivi de haute précision capable d'aligner les deux modules mobiles est nécessaire.

General Introduction

The positioning and tracking of moving targets is a relevant and essential topic in several fields of engineering and science. This topic has attracted the attention of researchers and development centers. Many studies have been devoted to determine the real-time position of objects or individuals at different scales, ranging from macro to nano scale, depending on the application. The existing methods that localize and track over a wide coverage (order of cm and m) suffer from a small accuracy (order mm - cm), such as radio waves, ultrasound based methods and vision systems within a large field of view. In addition, high-resolution methods (order of nano meter) have a limited range (order of μm). In this work, we propose a method that allows to locate and track mobile objects moving in a wide range (order of tens of cm) with a relatively high accuracy (order of tens of μm). Two applications are being studied in this thesis. The first is in the context of a micro-factory to monitor the movement of a mobile micro-conveyor and the second is to ensure the free space optical communication between mobile systems with a high bit rate data transmission.

In the context of micro-factory, the aim is to develop an original method for localizing and tracking mobile micro-conveyors moving over a conveying surface. The main advantage of the micro-factory is saving large quantities of resources such as space, energy, material and time. Micro-factory applications can be divided into several thematic fields: manufacture of micro-parts, micro-assembly of micro-parts, measurement of the quality of assembled systems or manufactured parts and finally, transport of a subsystem from one point to another. The latter thematic field corresponds to the theme of this thesis.

The principle of the proposed localization and tracking method is to detect a reflected beam on the micro-conveyor and analyze this optical signal to obtain the corresponding positions. The main elements of the system are a corner cube reflector placed on the micro-conveyor, a 2D MEMS mirror and a beam splitter. The corner cube reflector allows the optical signal to be reflected in its incident direction. The MEMS Mirror allows the surface to be scanned with diffuse laser spot illumination. The beam splitter is an optical component used to guide reflected

light to a position sensitive photo-detector. The latter is used to localize and track the micro-conveyor through the exploitation of the optical signal that it detects.

The importance of localization is to optimize the trajectory followed by the micro-conveyors. This can be achieved through controlling their position and speed of movement in order to finally be able to locate the micro-conveyor with high precision and avoid possible collisions between several micro-conveyors. To perform experimental tests and evaluate our sensor, the platform used is an electromagnetic surface (EM) developed at the Roberval laboratory. It is constituted of a matrix of cells, where each cell is composed of a flat coil (conductors) interacting with permanent magnets fixed to the moving structure of the micro-conveyor. After injecting the coils with supplied currents, micro-actuation along two orthogonal axes is produced using Laplace's force. As a result, the micro-conveyor moves in a planar motion over the conveying surface. The aim of this thesis is to control the injected currents depending on the position of the micro-conveyor, in order to ensure it follows the desired controlled path. The position of the micro-conveyor is measured using our optical developed sensor after calibrating the surface. In this work, the surface is calibrated using a homographie method. It is a projection transformation method between two planes, which are: the conveying surface and the plane parallel to the MEMS mirror. The relation between these two planes is ensured by the use of a transformation matrix \mathbf{H} . This matrix is calculated in an offline pre-step, by acquiring corresponding measured points in each plane. In fact, during calibration, the coordinates in the conveying surface are measured using a vision system and the coordinates in second plane are obtained from the rotational angles of the MEMS mirror. After calculating the matrix \mathbf{H} , in real time application the micro-conveyor's position is calculated by multiplying the matrix \mathbf{H} by the known coordinates in the second plane that correspond to the actual MEMS orientation. In a closed loop, the path of the micro-conveyor is controlled by comparing the measured position with the desired position. The criteria set for the positioning system are to achieve a positioning accuracy of less than 50 μm .

The second application of the thesis at the macroscopic scale is also presented for tracking in a closed-loop control system to ensure free space optical communications. The system consists of an active transmitter and receiver (instead of a passive cube corner reflector in the case of micro-conveyance application) and operated by two servomotors to have free movement in three-dimensional space. The two modules must be aligned to be able to send and receive information through laser beam, thus achieving communication. In this case, a high-precision localization and tracking system is required to be able to align the mobile module with the fixed one and ensure optical communication. For each module, two

servomotors are deployed in a closed loop optical detection system along with two quadrant photo detectors. The photo detectors control the orientation of the two servo-motors by indicating large scale dis-alignment according to the tracking feedback. As for small scale dis-alignment that exceed the precision scope of the motors, a MEMS mirror is integrated in each module in a closed loop control system with a third quadrant photo-detector to correct the small angles and translations dis-alignment.

The thesis manuscript is divided into 5 chapters. The context of each chapter is briefly detailed below.

The first chapter is a bibliographical analysis of the different localization and tracking methods at macro and microscopic scales. A comparison is realized between the accuracy and range of each method in order to show the importance of our proposed method giving a high resolution of few of μm within a relatively high range of tens of cm.

The system architecture and modeling of the remote optical localization and tracking method, is presented in chapter 2. In addition, working principles of each optical/optoelectronic components are discussed and explained. An application of this method in micro meso-scale is presented in chapter 3 and 4, where the optical system localize and track a mobile micro-conveyor moving over a 2D conveying surface.

In chapter 3, list of the conveying surfaces is provided, where the localization and tracking system can be applied to any of them. Then, the functioning of the control system is detailed. Moreover, this chapter is dedicated to validate the localization and tracking of the micro-conveyor, in an open loop control of the target movement, where the optical system should track the movement of the micro-conveyor for any random trajectories it makes over the conveying surface, up to a certain maximum motion speed. The parameters that affect the maximum speed of the micro-conveyor movement, before losing tracking, are discussed and presented as well.

Chapter 4 deals with the tracking of the micro-conveyor in a closed loop with the conveying surface. The actuation principle of the conveying surface and the surface architecture are presented. Moreover, the calibration of the conveying surface is presented by explaining the Homography method. Calculation is presented with a study to optimize the values of matrix H. Different scenarios are investigated which are global and local homography, in addition to the field of view of

the camera used in the offline and pre-step measurement. Experimental results are presented to validate the closed loop tracking in 2D motion. The chapter ends with multi conveyors control by proposing a time multiplexing method, whose concept is proven.

Chapter 5 is the application of our proposed method at macro-scale system. A prototype of two mobile communicating systems is presented. In addition, the tracking closed loop control with the two servo-motors and the MEMS mirror is discussed and validated, separately.

The manuscript closes with a conclusion with a preview on the work's perspectives.

Chapter 1

State of art on the technology of the localization and tracking of mobile systems

1.1 Introduction

Indoor localization has recently gained extra global recognition due to its essential role contribution in modern technologies, such as Factory of the Future, with many research and business investments being dedicated to this area. The literature review is divided into four main parts: the first part presents the indoor positioning applications, the second part helps to understand the different localization methods that already exist, the third aims to identify the performance metric that classifies the system and the last part studies the existing localization systems in macro and micro scales.

1.2 Localization and tracking applications

Today's modern life requirements, living standards and industrial technological progress, impose the need for positioning and tracking systems. This emerging need is highlighted through the vast list of localizing and tracking applications and capabilities. Although some applications may not be applicable at the present time, but it is irrefutable that major progress and enhancements are being achieved in future concepts of positioning and tracking systems.

In industry, over the last few years, mechanical engineering has been moving towards smart systems and automation in manufacturing processes. Indoor localization and tracking has embarked the industrial field and has become the subject of interest in various applications, such as smart factories, industrial robots, robot

guidance, robot cooperation, quality surveillance and automated monitoring as discussed in [Li 12b]. Indoor localization and tracking offers in locating tagged tools and equipment that have been lost or scattered around the department space within industrial facilities. Such systems could also implement safety guidelines through investing their positioning capabilities in smart worker protection and preventing possible collisions or accidents. As for logistics and optimization, collecting location data concerning assets and employees is a key process indicator for developing a more optimized and efficient environment especially in complex systems. For example, it is very efficient to find items when needed in a large storage facility right on spot and with minimal effort and time. Tracking of each asset becomes feasible once localization is accurately achieved. Positioning systems would certainly increase the efficiency rate for systems of merchandise management in airports, ports and for rail traffic.

In the sector of high bitrate line of sight communication, localization and tracking are essential for optical communication with high bitrate systems similar to those mentioned in [Al H 13]. Line of sight (LOS) between emitters and receivers should be maintained, during the motion of one of them. To do that, tracking is mandatory so that the systems continue to communicate with each other.

In the medical care domain, it is of utmost importance to know the location and to track the medical staff within the hospital during emergencies and crisis. The tracking of medical apparatus and a patient's activity is also a very important medical application [Tork 12]. For instance, a patient's abnormal fall could be detected as discussed in [Huan 09]. Throughout surgeries, the exact positioning of the robotic equipment which provides aid of the surgeons is an extreme necessity. Thus, practical surgical equipment could be used instead of traditional apparatus. Home applications are also one of the leading targets of indoor services. For instance, detecting lost items, games depending on physical movements and services at homes based on location, are examples of some home applications. Ambient Assistant Living (AAL) systems are founded to serve and facilitate the daily home related activities and tasks performed by the elderly and disabled people. A key function of AAL systems is location awareness which requires an indoor positioning functionality [Zeti 10]. In terms of intelligent transportation, the most common user applications targeting vehicles would certainly be the realization of an ideal navigation experience by providing trajectory directions within parking garages. Hence, the navigation to a certain desired parking space would be feasible along with the further navigation to the pedestrian's target position [Maut]. Also, there are systems which are developed in particular to help people having vision problems and disabilities in indoor and outdoor environments. Providing walking assistance and navigation is a must for vulnerable people [Mirz 12],

[Día 13] .

The contribution of the marketing field in terms of positioning systems has also gained recognition over recent years. Location-Based Services (LBS) are product applications serving significantly the majority of the market share on a commercial grade standard. Such systems benefit from the geographical location to send data related to context which can be reached through mobile devices [Tsai 17] . Services such as LBS are demanded in indoor and outdoor applications. For instance, indoor LBS is applied through collecting safety data or relevant information on events such as concerts, cinemas or similar events in the proximity. Other applications include navigation to the desired shop or office in a public region such as a mall or an office. Location based applications could be of topical interest. For example, detecting the location of products in a warehouse or store is of great value. Advertisements, bills, and search services that are based on location have a great commercial significance.

1.3 Localization and tracking methods

Localization methods can be divided into three general approaches: proximity, triangulation and scene analysis. In this section, these 3 techniques are described in the following paragraphs [Fari 13],.

1.3.1 Proximity Detection

Proximity algorithm is considered relatively as a simple positioning method to implement. It provides relative symbolic information on location. This method depends on cell of origin (CoO) or cell identification (Cell-ID), [Magh 16]. Each cell possesses a well-known position and limited range. At a given time, the mobile target is collocated with the cell that detects it. If more than one cell detects the mobile object, it is collocated with the one receiving the strongest signal. The accuracy of this method is favored by the decrease of the cells sizes which can be improved if additional sensors are used, however, it will increase the cost. Many localization systems use this method such as: systems using Bluetooth [Bouc 16], radio frequency identification (RFID) [Boli 15], Wi-Fi [Agat 16] and infrared radiation-based systems (IR) [Yasi 13] .

1.3.2 Triangulation

Triangulation relies on the geometric properties of a triangle to locate the target position. The triangulation method has two derivations: angulation and lateration. Angulation is based on angle measurement. This method is also called angle of arrival (AoA), [Zhan 10]. Range measurement method is another term for lateration, which relies on signal attenuation property and time base methods, such

as, time of arrival (ToA), round-trip time of flight (RToF), and time difference of arrival (TDoA). In the paragraph below, we present these two methods and their different variants, [Bren 17], [Liu 07].

Angulation method:

The angle of arrival method (AoA), also known as direction of arrival (DoA), employs the angles between the mobile target and a fixed base station to estimate the unknown location. In 2D applications, having two known reference points (A and B), and by measuring their corresponding two angles (θ_A and θ_B), the location of the target object (O) can thus be obtained as shown in figure 1.1. The position of tracked object is the intersection of two direction lines, each formed by the circular radius from the fixed base to the mobile target. The accuracy can be improved with using three base station or more instead of two.

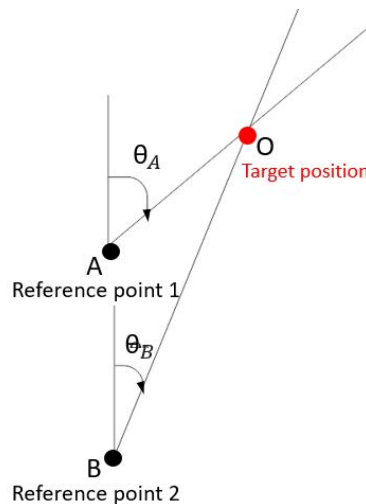


Figure 1.1: Positioning based on AoA measurements in 2D example

The advantages and disadvantages of AoA are the following [Liu 07].

The advantages of AoA are:

- Few measuring units are enough for localization: two measuring units for 2-D positioning and three measuring units for 3-D positioning,
- No need for synchronization between the measuring units.

The disadvantages of AoA are:

- Relatively large and complex hardware requirements.
- As the mobile target moves away from the measuring units, the location estimation degrades.

- High accuracy is needed for the angle measurements, while some applications such as radio wireless networks have limited accuracy due to multipath reflections arriving from misleading directions, shadowing, or the directivity of the measuring aperture.

Lateration method:

Lateration is a distance based method distributed among four main sectors, as illustrated below.

I-Time of arrival (ToA)

In this method, the mobile object is localized by exploiting the fact that the distance between the measuring units and the target object, is directly proportional to the propagation time. The mobile object sends a time stamp signal to a measuring unit, and the ToA value can be calculated by subtracting the time of transmission from the receiving time of the signal. The distance between the mobile target and the received station can be calculated from the one-way propagation time delay and the signal speed as follow, [Zhan 10]:

$$R = t \times v$$

Where v represents the traveling speed of the signal in the medium, t is the time taken by the signal upon traversing the trajectory from the transmitter to reach the receiver node and R represents the distance separating the transmitter on one hand and the receiver node on the other hand.

The absence of information for a specific direction causes each receiving station to become the center of a circle with a radius of the distance that separates it with the mobile target.

In a 2D plane, the position of the target (O) can be retrieved by geometrically calculating the intersection point of at least 3 circles centered by three different reference points (A, B and C), as shown in Fig.1.2.

Moreover, another approach to calculate the position of the target is to adopt the least mean square estimation (LSE) or the residual weighting (RWGH) algorithm. The LSE algorithm is based on minimizing the sum of square of a non linear cost function. The RWGH algorithm can be viewed as a form of weighted least-squares algorithm.

The main drawback of the ToA method is that all the devices of the system receivers and transmitters should be well synchronized, since this method needs precise knowledge of the transmission start time. Which is difficult in real life application. With the need of an additional server for time delay measurement, the cost of the system increases [Fari 13].

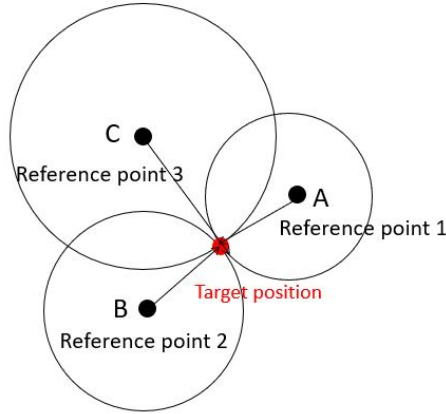


Figure 1.2: Positioning based on ToA measurements in 2D example

II- Time difference of arrival

Time Difference of Arrival (TDoA) techniques are based on multiple pairs of reference points with known locations and use relative time measurements at each receiving node instead of absolute time measurements as in ToA. Each pair of reference points gives a hyperbola. The hyperbola is the set of points of a constant range-difference ($c \times \Delta t$) from two reference points. Location estimation is the intersection of all hyperbolas. For 2D applications, at least three references points with known positions are required (Fig. 1.3). The equation of the hyperbola is:

$$R_{i,j} = \sqrt{(x_i - x)^2 + (y_i - y)^2} - \sqrt{(x_j - x)^2 + (y_j - y)^2};$$

Where (x_i, y_i) and (x_j, y_j) represent the coordinates of fixed receivers i and j coordinates and (x, y) represent the unknown coordinates of the target. With 2 equations of 2 hyperbolas, the 2 unknown coordinates x and y of the mobile target can be calculated. An easier solution is to linearize the equations through the use of a Taylor-series expansion and create an iterative algorithm [Zafa 19].

The advantage of TDoA is that only synchronization between the transmitters is required unlike ToA where synchronization is required between the transmitter and the receiver.

III- Round-Trip Time of Flight

Round-trip time of flight (RToF) relies on measuring the time that the signal takes to travel back and forth from the transmitter to the measuring unit, [Zhan 10]. The advantage of RToF method is the fact that it uses one node to record the transmitting and arrival time, while that of ToA needs two local clocks in both nodes to measure the delay time. As a consequence, there is not any synchro-

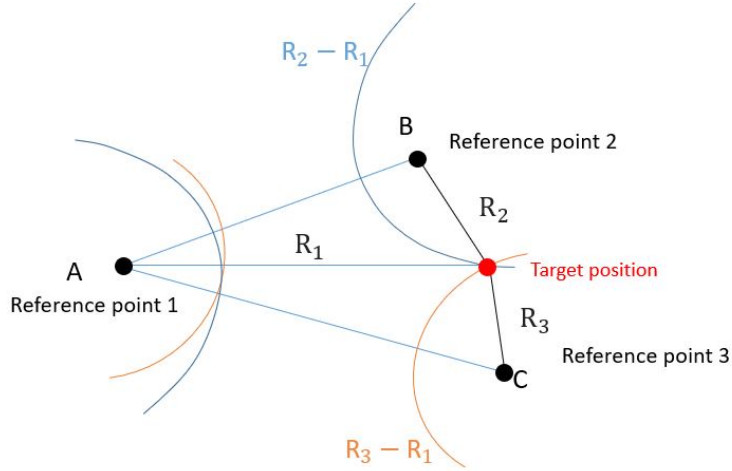


Figure 1.3: Positioning based on TDoA measurements in 2D example

nization problem for the RToF method. The distance R , using RToF method, is calculated as follow:

$$R = \frac{(t_{RT} - \Delta t) \times v}{2}$$

where t_{RT} represents the time spent for a signal to complete the course of traversing back and forth from one node to the other, Δt is the predefined time needed by the hardware device to execute at the receiver node, and v is the speed of the transmitting signal. The disadvantage of this method is presented through the fact that the successive range measurements of several devices should be executed in a successive manner. This may lead to certain ambiguity and uncertainty for applications that include fast moving devices.

IV- Received Signal strength (RSS-Based) Method

Starting from the knowledge of the received and emitted signal power, it is possible to calculate the power loss between the transmitter and the receiver. Using theoretical and empirical models, this loss can be translated into an estimation of the distance separating the emitter and the receiver. A mathematical framework is set in empirical form in order to compute the distance, as follows [Zhan 10]:

$$p(R) = p(R_0) - 10n \log \left(\frac{R}{R_0} \right) \quad (1.1)$$

Where $p(R)$ and $p(R_0)$ represent the strength of the signal acquired at R and R_0 , respectively. R is the distance between the transmitter and the receiver. R_0 is the distance related to the reference, and n represents the hindering influence during routing which could be realized through theoretical and empirical calculations.

Hence, the receiver will be localized. This method is mainly used for RF signals.

Due to severe multipath fading and shadowing present in the indoor environment, path-loss models do not work well in all cases.

1.3.3 Scene analysis / fingerprints

The scene analysis refers to the type of algorithms that first collect features (fingerprints) of a scene and then estimate the location of an object by matching online measurements with the closest a priori location in a database. RSS-based location fingerprinting is commonly used in scene analysis, [Liu 07]. Fingerprinting is described by two major phases, [Bren 17]. The First is denoted by an offline process, where maps for fingerprinting are set up either by empirical measurements or by analytical computation. The strength of the signals which are collected from fixed stations are measured at different points throughout a building and then inscribed into an offline database. For the second phase, the values of the signal strengths measured in real time are compared in accordance with the stored values in the offline database. In order to prevent detailed calibration processes in the case of analytical model, the generation is then used. As a result, a signal propagation model could be favored for computing the reference values of signal strengths.

As conclusion, the figure 1.4 sums up the hierarchy of the localization methods and table 1.1 illustrates the advantages and disadvantages of each one of them. Then, the tracking and tracing systems presented in the following paragraph consider one or more of these measurement methods according to its preferences and limitations.

1.4 Performance metrics

The choice of the positioning system depends on the desired application according to the following criteria:

Accuracy:

Accuracy (or location error) of a system is considered as an important requirement of positioning systems. Accuracy, linked to an uncertainty domain, tells us how close a particular measurement is to the correct position value. The higher the accuracy, the better the localization. The computation of the root mean square error is a relevant parameter for the quality of localization method, having the following formula:

$$RMS = \sqrt{\frac{1}{n} \sum_{i=1}^n (P_{(measured)_i} - P_{(desired)_i})^2}$$

where n is the number of measurements, $P_{(measured)_i}$ is the measured position vec-

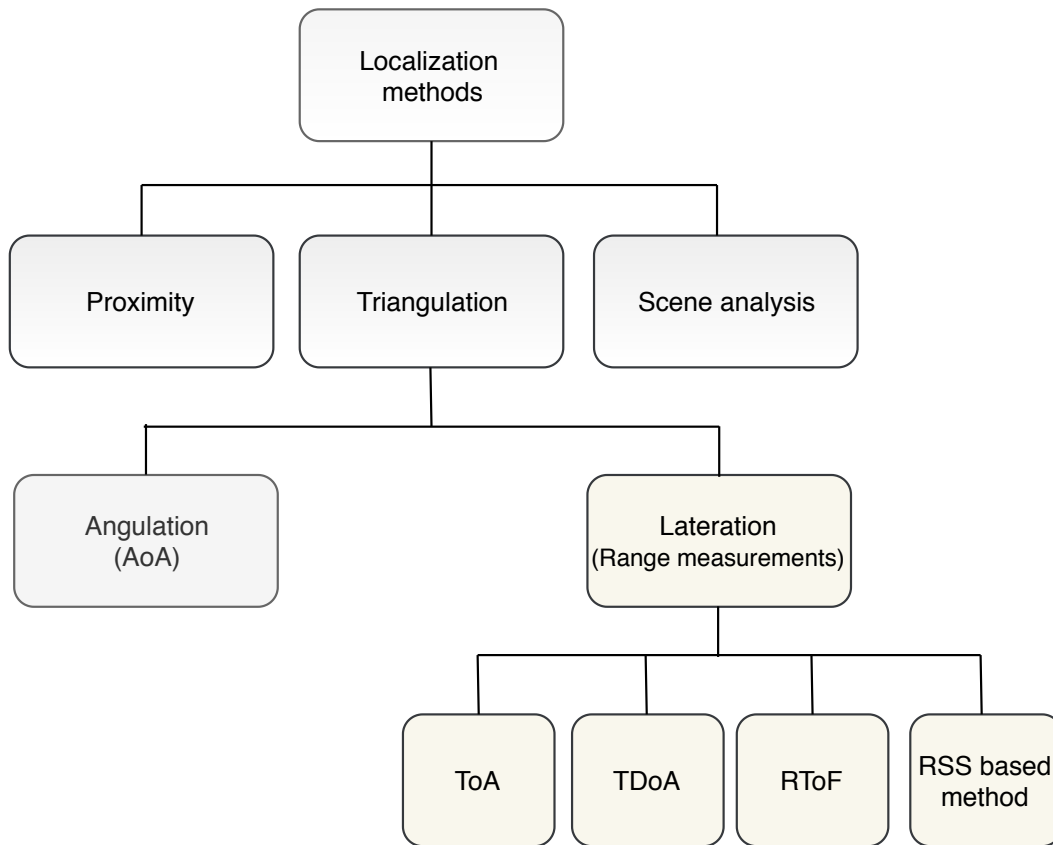


Figure 1.4: Classification of localization methods.

tor and $P_{(predict)i}$ is the corresponding desired position vector. The absolute average of the total error measurement is another useful qualification parameter obtained by the formula below:

$$a = \frac{1}{n} \sum_{i=1}^n (\|P_{(measured)i} - P_{(desired)i}\|)$$

The more these values decrease, the more accurate the system becomes.

Other parameters are essential to qualify a localization method such as precision, coverage, adaptiveness, and cost...

Precision:

Precision is the consistency of repeated measurements, the more consistent the results the more precise the measurement. It is possible to have a precise measurement but not accurate and vice versa [Stre 06] (see figure 1.5).

Responsiveness:

Responsiveness determines how quick the system is to update the new estimated location of the mobile target.

Table 1.1: Advantages and disadvantages of the different methods of localization

Method	Advantages	Disadvantages
Proximity	-Simple algorithm	-Accuracy depends on the number of devices.
AoA	- Fingerprinting is unnecessary. -localization has elevated accuracy. No time synchronization	- Need of complex instruments. -Limited accuracy when multipath effects misleads directions.
ToA	-Gives high accuracy. -Fingerprinting is unnecessary.	-Time synchronization is mandatory between transmitters and receivers. Precise performance requires LOS.
TDoA	Fingerprinting is unnecessary. No time synchronization between the device and RN.	Clock synchronization is needed between the reference nodes (RN). Greater bandwidth is needed.
RToF	-Fingerprinting is unnecessary. -High accuracy could be achieved	-Performance in short range measurements is influenced by any obstruction in processing.
RSS	-Applicable in many technologies -Practical in installation -Cost effective.	-Vulnerable to factors such as exterior noise from the environment. -Less accuracy in localization. -Multipath fading.
Fingerprints (Scene analysis)	- Easy to implement	- Needs updated fingerprints even if there exists a slight space variation.

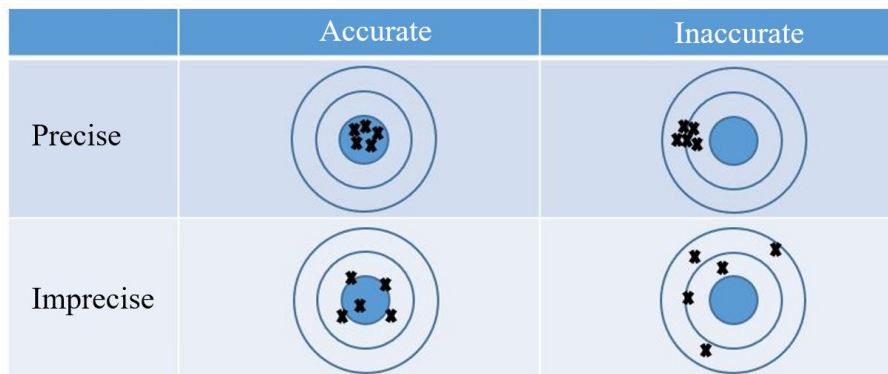


Figure 1.5: Accuracy vs precision of a system, [Stre 06].

Coverage:

The network coverage is the geographic area where the target can be localized.

We distinguish two types of coverage, [Fari 13]:

- Local coverage: for small and limited areas for example single room or building. In this case, the coverage size is specified (e.g., (m), (m²), or (m³)).
- Scalable coverage: it can change depending on the amount of hardware. The coverage increases when more hardware is used in the system, [Njoy 17].

Adaptiveness:

Adaptive system has the feature to work with the same performance, even if the environment changes (temperature, humidity . . .). This type of systems can provide better localization accuracy than system that cannot adapt.

Cost and Complexity:

The Complexity of a positioning system is caused by the hardware and software under use [Bren 17]. Cost remains one of the most common criteria, and it plays a key role in the consumer and developers choices. It can be affected by, [Fari 13]:

- Price and lifetime of the equipment
- Time of installation and maintenance
- Cost of extra infrastructure
- Weight and space needed
- Energy consumption

In the next section, we will mention the most common localization and tracking systems. Each technique will be defined and explained briefly.

1.5 Localization and tracking systems

Numerous studies have made it possible to determine the real-time position of objects or individuals at different scales, such as in macro, meso and micro levels, depending on the application, [Zafa 19], [Sakp 17], see figure 1.6.

1.5.1 Macro-scale localization and tracking:

Radio frequency based system

Radio frequency (RF) technologies are widely used for localization purposes, because they have larger coverage area and need less hardware compared to other technologies. Moreover, radio waves have the advantage that they can penetrate obstacles like wall, building and human bodies. In addition, RF based technologies are branched into:

- i) Narrow band based technologies such as (WLAN, Bluetooth, FM and RFID).
- ii) Wide band based technologies such as ultra Wide Band (UWB), which is based on the transmission of short range and high bandwidth of at least 500MHZ.

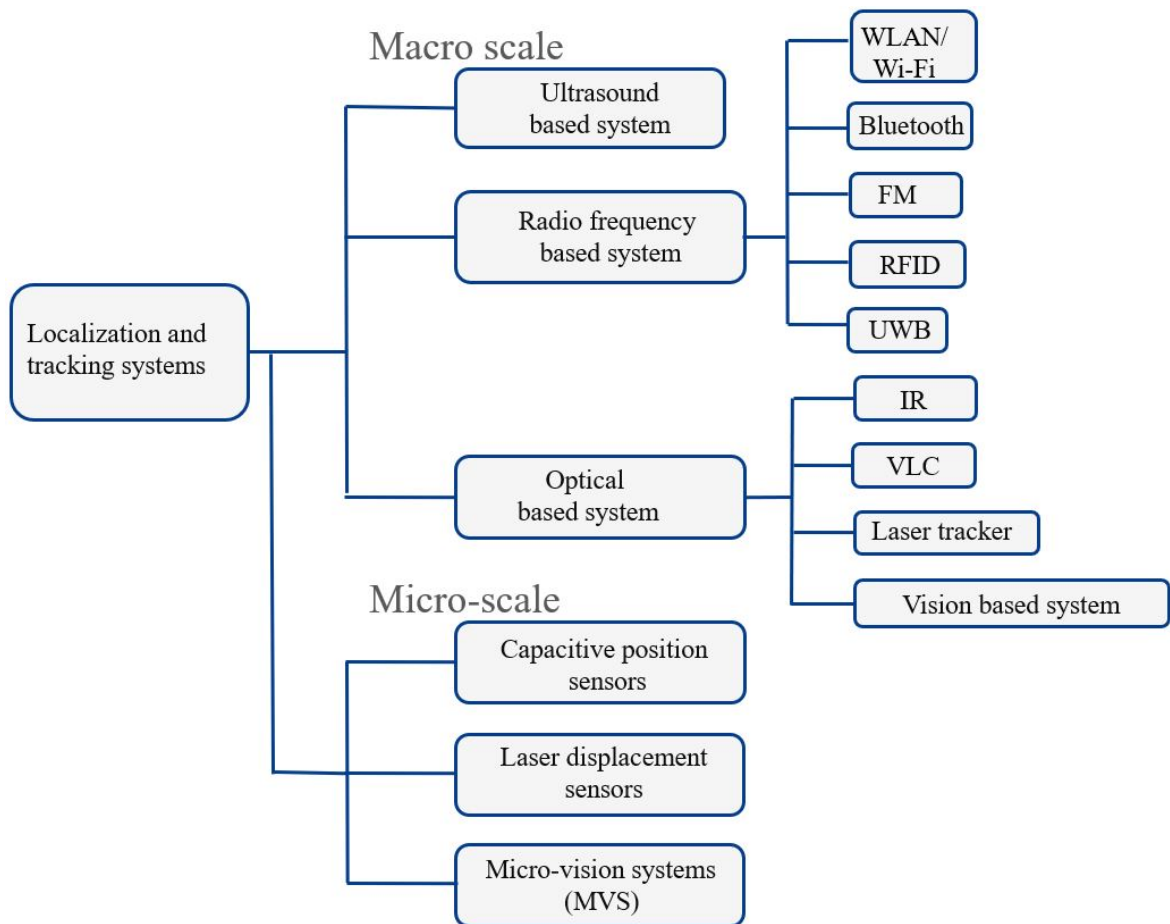


Figure 1.6: Different Localization Systems.

Wi-Fi / WLAN

Wi-Fi, short for wireless fidelity, is a set of wireless communications protocols covered by the standards of the IEEE 802.11. A Wi-Fi network allows the connection by radio waves of several devices (computer, router, smartphone, etc.) within a network to enable the data transmission between them, [Zafa 19], [Bhat 17]. The IEEE 802.11 standards, describe the characteristics of a wireless local area network (WLAN), with a typical raw bit rate of 11, 54, or 108 Mbps and a distance range of 50–100 m. IEEE 802.11 is commonly used in positioning systems since the infrastructure already exists and no additional hardware is needed. Moreover, Wi-Fi signals can penetrate walls and obstacles and no line-of-sight (NLOS) is required between components.

The principles used for localization are based on measurements of the RSS or ToA/TDoA or AoA. Due to the complexity of angular and delay measurements, the technique of RSS is the most used for localization. Several approaches can be adopted to locate the target, [Main 14]:

- i) Cell of origin (CoO) method: the target receives different RSS from all the

access points existing in its environment. The access point having the highest RSS coordinates is equal to the access point emitting the highest RSS.

- ii) Triangulation method: several devices are required to receive RSS from different locations, in order to calculate the position of the target using the geometric proprieties of a triangle.
- iii) Fingerprinting: a database is constructed by measuring the RSS of different fixed routers distributed in the zone of interest with known sampled positions. Then, in real time application, the on-line measurements will be compared to the RSS values already stored in the off-line database, in order to estimate the location.

Bhatt et al. adopted the Wi-Fi positioning system (WPS) using the fingerprint method [Bhat 17]. In their work, the positioning accuracy reaches a level of better than 1 m for a range covering area of $25 \times 30 \text{ m}^2$.

Bluetooth

Bluetooth technology (or IEEE 802.15.1), works in the 2.4 GHz industrial, scientific and medical (ISM) band. It uses the technique of Frequency Hopping Spread Spectrum (FHSS) in order to immunize communications against different types of interference and improves the co-existence with other signals using the same band as Wi-Fi. The benefits of using Bluetooth for exchanging information between devices are that this technology is of high security, low cost and low power consumption [Yoha 18].

Localization using Bluetooth can be done by measuring the following signals [Kamm 14]:

1. CID (cell ID): the identity of a Bluetooth cell is given by the ID (MAC address of a computer for example) of the Bluetooth beacon or access point that belongs to the cell under consideration. The principle of localization is to use a database which combines identifiers with the positions of known cells.
2. Measuring Received Signal Strength (RSS), see paragraph 1.3.2.
3. Inquiry Response Rate (IRR), measured by an access point for a specific Bluetooth target. In fact, IRR represents the received number of responses over the total number of inquiry procedures performed over a given period. The localization is based on the assumption that the failure rate is correlated with the distance. Signal-to-noise ratio (SNR) decreases when the distance increases.

One of the drawbacks of using Bluetooth technology in localization is that, for each location finding, it runs the device discovery procedure; due to this, it significantly increases the localization latency (10–30 s) and power consumption as well. That is why Bluetooth device has a latency unsuitable for real-time positioning applications [Fari 13].

Frequency Modulation (FM)

Frequency Modulation (FM) radios is a well developed broadcasting technique that transfers data over a carrier through frequency variation. Indoor navigation could potentially make use of signals transmitted from broadcasting towers. Due to the insufficient timing data of the FM signal, the ToA and TDoA methods were considered hardly applicable. Nevertheless, time independent fingerprinting methods that rely on the strength of the signals are feasible for FM signal broadcast. The advantages of FM radio positioning is that it makes use of the infrastructure of the radio tower. The latter provides wide indoor and outdoor coverage, high power of the received signal, and cost efficient hardware. FM can embark secured and restricted areas while other RF technologies hindered by reasons of security. This is possible due to the passive attribute linked to the client device. Moghtadaiee et al. used an office environment to install a positioning system of RSS fingerprinting based on FM radios [Mogh 11]. An average accuracy of 3 m was reported within a space of 253 m^2 upon collecting FM fingerprints that consists of 17 sensed FM channels at 150 grid points. Even with the same operating circumstances, the WLAN fingerprinting proved to be of higher accuracy.

Radio frequency identification (RFID)

RFID is a radio frequency technology that permits the identification of an object, its tracing and remote learning of its characteristics, through communication by radio waves between a reader and tags that are attached to or incorporated into the object. The RFID tag consists of a chip connected to an antenna, encapsulated in a holder. It is read by a reader which captures and transmits the information. In fact, there are 3 ways to access and use the RFID tags:

- i) Tag read-only, where its ID is stored once during manufacturing and becomes non-editable with no additional memory. It is used only to identify the product.
- ii) Tag read/write. In this case, the chip has a small memory on which it is possible to write a particular unique number to identify the end user.
- iii) Tag read/ write protected, where the user needs to enter a password before accessing the tag and write into its memory.

Moreover, there are two main types of RFID tags:

- i) Active tags, which have an internal energy source (e.g battery..) that allows the tag to send its own identification (ID) autonomously to the reader within a range of 100 m.
- ii) Passive tags, which require an external source to work. It uses the radio energy coming from the reader to reply to it. These tags have a lower cost, are generally smaller and have a virtually unlimited life expectancy, compared to active tags. The working range to respond to the reader is limited to 1 to 2 m.

Usually, most localization techniques rely on the installation of one or multiple readers on the mobile robot and on the distribution of RFID tags having known positions in the environment. The position is calculated by detecting radio signals from at least two known position tags. The authors in [Yang 13] discuss the shape density distribution of RFID tags in order to obtain performance with an improved accuracy of 10 cm. Measuring the received signal strength intensity [Park 13] or phase shift [Mart 16] of the RFID tags signals is another approach to obtain the position of the target. In [Mart 15], a combination of the two measurements (RSSI and phase and phase shift) is proposed to obtain a better average position estimation errors of 3.3 cm.

Ultra Wide Band (UWB)

The radio technology UWB is a wireless communication method having high speed and short range. This technology has been widely adopted through multiple applications and positioning systems due its profitably high bandwidth (more than 500 MHz) [Dabo 18]. The UWB signal is transmitted from a tag to an anchor. The time of flight that the signal takes to travel in the two directions is measured and divided by the velocity of the signal, in order to obtain the distance between the tag and the anchor. With at least three fixed anchors with known positions, the position of the mobile tag is obtained from ToA ore TDoA measurements.

Many advantages lie in the indoor use of UWB. For instance, indoor applications benefit from the absence of multipath effects (for having very short duration), negligible interference, high power of penetration, high positioning accuracy and data rates. UWB tags also profit from longer battery life and less power consumption. Furthermore, increasing the number of UWB sensors used along

with their own implementation is likely to prosper in various sectors. For example, improved accuracy of positioning is gained, the area of coverage is expanded, real time tracking is achieved, and the effect of signal limitation is highly reduced [Deak 12]. The average accuracy, achieved in [Dabo 18], is $100 \pm 25mm$ for range accuracy of $320 \pm 30mm$. Nevertheless, public UWB use may not be very feasible due to the fact that it is dependent of technologies which are not in accordance with the present standards. Besides the uncertainty of UWB public use, its use is relatively costly due to the large number of UWB sensors needed to ensure an improved performance in a wide region [Deak 12].

Magnetic positioning systems

The ancient magnetic positioning method proved to be still a subject of interest for position realization and tracking as stated in the studies of 1979 in [Raab 79]. This positioning method relies on applications of magnetic fields such as the earth's magnetic field and the compass [Li 12a].

The Magnetic positioning system is based on finding the position in the scope of a magnetic field through the use of magnetic signals.

The system is constituted of transmitters and receivers that are fixed and installed on the object to be tracked. The magnetic signals issued from the transmitter are received and transferred to a centralized location by the receivers to achieve position realization. On the other hand, systems exist that do not favor the usage of such devices. They, otherwise, benefit from magnetic properties present in elements such as steel structures, pillars, electrical power systems, electronic devices and different structures that adopt some form of magnetic field [Gozi 11]. Magnetic fingerprinting is categorized in the sector of studies in the magnetic positioning systems. The Non line-of-sight signal (NLOS) was the reason behind using fingerprinting. This sector was the subject of interest of various studies of researchers such as [Stor 10], [Zhan 17] and [Mont 16]. Storms et al. highlighted in [Stor 10], the peculiar attribute of the variations of the magnetic field within indoor environments obtain an approximate position and navigation trajectory of a vehicle. Kalman filter algorithms, three axis magnetometers, and the mapping of the intensities of the magnetic field within the environment are used to obtain a proper approximation of the position. This method provided acceptable results in the accuracy level of the system, nevertheless, the appearance of errors was inevitable especially upon using a map for the whole region.

Ultrasound

Ultrasound is a sound wave operating at high frequency, above 20 kHz, that humans are not able to hear, so it is not annoying. In fact, sound is a mechanical wave unlike electromagnetic waves, it produced by the vibration of materials. In

this sense, it is common to take advantage of the slow speed of propagation of ultrasonic signal to estimate its ToA between a transmitter node and a receiver node in a range of 10 m. The ToA measurement is then used to calculate the distance value between nodes considering the propagation speed of sound with a level of accuracy in centimeters [Medi 12].

Active Bat and Cricket are the most common ultrasonic localization and tracking systems. ActiveBat is an active ultrasonic positioning system where the infrastructure works as receiver and the mobile target transmits the signals, as shown in figure 1.7 (a). While for cricket the target is passive receiving signals from the infrastructure deployed in the environment, see figure 1.7 (b) [Bren 17].

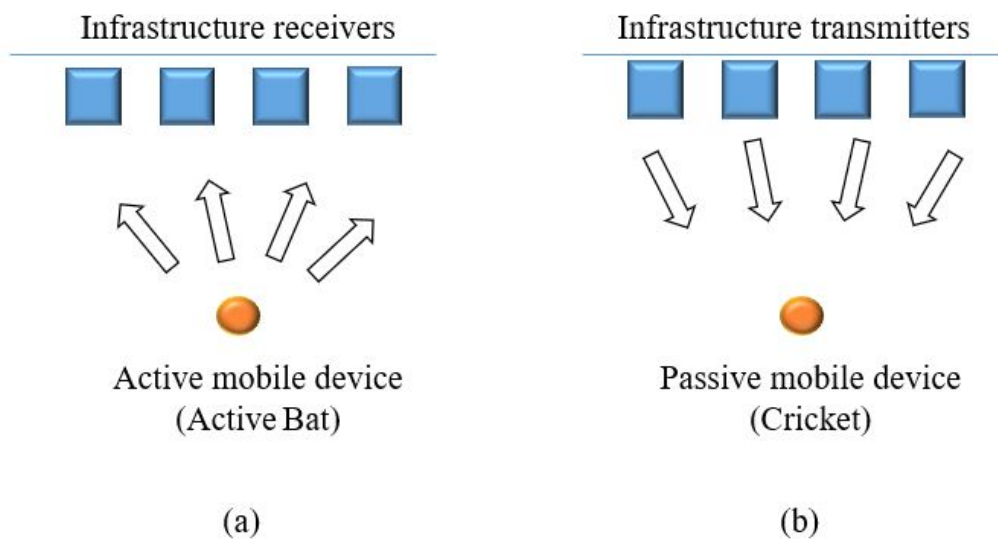


Figure 1.7: (a) Active Bat vs (b) Cricket architecture

These two methods are described below.

Active Bat

The Active Bat system consists of an arrangement of fixed microphones and a tag carrying user. The system is therefore active. The trilateration principle is used to calculate the user's location. In order to seek the user's position three or more microphones that receive sound pulses are needed. Taking into account that the sound transmitter is placed in front of the user, the direction in which the user is facing can be determined. This is achieved through collecting the data concerning the signal's relative strength in the array of microphones. The ultrasonic tags have properties such as being compact and a long batteries lifespan which makes them favorable to be carried by users. Thus users are spared the frequent battery

change. In addition, the Bat system is capable of localizing of more than 70 independent transmitters concurrently with a precision of the order of a couple of centimeters. This is because the receiver or sensor processes the signal one at a time and many tags will need to be deployed. Therefore, implementation on a large scale will degrade accuracy and performance due to noise and multipath effects [Sakp 17]. One disadvantage is that, as in most active systems, the location information is disclosed to the infrastructure administrators, creating a privacy risk. In spite of this, Woodman et al. developed a system in which the receiver is able to operate signals coming from the transmitters simultaneously in the absence of any interference threat [Wood 10].

The cricket

The cricket system combines the techniques of ultrasound and RF in order to achieve position realization on the mobile device which enhances user privacy. The cricket system adopts the techniques of ToA, TDoA and trilateration in the process of target location. Priyantha. et al launched the studies on the cricket system in 2000, [Priy 00]. The aim of establishing Cricket was to create a location assisting system for mobiles and for various indoor applications that engage with location. In short, the cricket system supplies devices with aid to determine their position rather than monitoring or tracking the user's location. For this means, there is no reason for having a position computation server. Even though, the accuracy of positioning of the system was acceptable over small ranges such as room level, on the larger scale the positioning accuracy failed to maintain its level. This is due to computational increase in the components and would hereby result in vulnerable performance.

As a conclusion, RF methods are widely used since their infrastructure is already available in the environment (Wi-Fi, FM, Bluetooth) or because they are inexpensive (RFID). In addition, they can localize in a wide range, with no need for LOS between the devices. The RF waves can also penetrate many materials. However, this method suffers from interference and electromagnetic noise and low accuracy. The remainder of the paragraph examines the optical methods developed in literature for localization and tracking application.

Such techniques are also more secure than RF since the light signal cannot penetrate the walls.

Visible light communication (VLC)

VLC is a free space wireless optical communication (OWC) technology that transmits data using visible light with wavelengths between 380 and 780nm. One of the visible light communication applications is the localization of a mobile target. Data can be transmitted using Compact Fluorescent Lamps (CFLs) or white LED lamps at 10 kb/s and 500 Mb/s respectively to one or multiple receivers, which may be a camera or photodiode placed in the environment. Using high frequency modulation signals will not be detected by human eyes, thus this application can be used to simultaneously for lighting and for locating the target [Grob 13].

In addition, VLC has a bandwidth larger than that of RF. However the communication needs a LOS between the light source and the sensors. Most of the studies focus on white LEDs over CFLs, because they have more benefits such as low power consumption of 100 mW, longer life time of 10 years with reliable illumination, high humidity tolerance, low cost, lower thermal generation and data modulation [Zhua 18], [Shar 17].

Usually the packet sent by the LED contains 30 bits composed of essential parameters such as ID, its coordinates, transmitted power in order that the receiver is able to calculate its distance to the LEDs. One of the localization algorithms: RSS, ToA or AoA serves to calculate the position of the target.

The architecture of VLC localization can be categorized as follows:

- Multiple light sources and one receiver
- One light source and multiple receivers
- One light source and one receiver

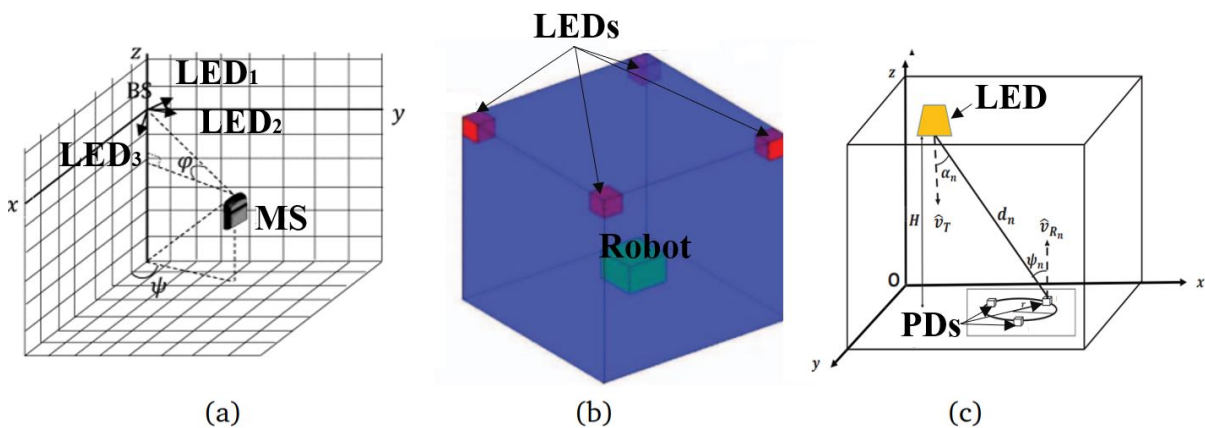


Figure 1.8: (a) Multiple LED 1 photodiode (PD) configuration [Erog 15] vs (b) multiple LED placed at the wall [Saab 16] (c) single LED vs multiple PD with a circular configuration [Naz 18]

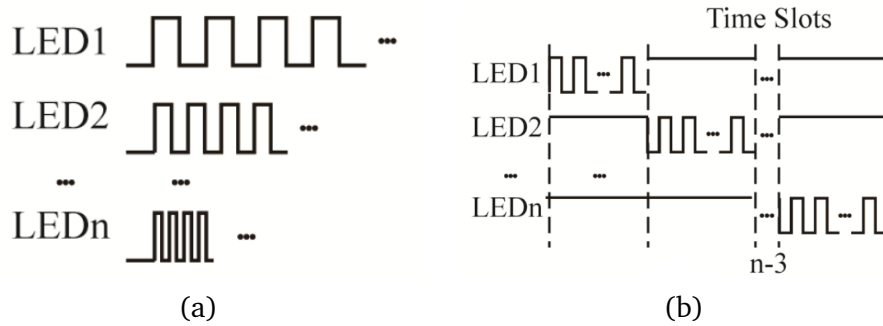


Figure 1.9: (a) FDM protocol vs (b) TDM [Zhua 18]

In the paragraph below, we will explain these 3 configurations.

Multiple light sources and one receiver

The most common VLC architecture is to have multiple LEDs mounted on the ceiling, at least two or more, and a single receiver, see figure 1.8 (a). In such a scenario, the receiver observes several transmitters at the same time. In another approach Saab et al., proposed to use the VLC technology without the need of a ceiling nor a grid of LEDs, see figure 1.8 (b) [Saab 16]. Instead, a single base station composed of the three or more LEDs each having its own orientation communicate horizontally with the photodiode (PD) mounted on the target. The localization was based on RSS method.

In VLC applications, multiplexing protocols such as frequency division multiplexing (FDM) and time division multiplexing (TDM), are needed to combine multiple signals into one signal on a common carrier. For FDM protocols, depending on the number of LEDs used in the application, the total available bandwidth is divided into a series of non-overlapping frequency sub-bands, where each is used to carry a separate signal for the corresponding LED, see figure 1.9 (a). For instance, Orthogonal Frequency-Division Multiplexing (OFDM) has been implemented in LED localization [32] in order to improve the autonomy of multi-access signals for FDM protocols. The OFDM is often used in wireless communication systems having RF basis, similar to current fourth generation (4G). Hindering factors such as narrow band interference and multi-path frequency-selective fading could be handled by OFDM through utilizing many near distant orthogonal signals. In [Erog 15], see figure 1.8 (a), they adopted the frequency multiplexing approach, where each LED has a proper identification ID with a known position which is sent to the receiver in a broadcast message. The ID is a specific frequency and by applying the AoA method the target position was calculated.

The TDM protocol divides the total time into multiple time slots. Each LED sig-

nal transmits its information in a time slot and synchronously switches at the end of the time slot so that the next LED starts the transmission, and so on, see figure 1.9 (b). However, several localization techniques based on LEDs that govern TDM protocols or ToA algorithms are impacted by defective synchronization between the LEDs and receivers. To serve the purpose of aiding the receiver and LEDs in modifying their clocks throughout the positioning, IEEE 802.15.7 adopts a synchronization header in the data frame. Total synchronization has been abandoned since the perception of a modified Additive Link Online Hawaii system (ALOHA) protocol, called Basic Framed Slotted ALOHA (BFSA). This sets the cornerstone for building a frame structure constituted of a known number of time slots exceeding the number of transmitters. In order to transmit data, every transmitter chooses a slot in a random manner within the frame length.

One light source and multiple receivers:

In this approach, the localization is based on the use of a single LED mounted on the ceiling communicating with several photodiodes placed on top of the target, see figure 1.8 (c) [Naz 18]. Localization is based on time difference of arrival (TDoA) for position estimation for different modes of distribution such as squares, hexagonal, circular. The photodiodes with circular pattern had the best accuracy with an order of millimeter which is close to the accuracy provided by multiple LED and a single PD attached to the receiver (Figure 1.8 (b)).

One light source and one receiver:

Using a single PD and a single LED it has been proved that it is technically impossible to achieve positioning, [Zhua 18]. To resolve this situation, research in [Li 14] mentioned the usage of inertial sensors for taking measures of the angles of incidence and irradiation upon the rotation of a smartphone. The concept lies in positioning the phone directly to face the light. At that particular position when the phone was placed horizontally, the RSS signal should be at its peak and hence the corresponding angle is the angle of incidence. Upon collecting this needed data and by using the model equation, the distance could be calculated. When facing the light, the direction of the smartphone was recorded using its internal compass. After measuring the distance and the direction, the location was then calculated. The drawbacks of this process are its complexity and the fact that it is time demanding. Besides the mentioned drawbacks, the performance was scaled to reach 95% below 1 m while that of the multiple LEDs locating system was 90% below 0.45 m. However, this process could be considered as a complementary

solution for robust circumstances, mostly in the the case were light sources are deficient.

Infrared

Infrared light is invisible to the human eye because its wavelengths are longer than those of visible light, making this technology less disturbing than indoor positioning based on visible light. Different approaches make use of infrared signals such as active IR beacons or passive IR sensors.

The active IR method is based on target holding active beacons that transmit IR signals towards fixed infrared receivers with predetermined positions. Both beacons and receivers are spread within an indoor environment. By trilateration, the unknown position is obtained. The ‘Active Badge’ System first deployed in 1992 is one of the most conventional and traditional IR indoor positioning systems modeled for the localization of people within the scope of a room [Want 97]. In fact, the members of the building work team hold ‘Active Bagdes’ emitting IR short pulses having distinctive codes and at a frequency of 0.07 Hz. The signals are received by an implemented IR receivers network inside the building. Through exploiting the principle of Cell of Origin, the positional accuracy of the ‘Active Badge’ system is controlled by the range of an IR sender of 6m. For the real time applications, the ‘Active Badge’ has a significant drawback due to its 15 s position update rate. The system’s model achieves the precise localization in rooms with a single receiver in each room. In the case of precision on the level of sub-rooms, a receiver with extra AoA potential is set [Maut].

A special application of infrared rays has been proposed in [Atsu 10]. The concept of the system relies on supplying angular related data in order to attenuate the sensor deviation of the integrating positioning systems. Polarized infrared light is used to obtain a proper approximation of the azimuth incidence angle relative to a single beacon. The beacon consists of an optical polarizing filter along with an infrared light source. The receiver is composed of a rotating polarizer and a photo-detector. The polarizer modulates the intensity of the signal based on the horizontal angle. As a result, the angle of the polarizing plane will describe the phase of the time dependent signal. This permits an approximation of the absolute angle of azimuth with an accuracy level of a few degrees accuracy in accordance with early experiments.

The textbook synonym of natural infrared radiation positioning has been described as a passive infrared localization system. Sensors that are able to process within the so called thermography region with spectrum of 8 μm to 15 μm make

use of the natural thermal emissions to provide a totally passive image of the surroundings [Haus 10]. Hence, using dedicated thermal sources such as active infrared illuminators is unnecessary. Thermal infrared radiation is capable of collecting the thermal degree of tagless individuals or objects placed at distance without any contact. The most common thermal detectors are represented by broadband detectors, thermocouples, thermal cameras and motion detecting pyroelectric infrared sensors.

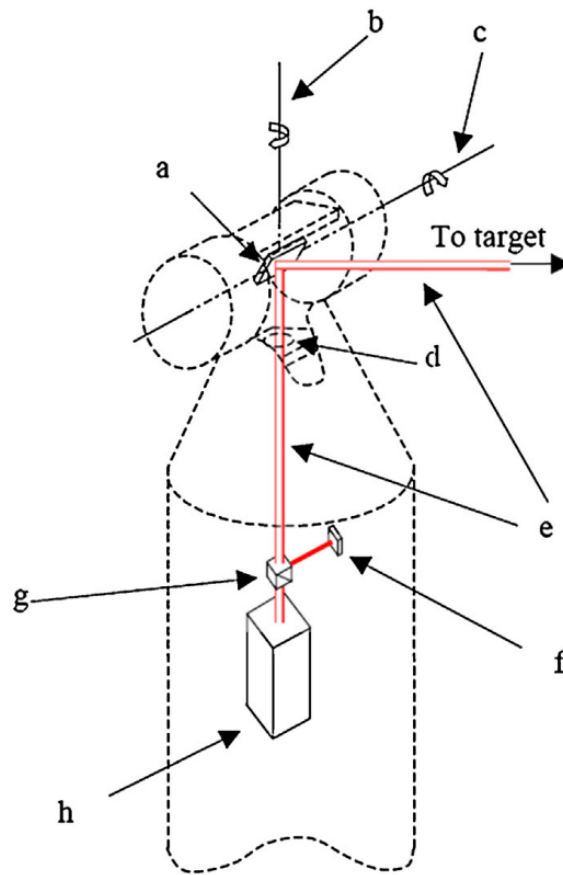
Emitter/Receiver system laser trackers (optical system)

Another approach is based on optical emitter/receiver system, where a laser scans the zone of interest to locate and track a mobile target holding a reflective element or an optical detector [Mura 16]. This method is applicable using visible or IR emitters/receivers. An example of the laser tracker architecture is presented in figure 1.10. A mirror rotating over two orthogonal axes (horizontal and vertical) steers the beam light coming from the laser toward the target. Once the laser reaches the target surface a retro-reflection occurs in the same incident direction, thanks to a retro reflective element placed on the target. This reflection is directed using a beam splitter towards a position sensing detector (PSD), which gives information on the spot position over its surface. In order to track the object, the mirror rotates to keep this reflection centered on the PSD surface. Usually, two angle encoders are mounted coaxially with the standing axis and the transit axis in order to read the horizontal and vertical angles of the mirror, respectively. By reading the angles, the position of the target can be obtained. The rotation of the mirror can be performed by using galvanometer motors, servomotors or by using a micro-electro-mechanical systems (MEMS) mirror.

Milanovic worked on the MEMSEye laser tracking technology. It uses two scanning MEMS mirrors, a modulated laser, and a photo sensor to localize and track the position of a retro-reflector marked object in a 3D plane [Mila 13a], [Mila 13b]. By using 2 MEMS mirror, the system localized and tracked a mobile retro-reflective element in 3D space. This retro-reflector can be placed on the object to be tracked. In this work the accuracy is approximately 1cm at a range of 50 m and 2.5 cm at 100 m.

Another approach of laser tracker is light detection and ranging (Lidar). This is a remote optical measurement method based on the analysis of the properties of a beam of light returned to its emitter. The distance between the Lidar device and the object is given by measuring the time between the emission of a pulse and the detection of its reflected pulse, knowing the speed of light. In [Hu 16], a spherical robot of 60 mm diameter is localized using 2D LIDAR rangefinder. The main aim of this work is to achieve an autonomous docking system, see figure

1.11, In which the robot is guided towards the base station. The Lidar system is added to the home station; since there is no place on the robot. In this work, the robot achieved parking within an accuracy of $\pm 10mm$ of the docking station's location, for a range of 0.06 to 1 m.



- a. Beam steering turning mirror
- b. Standing or vertical axis
- c. Horizontal or transit axis
- d. Cover plate
- e. Laser beam
- f. Position Sensing Device (PSD)
- g. Beam splitter
- h. Laser head

Figure 1.10: Architecture of the laser tracker principle [Mura 16]

Vision-based positioning systems

Vision-based positioning systems can be deployed in two different ways: either the camera is in motion and needs to be located, or the camera has a fixed position and is used to locate mobile targets (e.g, objects, people...) within the field of view, [Main 14]. The camera is used to locate the position of the pixel corresponding to the target's position in the image. By calibrating the camera and image real



Figure 1.11: Localization based on Lidar system [Hu 16]

position of the target can be obtained.

Furthermore, the vision-based system can be categorized into the following methods [Maut 11], [Maut]:

- i) Reference from 2D or 3D building models,
- ii) Image-based reference,
- iii) Coded target based reference,
- iv) Hybrid reference.

Reference from 2D or 3D building models

The 2D or 3D building models are based on comparing the image captured by a camera on the target object with an existing image in a database, where position information of the object is stored. The main advantage of this technique is that it does not require the implementation of infrastructures such as sensor beacons or target references. Kohoutek et al. worked on the city scheme and camera range sensor to obtain a digital spatio-semantic interior building design, [Koho 10]. The information extracted from the camera's range, based on time of flight, is compared to the city Geography Markup Language (GML) database. Depending on the properties of the captured object (quantities, dimensions and position), the matched room will be identified, see fig 1.12. The 3D camera's position is determined with an accuracy of 1 cm.

Image-based reference

For image-based reference, a moving camera in a certain path captures a number of sequential images, as seen in figure 1.13, and stores them in a database.

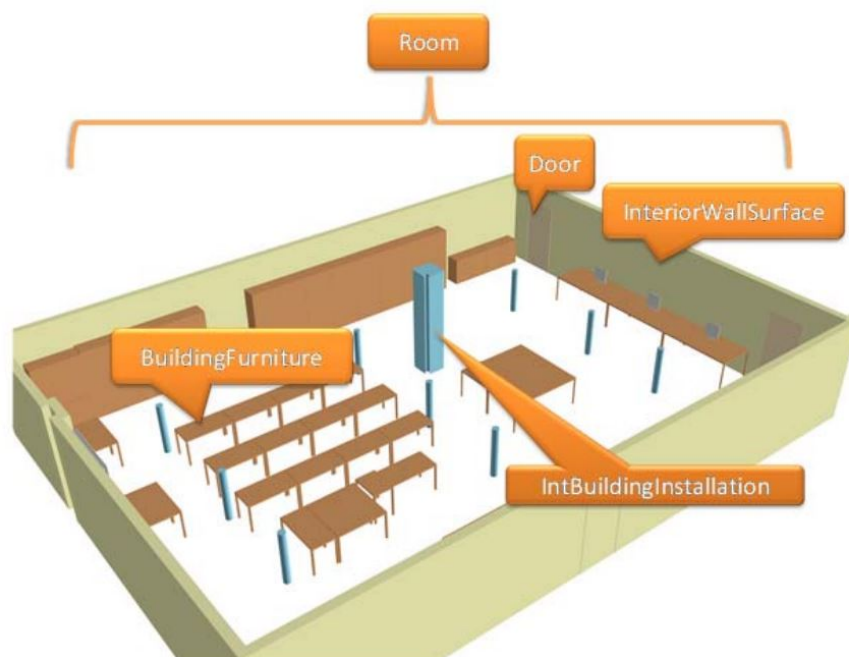


Figure 1.12: Model of a room in CityGML [Koho 10]

Afterwards, the current image is compared to the set database to determine the current view taken by the camera [Lian 13]. Muffert et al. determine the trajectory of an omnidirectional video camera based on relative camera orientation of consecutive images. If there is no additional control via other reference positions or directions, the recorded path drifts away from the true trajectory, similarly to inertial sensors relying merely on dead reckoning. For an acquisition time of 40 s, standard deviations of 0.09 degree are reported for tilt angles [Muff 10].



Figure 1.13: Example of vision based on image reference [Maut 11]

Coded target

The technique of coded target reference is based on using different markers such as bar-codes, concentric rings, colored dodes or retro-reflective objects to facilitate localization, see figure 1.14.

There are three motives for the use of markers in algorithm development:

- i) Reducing the complexity of automatic detection of corresponding points,
- ii) Initiating the system scale,
- iii) Differentiation and recognizing targets through utilizing a distinctive code for every maker.

In [Dand 18], a new control marker was designed in order to measure its position in addition to it's rotation, that can be used for surface reconstruction. An accuracy of ± 7 mm was deduced compared to the spatial polar method.



Figure 1.14: Four examples of coded targets used for point identification and camera calibration [Maut 11]

Hybrid

Hybrid positioning systems are based on associating multiple positioning technologies. Hybrid systems profit from the potential and strength points of two or multiple systems by combining their advantages in a complementary manner so as to compensate each system's constraints and weak points. By this method, hybrid systems surpass the restrictions of single model positioning technologies. This

method of merging yields improved accuracy, functionality and utility in the positioning system. In the case of the combination of two positioning systems, it may be possible to use either the better out of the two techniques uniquely or a combined positioning technique. The Cricket technology is one of the hybrid systems combining RF and Ultrasound, [Priy 00]. With the same concept, in [Nguy 16], a target position was also determined using RF and ultrasound in a 3D environment. Distances from the target to reference were calculated using TDoA principle. Then trilateration algorithms were applied to determine the target position.

An other hybrid relative positioning system of multiple robots is proposed in [Mao 13] using one infrared (IR) emitter, one IR receiver and one compass (magnetic sensor). An IR communication takes place between the robots and the distance between them is obtained by applying the Received Signal Strength (RSS) technique.

1.5.2 Micro-scale localization and tracking:

The main application fields of micro-scales localization are micro manufacturing, optical fiber alignment, bio-micro-surgery [Zhen 13], micro-assembly [Goze 12], atomic force microscopy (AFM) [Yan 10] and scanning tunnel microscopy (STM) [Taja 18].

Two main categories of sensors are distinguished when it comes to measurements at the micrometric scale: electromagnetic sensors and optical sensors, [Bell 09], [De S 15]. Electromagnetic sensors measure the displacement of an object by observing variations in current or magnetic field as they occur, of which we mention, capacitive sensors. In [Clar 16] the resolution reached is of sub-nanometer in a range of 100 μm for the parallel plate capacitors and 5 mrad for the angular measurement which causes non linearity. However, such a technique demands high installation requirements and needs multiple sensors for multiple axes.

Optical sensors are non-contact sensors that exploit variations in the optical perception of a movement. These include laser triangulation sensors. In [Guo 15], three laser range displacements are used to measure the real-time motion of a mobile platform. Two of them are dedicated to the measurement of the translation in x -axis and the rotation around z -axis. The third is dedicated to y -axis measurement. With a range of 12 μm of displacement, a resolution of 0.1 μm was obtained for a circular path of a radius of 5 μm .

There also exist micro-vision based systems that depend on using a camera that captures movements in multiple axes, unlike previous methods that deploy sensors for every single axis. Such micro-vision based systems also hold another advantage over the previous methods through their remote contactless nature that eliminates the possibility of measurement contact errors. A single camera can be enough to

recognize the placement of an object with a performance similar to that of conventional sensors (capacitive, inductive, optical, etc.). Nevertheless, the non-contact aspect, the remote placement, the multi-DOF measurement or simply an interface should be implemented to control the robot. Vision displacement measurement can be sorted into two broad categories [Guel 17]: pixel and structure methods. Pixel methods are based on the study of images from the point of view of the intensity of their pixels, without prior information on their distribution. They can be applied to any image or, at least, to any image with certain defined properties. Lu [Lu 11] applies, for example, a method of motion estimation based on the gradient of the image on the micrometer scale. Here applied to a displacement of 3 μm , this method makes it possible to obtain a measurement with an error of less than 15 nm.

Structural methods look for precise structural information (pattern) within images, in other words, primitives such as points, corners or straight lines, or even objects clearly identified as belonging to this type of image. These methods therefore require an extra step: the detection of elements to be associated (which must certainly be present in the image). Once the elements have been extracted, all that remains is to associate them via their spatial relationships, [Guel 17]. In [Guel 16], the position is obtained by using a pseudo-periodic pattern observed by a regular visual setup. This micrometric pattern corresponds to the intertwining of two perpendicular copies of a single-axis pattern made of two spatial frequency carriers with slightly different periods. Over a range of 221 μm , a resolution below 0.5 nm is demonstrated by the use of 2000 images for a video rate of 30 frame per second (fps).

1.6 Conclusion

In this chapter, several localization methods such as proximity, trilateration and scene analysis were presented and described. A comparison study was made to reveal the pros and cons of each method. In addition, some performance parameters that qualify positioning and tracking methods were listed. Finally, a bibliography study on different localization and tracking systems for macro and micro scales was presented. The functionality principle of each of the methods was also discussed.

Table 1.2 sums up the different localization and tracking methods in the macro and micro scales displaying the accuracy and the corresponding range. As seen, the accuracy decreases as the range expands. High accuracies of nm are obtained for micro-scaled systems having a narrow range of μm . In this work, the aim is to develop a method, based on an emitter/receiver technology, to achieve localization and tracking with an accuracy of μm and within a relatively large range (meso-

scale, hundreds of mm for example).

Table 1.2: Comparison between the different localization systems

Technology	Range	Accuracy
UWB	10-20 cm	less than 10 cm
WLAN/wifi	10 m -100 m	1 m
Bluetooth	100 m	1 m
RFID	1 m -50 m	dm - m
Magnetic	1 m - 20 m	mm - cm
Ultrasound	10 m	less than 10cm
VLC	m	cm
Infrared	1 m-5 m	cm -m
E/R	m	cm
Vision camera	1m - 10 m	0.1 mm - dm
Micro-applications	μm	nm

Figure 1.15 represents the outline that illustrates graphically the coverage variation of various methods in function of accuracy. As displayed, the proposed thesis offers a practical and intermediate solution that is farther and more fruitful than the conventional methods.

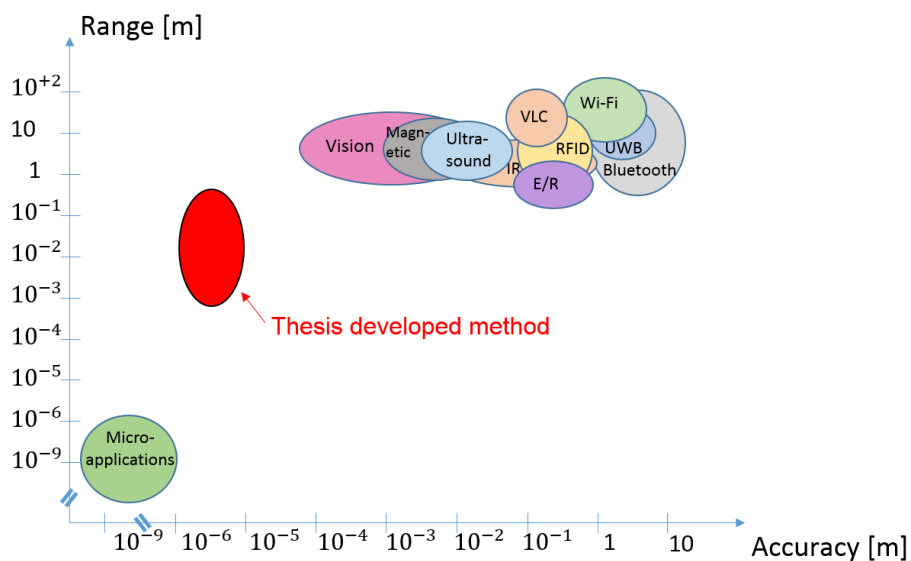


Figure 1.15: Graphical overview for the range versus accuracy of the localization methods in the literature compared to the method proposed in this thesis

Chapter 2

Modeling of the optical localization and tracking method

2.1 Introduction

Over the past years, positioning systems have served in several fields such as engineering and science, gaining the attention of researchers and development centers. Numerous studies have made it possible to determine the real-time position of objects or individuals at different scales, as listed in chapter 1. Depending on the application, the scale varies from macro to nano levels. However, for a large scale the positioning accuracy is reduced. In this chapter, we propose a 2D optical localization and tracking method to localize mobile objects moving freely over a large surface, called here the conveying surface, but with a high relative resolution compared to the large scale of displacement. This method uses optical emitter/receiver devices coupled with a scanning system. The emitter is a laser source that scans the surface, using a beam steering device, in order to locate a target to be tracked, while analyzing the signals generated from an optical sensor, called photo-detector.

This chapter begins with a system description of the localization and tracking method in section 2.2. In section 2.3 an optical model is developed to achieve the objective of our optical localization and tracing method. In addition to the presentation of a mathematical model, a study of the system dimensions is proposed. Then, in section 2.4, the scanning phase is outlined and the different types of steering devices are listed. Finally, in section 2.5, the different types of photo-detectors and their functionalities are introduced and discussed.

2.2 System architecture for localization and tracking

The proposed localization and tracking method for a mobile target is based on the detection and analysis of a light beam reflected from its surface. A fixed laser diode scans the conveying surface, where the target moves, using a 2D steering device. The target is localized when the laser beam reaches the surface, where the target and the steered beam has the same line of sight (LOS). A retro-reflective element (corner cube reflector (CCR) or tape reflector) is placed onto the target surface to reflect the light, in the reverse incident direction, towards an optical photo-detector. The latter converts the received light into an electrical signal. In such a scenario, there is no need for triangulation or multiple laser beams to determine the position of the target, since the reflection has the same incident direction thus, the target position can be known from the steering device orientation. The tracking is achieved when the steering device rotates to follow the motion target over the conveying surface, in order to maintain the LOS between them. A position sensing detector (PSD) is adopted as the optical photo-detector that receives the reflected beam light coming from the target. PSD can be either a QPD or LEP (,see paragraph 2.5). A PSD provides direct information on the position of the light spot received on its active surface. The aim of tracking is to keep this spot light centralized over the PSD's active surface. When the localized target moves, the PSD detects a variation in the position of the light received on its surface. Thus, in a closed-loop control system, the orientation of the steering device is controlled by to the output signals generated by the PSD, in order to follow the new target position so that the PSD continues to receive a centralized light spot.

In the rest of this section, a more detailed description of the localization and tracking method is presented.

2.2.1 Localization phase description

The main elements used for the optical localization system are: laser diode, steering device, retro-reflective element, PSD and a beam splitter. The wavelength of the laser diode can be visible or IR, on condition that the PSD used can respond to it. The role of the steering device is to scan the surface by directing light coming from the laser source to the conveying surface. The corner cube reflector (CCR) is the retro-reflective element placed on the target, in order to provide reflection parallel to the incident beam. The CCR is a trihedral prism made up of three adjacent, mutually orthogonal and reflective intersecting surfaces, see figure 2.1 (a). As shown in this figure, regardless of the orientation of the prism and the incident beam, the reflected beam is parallel to the latter. The reflected beam is shifted

from the incident beam by a distance that depends on the position at which the incident beam touches the entrance surface of the CCR. The maximum value of the shifted distance is equal to the diameter of the corner cube (denoted D_{CCR}), in the case where the incident beam hits the edge of the corner cube reflector.

The beam splitter is an optical component used to divide incident light into reflected and transmitted beams of a specific ratio of (50%/50% or 90%/10%), see figure 2.1 (b). Here, the beam splitter is used in both directions. For example, in figure 2.1 (b), the beam noted as input I corresponds to the laser source which is divided into two parts. The first is transmitted and denoted by beam III, while the second is reflected and denoted by beam II. In our case beam III is directed to the steering device, while beam II is not used. For the other side, input I' is the reflected light coming from the corner cube that will be split again to the reflected beam II' and transmitted beam III'. II' is directed towards the PSD and III' is considered lost. For such a configuration, the beam splitter with the ratio (50%, 50%) is the one adopted so that the PSD, theoretically without taking into account the other loss factors, receives 0.25% of the initial power, instead of the ratio (90%, 10%) giving a percentage of 0.09%.

Figure 2.2, illustrates the proposed architecture for localization, having the following sequential procedure order:

First, the light beam, coming from the laser source and reflected by the surface of the steering device, is directed towards the target's surface (steps 1, 2 and 3 or 3'). Each orientation of the steering device corresponds to a spot position on the conveying surface. The orientation I of the steering device does not reach the mobile target (i.e, conveyor), thus beam 3' is not reflected back through the PSD. Therefore, the steering device continues to change its orientation until orientation II, where beam 3 reaches the target.

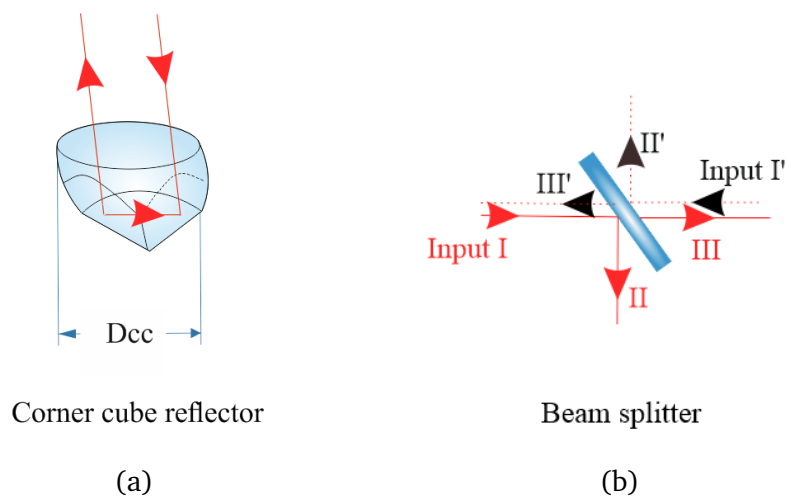
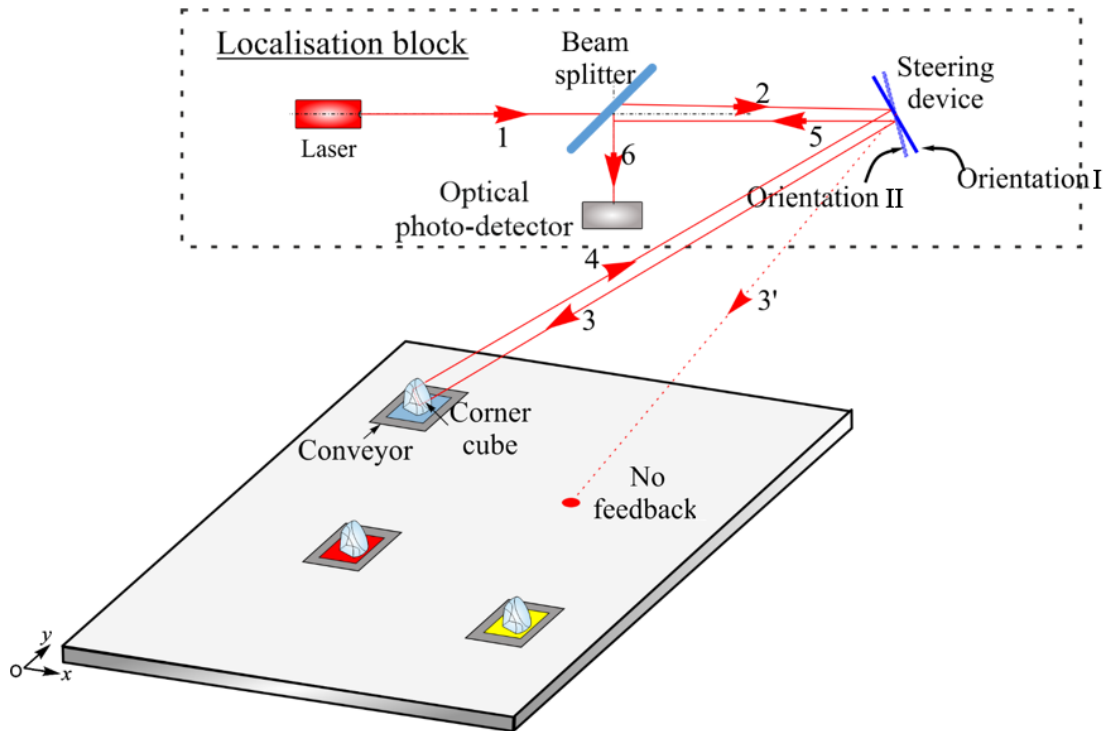


Figure 2.1: Working principle of (a) a corner cube reflector and (b) a beam splitter



- Beam number 1: from source to beam splitter
- Beam number 2: from beam splitter to steering device
- Beam number 3: from steering device to CCR
- Beam number 4: from CCR to steering device
- Beam number 5: from steering device to beam splitter
- Beam number 6: from beam splitter to PSD

Figure 2.2: Schematic layout of the proposed localization architecture

There, the passive CCR reflects the beam towards the optical receiver (step 4). Reflected light beam number 4 is transmitted towards a fixed PSD, through the beam splitter (step 5 and 6). By analyzing the detected signal after a reflection on the steering device, the target can be localized. Once the localization is performed, the tracking phase will be launched. The following section describes the proposed tracking method.

2.2.2 Tracking phase description

As mentioned above, the optical photo-detector that receives the reflected beam 6, has to be a position sensor detector (PSD), in order to track the movement of the localized target. When the localized CCR (i.e, the target) moves, the PSD can detect a variation in the position of spot 6 on its active surface.

The goal of tracking the mobile target, is to keep this spot centered on the PSD surface, through controlling the steering device orientation. To do so, the proposed tracking method consists of scanning the conveying surface with a light

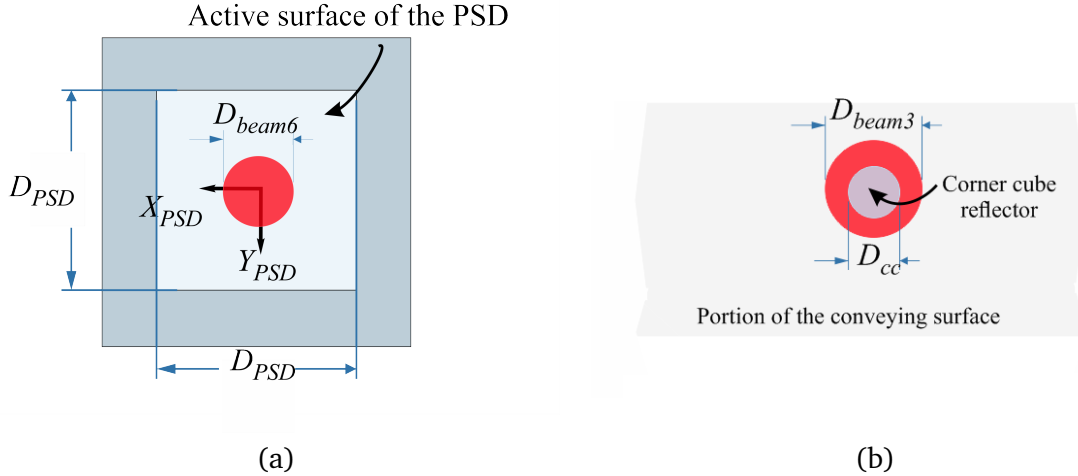


Figure 2.3: Top view (a) of the PSD and (b) conveying surface, where the system is optically centralized

spot having a diameter (D_{beam3}) larger than that of the CCR (D_{CCR}). In such a way, the PSD detects the movement of the CCR inside the beam spot 3. The coordinates of this point with respect to the center of the PSD are noted x_{PSD} and y_{PSD} and vary between $[-\frac{D_{PSD}}{2}, \frac{D_{PSD}}{2}]$, where D_{PSD} is the diameter of the active surface of the PSD. The obtained values of x_{PSD} and y_{PSD} give a direct information of the corner cube reflector's position inside the light spot number 3. For example, x_{PSD} and y_{PSD} theoretically equal to zero, which means that beam number 6 is centered on the active surface plane of the PSD, as shown in figure 2.3(a), implies that the position of the corner cube reflector is in the center of spot beam number 3 over the conveying surface, see Fig. 2.3(b). If the corner cube reflector changes position, i.e. the target moves, the CCR is no longer centered with spot 3, and, as a consequence the values of x_{PSD} and y_{PSD} are no longer zero. Next, the steering device is re-oriented in accordance with these values of (x_{PSD} and y_{PSD}), in such a way to return the CCR at the center of spot 3. As a result, the corner cube reflector remains centered inside the movable light spot 3 for any new position of the target on the surface.

Furthermore, a model for our system must be proposed and dimensioned conveniently to fulfill the project's aim. The next paragraph provides detailed description of the design and conception of our proposed tracking technique.

2.3 System modeling of the localization and tracking method

The purpose of this section is to find the optical model that allows to scan the surface in an appropriate manner, to ensure its reliability in localization and tracking

the mobile target moving over the conveying surface.

The section's goal is also to find the equation of the spot size received on the conveying surface (D_{beam3}), the sensitivity of the tracking system and to calculate the size of the covered scanning surface, as a function of the steering device's rotation angles. There are two ways to scan the surface, either with a collimated beam or with a non collimated one. In the case of scanning the surface with a collimated laser source having a beam diameter equal to (D_{beamS}), the latter should satisfy different optimization constraints such as:

1. D_{beamS} should be equal to or less than the diameter of the steering device, in order to reflect all incident light without any loss of optical power.
2. D_{beamS} must be larger than the diameter of the corner cube reflector in order to detect its movement inside the spot light of beam number 3, see fig. 2.3(b).
3. D_{beamS} should be equal to the desired value D_{beam6} received on the surface of the optical detector, see fig. 2.3(a).

The method of using two converging lenses in a telescope arrangement can be adopted to adjust the size of D_{beamS} to meet the above constraints, see Fig.2.4. If the first lens has a focal length (F') greater than that of the second lens (F''), the diameter of the D_{beamS} will be reduced. In the second case, where F' is less than F'' , D_{beamS} will be enlarged. The new diameter will be equal:

$$New D_{beamS} = D_{beamS} \times \frac{F''}{F'} \quad (2.1)$$

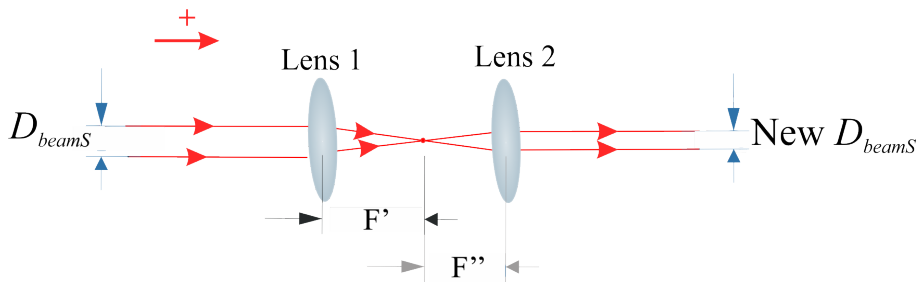


Figure 2.4: Two lenses methodology for changing beam width value

However, the method of scanning the surface with a collimated laser beam cannot be adopted, due to the complexity of satisfying all of the above constraints, where each beam (from 1 to 6) cannot have the same diameter width. In addition, placing optical components such as convergent lens or divergent lens, after the steering device, causes the surface scanning to be limited by the diameter of lenses.

Therefore, a second approach was implemented, which consists in scanning the conveying surface with a non-collimated light beam. In such a scenario, two lenses will be added to the system. The first is placed between the beam splitter and the steering device and the second between the beam splitter and the photo-detector, in order to adjust the beam width to the desired diameter value.

Fig. 2.5 (a) shows the proposed system architecture, during the scanning phase, with more detail compared to figure 2.2, where two lenses are added in front of the steering device and the PSD, respectively. In fact, a converging lens is employed to focus the light on the center of the steering device, as seen in figure 2.5. Our architecture is, thus, generalized to be adopted for all sizes of the steering device. In such a scenario, the spot size obtained on the conveying surface (D_{beam3}) depends on the focal length value of the convergent lens used, in addition to the elevation of the steering device with respect to the conveying surface, the rotation angles of the mirror and the width of the source beam (more details on how to obtain this relation is presented in section 2.3.1). A lens 2 is placed in front of the PSD to ensure that the received beam (6) on the PSD's active surface has the desired radius value, more details on the choice of radius are presented in section 2.5. The selected PSD and the distance between it and the lens having a certain focal length, determines whether a convergent or a divergent lens has been used. As for the position of the beam splitter, the best arrangement is to place it between the laser and the steering device, as seen in figure 2.5 (a), so that the beam number (6) depends solely on the movement of the corner cube reflector in the spot. For each position of the corner cube reflector inside the light spot, the reflection beam number 4 will be directed to a specific position on the active surface of the PSD. Consequently, any movement of the corner cube reflector within the spot will be detected by the optical sensor. Otherwise, if the beam splitter is placed between the corner cube reflector and the steering device, reflected beam (6) depends on the position of the light spot over the entire conveying surface [Mala 18].

Figure 2.5, illustrates a tracking representation on one axis (1D) associated with the analysis of the variation of beam position over the PSD active surface plane, relatively to different corner cube reflector positions on the conveying surface. As mentioned above, figure 2.5 (a) represents the scanning phase, where the corner cube reflector is not yet lit by the incident beam, so that no reflection onto the PSD has occurred. In this case the CCR has a position 0 and the steering device orientation 1. In figure 2.5 (b), the PSD is set to a fixed default position that corresponds to the corner cube reflector being at the center of the light spot, position 1. First, at this default position, the reflected beam number 6 will evidently be at the PSD's center so x_{PSD} will be equal zero. When the corner cube

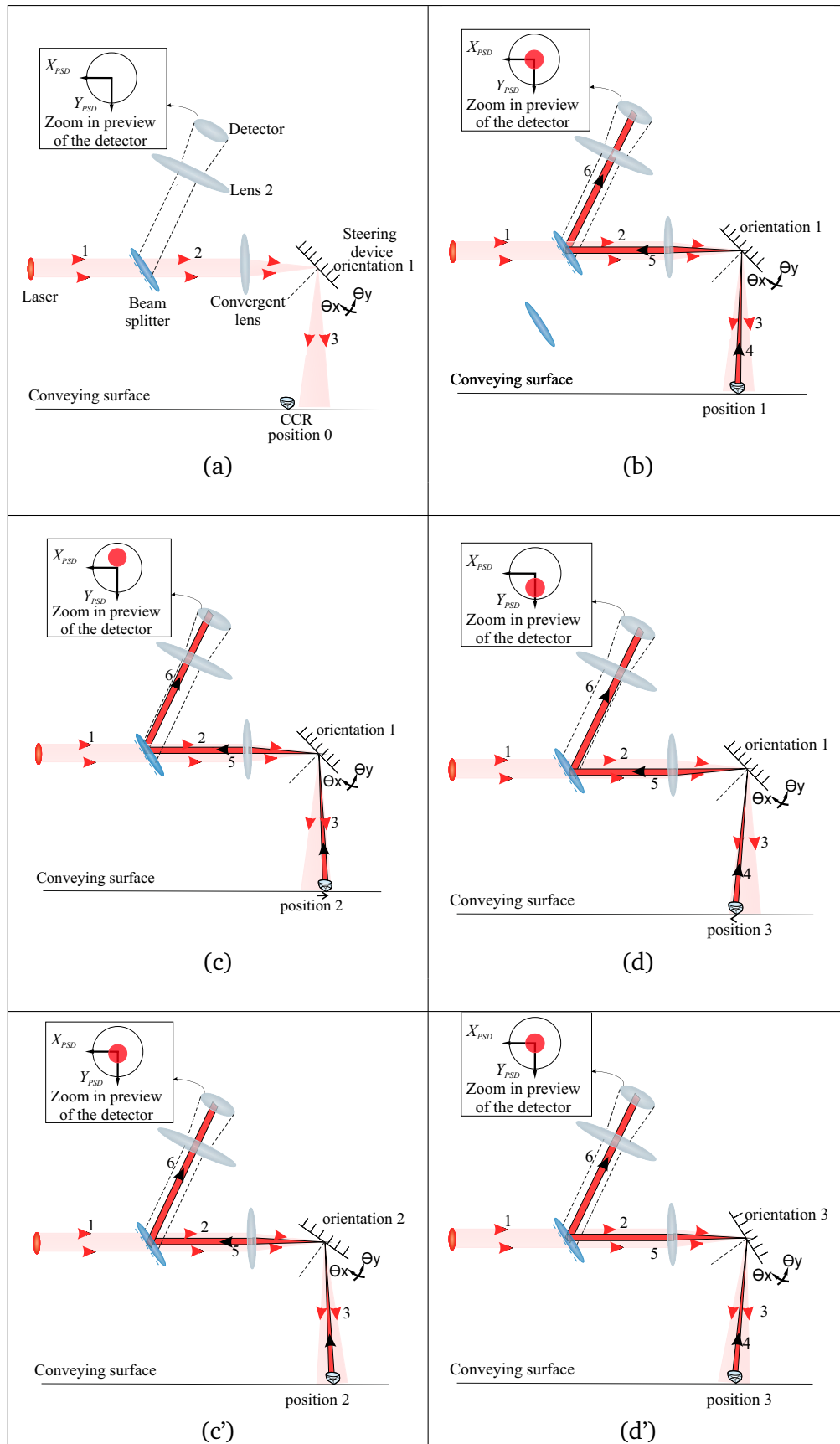


Figure 2.5: Demonstration of the tracking in one axis for different corner cube's position giving different x_{PSD} values, (a) incident beam trajectory in absence of corner cube, (b) centralized beam $x_{PSD} = 0$, (c) $x_{PSD} < 0$, (d) $x_{PSD} > 0$ and for (c')(d') giving new orientation of the steering device to re-obtain $x_{PSD} = 0$

reflector, i.e. the target, moves to the right from position 1 to position 2 (respectively left, from position 1 to position 3), as a consequence the reflected beam 6 moves and the x_{PSD} value increases (decreases), as seen in Fig. 2.5, (c and d). In a closed-loop control, the system corrects the orientation of the steering device to follow the new position of the corner cube reflector, so that x_{PSD} returns to zero and the corner cube reflector is back once again in the center of the light spot, as seen in figure 2.5 (c' and d'). In this example, the steering device rotates from orientation 1 to 2, for the case the CCR moved to the right, as seen figure 2.5 (c and c'), respectively. In addition, the steering device rotates from position 1 to 3, when the CCR moves to the left, as shown in figure 2.5 (d and d'), respectively. The same study is carried out for the other axis. Thus, a 2D tracking of the target is achieved and the system is able to track the target during its 2D movement over the conveying surface.

2.3.1 Dimensioning of the tracking system

This section focuses on the calculation of the spot diameter, coverage surface and system sensitivity in one dimension. This study is sufficient to define the 2D system. In the following example the abscissa axis is the one adopted. Fig. 2.6 is a model representation of our system showing the fixed part composed of the convergent lens and the incident beam light coming from the source and actuated and mobile parts composed of the steering device that reflects the light over the conveying surface in different directions. The relationship of D_{beam3} can be extracted, using the geometric model and trigonometric equations in a triangle, as a function of the mirror elevation with respect to the conveying surface (Hei), the focal length of the convergent lens ($\overline{O_1F'_1}$), beam width of the source beam light D_{beamS} and the angle of rotation of the steering device (θ_x). In fact, θ_x is the angle formed between the normal to the convergent lens ($\overline{O_1F'_1}$) and the normal of the steering device and (D_{beam3}) can be expressed as follows:

$$D_{beam3} = \overline{BA} = \overline{BO} + \overline{OA} \quad (2.2)$$

Where B and A are the two point extremities of the light spot of the left and right side of the spot, respectively. The normal projection of the focal point F_1 on the conveying surface corresponds to the center denoted as the point O. In order to

have a symmetric scanning over the conveying surface, the point O is considered as center of origin of abscissa for the scanning.

For real application conditions, θ_x is between 0 deg and 90 deg, and equal to:

$$\theta_x = \theta_{x0} \pm \Delta\theta_x \quad (2.3)$$

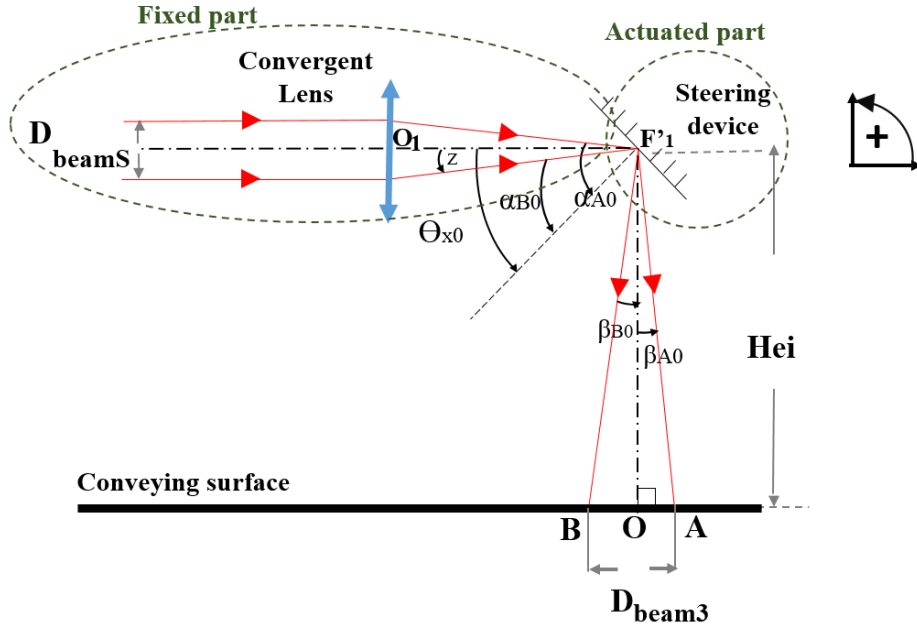


Figure 2.6: Model representation of the optical system where the center of the light spot is at the origin of the surface O

$\Delta\theta_x$ is the angle variation of the steering device and θ_{x0} is the initial position of the steering device. In Fig. 2.6, $\theta_x = \theta_{x0}$ and $\Delta\theta_x = 0$ giving that the steering device is at its initial position. In this case, the origin O is the center of the beam of diameter AB having a minimum spot size.

For such configuration, θ_{x0} is equal to:

$$\theta_{x0} = z + \alpha_{B0} = \alpha_{A0} - z = 45 \text{ deg} \quad (2.4)$$

Where α_B and α_A represent the angle formed by the normal of the steering device and the spot rays as shown in figure 2.6. $2z$ is the incident angle with respect to the steering device. In addition, the value $2z$ is equal to $\widehat{BF_1A} = \beta_B + \beta_A$ due to Fermat's principles (reflection law).

β_B and β_A are the angles formed by the normal of the conveying surface at the point O and the extremity of spot rays $F_1'B$ and $F_1'A$, respectively. In figure 2.6, $\beta_{A0} = \beta_{B0} = z$.

Thus, the normal of the steering device is the bisector of the right angle $\widehat{O_1F'_1O} = 2\alpha_{B0} + 2z = 90$ deg resulting to a θ_{x0} equal to 45 deg.

In order to calculate the minimum spot dimension $D_{beam3\ min}$ for θ_{x0} equal to 45 deg, the values of OB and OA need to be extracted. Note that the absolute value of an algebraic distance, for example $\|\overline{OB}\|$, is simplified here to be written as OB . By applying the rectangular triangle theorem in the triangles (F'_1OB) and (F'_1OA) , OB and OA can be expressed, respectively, as follows:

$$OB = Hei. \tan(\beta_{B0}) \quad (2.5)$$

$$OA = Hei. \tan(\beta_{A0}) \quad (2.6)$$

Thus, $D_{beam3\ min}$ is equal to:

$$D_{beam3\ min} = OA + OB = Hei(\tan(\beta_B) + \tan(\beta_A)) \quad (2.7)$$

In addition as seen in figure 2.6, β_B and β_A are equal to the angle z . From trigonometric formulas, z is written as:

$$z = \arctan\left(\frac{D_{beamS}}{O_1F'_1}\right) \quad (2.8)$$

Implies:

$$D_{beam3\ min} = OA + OB = 2 \tan(z) \times Hei = \frac{D_{beamS} \times Hei}{O_1F'_1} \quad (2.9)$$

For D_{beam3} equal to $\overline{BA} = \overline{OA} - \overline{OB}$ and having O as origin of abscissa, there exists 3 cases for the model:

- case 1: points A and B are both in the positive abscissa
- case 2: points A and B are both in the negative abscissa
- case 3: points B is at negative and A is at positive abscissa

For each of the above cases, we will find the corresponding interval θ_x by studying the limits where points A and B are superimposed with O, respectively.

If point A is superimposed on O, i. e. $D_{beam3} = BA = BO$, the steering device is turned in the direction $-\Delta\theta_x$ until β_A becomes zero and $\beta_B = 2z$, see fig. 2.7. The values of the angles θ_x , α_B and α_A decrease with an angle $\Delta\theta_x$, giving :

$$\theta_x = \theta_{x0} - \Delta\theta_x \quad (2.10)$$

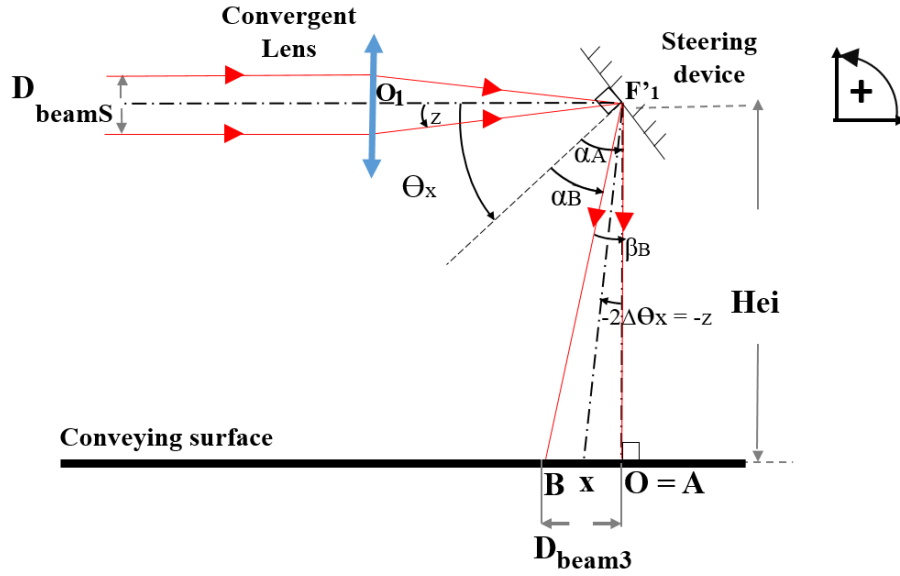


Figure 2.7: Model representation of the optical system where the origin of the surface O superimposed on the end point A of the light beam

$$\alpha_A = \alpha_{A0} - \Delta\theta_x \quad (2.11)$$

$$\alpha_B = \alpha_{B0} - \Delta\theta_x \quad (2.12)$$

From the angle $\widehat{O_1 F'_1 O} = \widehat{O_1 F'_1 A} = 90 \text{ deg}$, we can continue with:

$$\theta_x + \alpha_A = 90 \quad (2.13)$$

From equations 2.10 and 2.11, we obtain the expression of $\Delta\theta_x$ as follow:

$$\theta_{x0} - \Delta\theta_x + \alpha_{A0} - \Delta\theta_x = 90 \quad (2.14)$$

$$\Delta\theta_x = \frac{\theta_{x0} + \alpha_{A0} - 90}{2} \quad (2.15)$$

using equation 2.4,

$$\Delta\theta_x = \frac{\theta_{x0} + \theta_{x0} - 90 + z}{2} \quad (2.16)$$

$$= \frac{z}{2} \quad (2.17)$$

From this equation, we can verify that if the steering device rotates by an angle of $\Delta\theta_x$, the center of beam light rotates of an angle $2\Delta\theta_x$.

Equation 2.10 can be rewritten as:

$$\theta_x = \theta_{x0} - \frac{z}{2} \quad (2.18)$$

For the case where the mirror is at rest position $\theta_x = 45deg$, and if the steering device rotates more than $\frac{z}{2}$, both points A and B will be in the positive abscissa. Thus, case 1 corresponds to the case where θ_x limit lies between 0 and $\frac{z}{2}$.

Similarly, when point B superimposed on the point O, $D_{beam3} = BA = OA$. The steering device rotates in the positive direction. The angles β_B and β_A are equal to zero and $2z$, respectively, see figure 2.8. The values of θ_x , α_A and α_B increase by $\Delta\theta_x$, resulting the following equations:

$$\theta_x = \theta_{x0} + \Delta\theta_x \quad (2.19)$$

$$\alpha_A = \alpha_{A0} + \Delta\theta_x \quad (2.20)$$

$$\alpha_B = \alpha_{B0} + \Delta\theta_x \quad (2.21)$$

The right angle $\widehat{O_1F_1'O}$, which is also equal to $\widehat{O_1F_1'B}$ allows us to write:

$$\theta_x + \alpha_B = 90 \quad (2.22)$$

From 2.19 and 2.21:

$$\theta_{x0} + \Delta\theta_x + \alpha_{B0} + \Delta\theta_x = 90 \quad (2.23)$$

$$\Delta\theta_x = \frac{-\theta_{x0} - \alpha_{B0} + 90}{2} \quad (2.24)$$

Using equation 2.4,

$$\Delta\theta_x = \frac{-\theta_{x0} - \theta_{x0} + 90 + z}{2} \quad (2.25)$$

$$= \frac{z}{2} \quad (2.26)$$

Equation 2.19 can be rewritten as:

$$\theta_x = \theta_{x0} + \frac{z}{2} \quad (2.27)$$

The value of θ_x for case 2 is between $[\theta_{x0} + \frac{z}{2}]$ and 90 deg, where the points A and B are on the negative abscissa. The remaining interval corresponds to the third case where θ_x is between $[\theta_{x0} - \frac{z}{2}]$ and $[\theta_{x0} + \frac{z}{2}]$. Point A is in the positive abscissa while point B is in the negative abscissa.

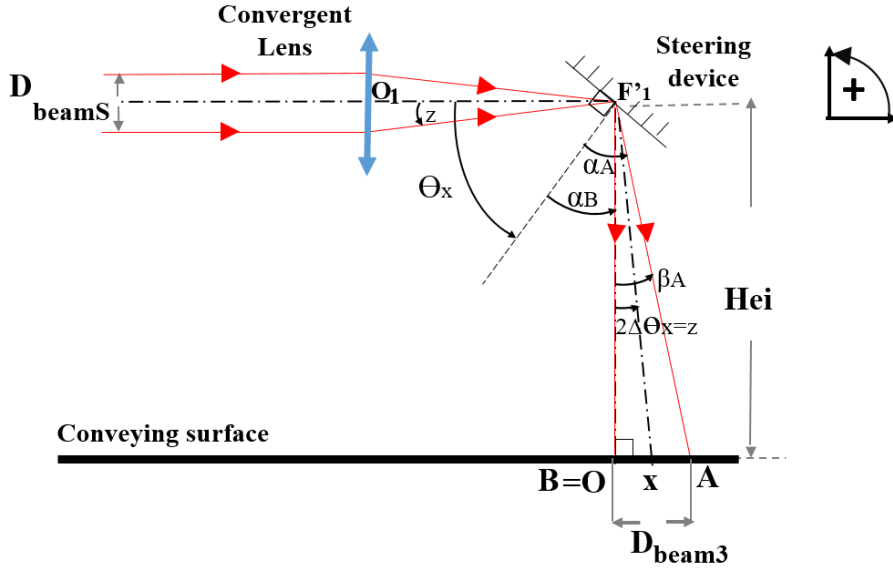


Figure 2.8: Model representation of the optical system where the origin of the surface O superimposed on the end point B of the light beam

After obtaining the range of values of θ_x for each case, the next step is to find the function D_{beam3} from the measurement of OA and OB . Taking the case of Fig. 2.9, where the mirror rotates by $+\Delta\theta_x$. The corresponding values of β_B and β_A are equal to:

$$\beta_B = 2\Delta\theta_x - z \quad (2.28)$$

$$\beta_A = 2\Delta\theta_x + z \quad (2.29)$$

By replacing z with its value from equation 2.8 and by extracting the values of OA and OB from the angles β_A and β_B , respectively, using the equations 2.6 and 2.5, D_{beam3} can be written as follows:

$$D_{beam3} = \overline{BO} + \overline{OA} = \overline{BA}$$

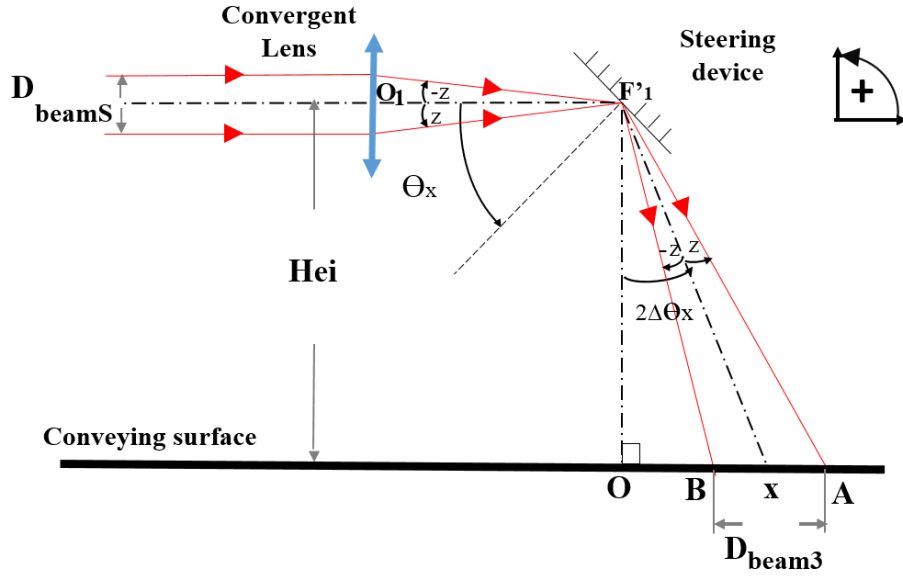


Figure 2.9: Model representation of the optical system for a general case where the spot is at the positive abscissa of the surface

$$D_{beam3} = -Hei \times \left[\tan \left(2\Delta\theta_x - \arctan \left(\frac{D_{beamS}}{2O_1F'_1} \right) \right) + \tan \left(2\Delta\theta_x + \arctan \left(\frac{D_{beamS}}{2O_1F'_1} \right) \right) \right] \quad (2.30)$$

To confirm the calculation, the previous formula 2.9 of $D_{beam3 \min}$ is re-obtained by substituting the value $\Delta\theta_x$ with zero, as follows:

$$D_{beam3 \min} = Hei \times \left[\left(\tan \left(\arctan \left(\frac{D_{beamS}}{2O_1F'_1} \right) \right) \right) + \left(\tan \left(\arctan \left(\frac{D_{beamS}}{2O_1F'_1} \right) \right) \right) \right] \quad (2.31)$$

$$= Hei \times \frac{D_{beamS}}{O_1F'_1} \quad (2.32)$$

From equation 2.30, the variation of D_{beam3} is expressed in relation to $\Delta\theta_x$, as seen in figure 2.10. Where the limits of D_{beam3} as θ_x tends to 90 degrees and 0 degrees respectively, are $+\infty$ and the minimum spot size is achieved for $\theta_x = \theta_{x0}$.

$$\lim_{\theta_x \rightarrow 90^-} D_{beam3} = +\infty \quad (2.33)$$

$$\lim_{\theta_x \rightarrow 0^+} D_{beam3} = +\infty \quad (2.34)$$

$$D_{beam3}(\theta_x = \theta_{x0}) = D_{beam3 \min} \quad (2.35)$$

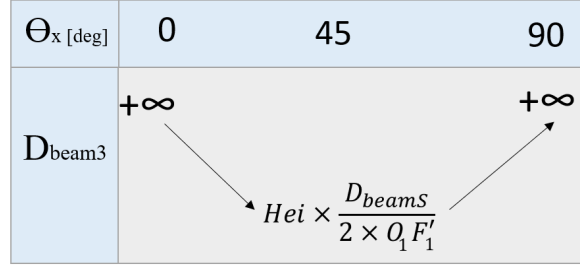


Figure 2.10: Evolution of the value D_{beam3} compared to θ_x

The spot's dimension is chosen according to the corner cube reflector's dimension and to the chosen PSD. A further study is presented in paragraph 3.3 of chapter 3.

2.3.2 Surface coverage

In the real case, where we consider the steering device has an angular rotation range, where $\Delta\theta_x$ is limited between two constant values:

$$-\Delta\theta_{xmin} < \Delta\theta_x < \Delta\theta_{xmax} \quad (2.36)$$

The maximum conveying surface dimension (S_{max}) that can be illuminated has the width denoted by the distance between the maximum position of point A in the positive abscissa and the maximum position of point B in the negative abscissa.

$$\overline{OB}_{min} = Hei \times \tan [2\Delta\theta_{xmin} - z] \quad (2.37)$$

$$\overline{OA}_{max} = Hei \times \tan [2\Delta\theta_{xmax} + z] \quad (2.38)$$

Thus, S_{max} is equal to:

$$S_{max} = \overline{BO}_{min} + \overline{OA}_{max} \quad (2.39)$$

$$= -Hei \times \tan [2\Delta\theta_{xmin} - z] + Hei \times \tan [2\Delta\theta_{xmax} + z] \quad (2.40)$$

Moreover, if we introduce the constant $\Delta\theta_{xL}$ as the maximum rotational angle

realized by the steering device, $\Delta\theta_{xmin}$ and $\Delta\theta_{xmax}$ can be re-written as:

$$\Delta\theta_{xmin} = -\Delta\theta_{xL} \quad (2.41)$$

$$\Delta\theta_{xmax} = +\Delta\theta_{xL} \quad (2.42)$$

As a conclusion, S_{max} has the final equation:

$$S_{max} = 2Hei \times \tan [2\Delta\theta_{xL} + z] \quad (2.43)$$

Where the factor 2 is explained by the fact that the scanning is symmetric.

2.3.3 Sensitivity of the spot position to the angular variation of the mirror

System sensibility is an important parameter since it allows to observe the variation of the spot position of beam 3 for each respective variation of the steering device. The spot position is denoted by Ox where x is the center of the beam3 spot and is equal to:

$$\begin{aligned} Ox &= \frac{\overline{OB} + \overline{OA}}{2} \\ &= \frac{Hei \times \tan [2\Delta\theta_x - z] + Hei \times \tan [2\Delta\theta_x + z]}{2} \end{aligned} \quad (2.44)$$

Thus, by deriving the above equation with respect to $\Delta\theta_x$ we obtain the sensitivity formula:

$$Sensitivity = \frac{dOx}{d\Delta\theta_x} \quad (2.45)$$

$$= \frac{OH}{2} [2(1 + \tan^2(2\theta_x - z)) + 2(1 + \tan^2(2\theta_x + z))] \quad (2.46)$$

$$= Hei \times [2 \tan^2(2\theta_x - z) + \tan^2(2\theta_x + z)] \quad (2.47)$$

2.4 Scanning phase

The steering device is the main element used to perform the scan of the surface. A mobile mirror attached to an electric motor or a galvanometer driver can be used to steer the beam number 2 coming from the laser source, towards the conveying surface. There are two ways to obtain 2D scanning. The first method is by using one mirror that rotates about 2 axes. The second method consists of

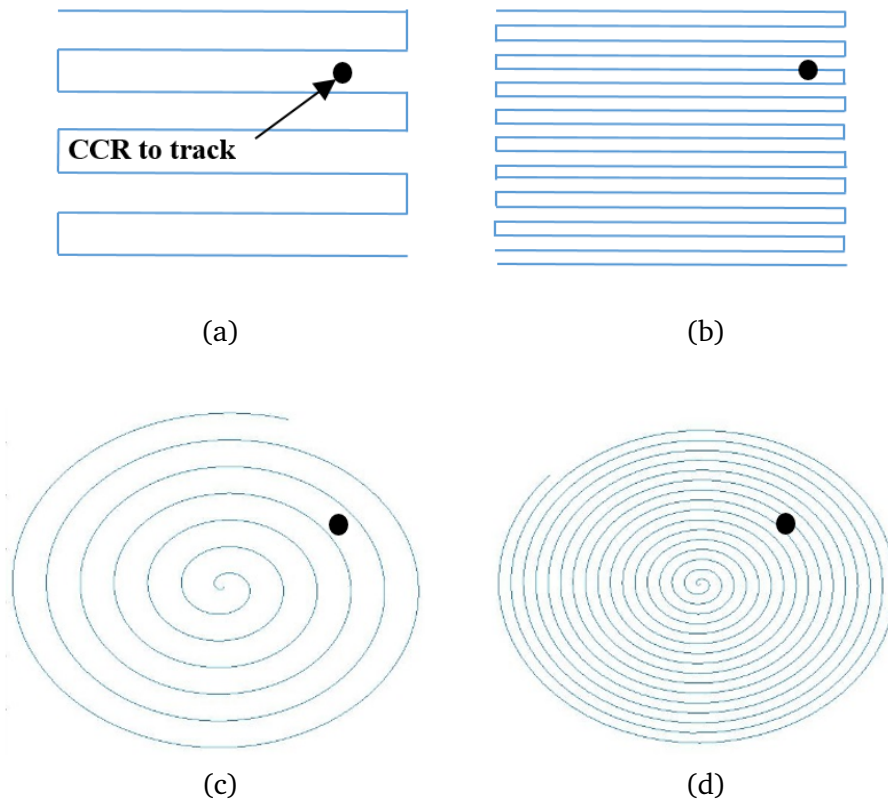


Figure 2.11: Scanning pattern compared to the size of the CCR

using two mirrors placed close to each other on orthogonal axes. Each mirror is controlled separately, so that the 2D scanning is performed by combining the two movements of these two mirrors. A Micro mirror driven by a Microelectromechanical system (MEMS) is another efficient approach to scan the surface with low power consumption and high operating speed. The MEMS micro mirror can be rotated based on different actuation principles such as electrostatic, electromagnetic, piezoelectric or thermal mechanisms [Holm 14]. By rotating the mirror in a certain manner, the surface can be scanned with different geometric patterns of which we can mention traditional raster spiral scanning, (fig 2.11). Moreover, The thickness of the scanning line is equal to the diameter of the beam spot arriving at the conveying surface. The choice of scanning pattern depends on the geometric form of the surface that can take any random configuration. The scanning criterion is that the chosen geometric pattern must cover the entire dimension. In addition, the scanning pitch must be smaller than the diameter of the corner cube reflector so that the laser scanner could pass over it at least once after one complete surface scanning, as shown in Fig. 2.11 (b and d).

2.5 Photo-detector types and functionality

The position sensing detectors (PSD) can be a segmented quadrant photo-detector (QPD) or a lateral effect photodiode (LEP). Both measure the displacement of the light beam in two axes, with respect to the detector's center. The quadrant photo-detector is composed of four identical and symmetrical detecting surfaces separated by a narrow gap. The spot size which is applied to the QPD has to be smaller than the quadrant photodiode array's diameter and bigger than the non active gap. Each quadrant generates a photo-current which is proportional to the received light intensity. By comparing the generated signal between the four quadrants, the beam position can be obtained with respect to the quadrant's origin. The LEP is presented by a single photodiode having a large area. This photodiode is equipped with two similar and uniformly resistive sheets on each of its anode and cathode. Each of the mentioned sheets has two extended ohmic contacts. Each contact pair is set to be perpendicular to one another and the two pairs are oriented at opposite corners of the sheets. The current generated is then distributed among the resistive paths to reach the contacts starting from the illuminated region. The two paths have different lengths according to the distance to be crossed by the current, and thus each possesses a resistance proportional to its path. Two currents are then developed for each resistance and the position of the center of the light spot can then be calculated from measurements of these currents.

The position of the spot is calculated accordingly by the subtraction of opposite signals and dividing this result by the sum of the mentioned signals. This results in scaling the position of the spot with minimum and maximum values of -1 and +1, respectively. Upon choosing the coordinate, as seen in Fig. 2.12, the distance x and y between the center of the light spot and the center of the QPD or LEP detector has the following equations, respectively:

$$X_{QPD} = K_{QPD} \frac{(i_c + i_d) - (i_a + i_b)}{i_a + i_b + i_c + i_d} \quad (2.48)$$

$$Y_{QPD} = K_{QPD} \frac{(i_b + i_c) - (i_a + i_d)}{i_a + i_b + i_c + i_d} \quad (2.49)$$

$$X_{LEP} = K_{LEP} \frac{i_d - i_b}{i_d + i_b} \quad (2.50)$$

$$Y_{LEP} = K_{LEP} \frac{i_c - i_a}{i_c + i_a} \quad (2.51)$$

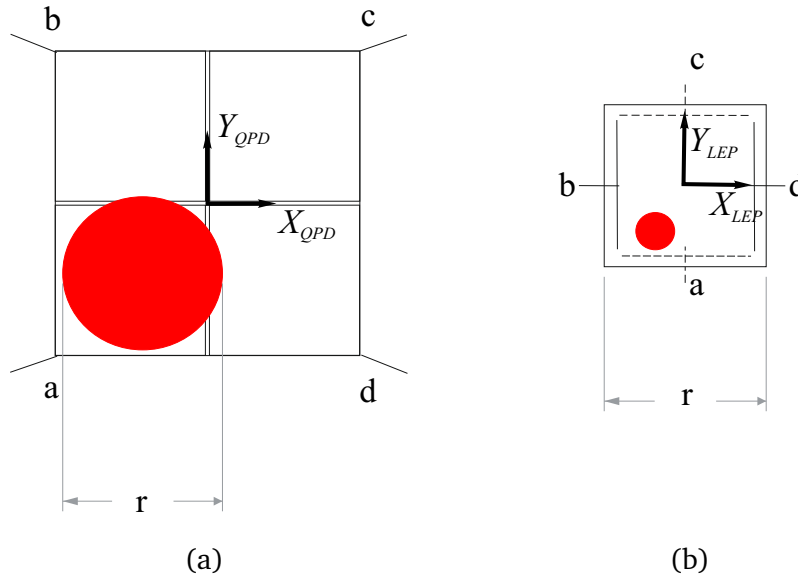


Figure 2.12: Schematic of a) a QPD and b) a LEP having an equal measurement range r

Where i_a , i_b , i_c and i_d are the average currents of the contacts a, b, c and d, and k_{LEP} and k_{QPD} providing absolute displacement values by converting the relative ones. The scale factor k_{LEP} is equal to $\frac{D_{LEP}}{2}$, where D_{LEP} is the diameter of the LEP active surface. The value of the scale factor K_{QPD} is equal to $\frac{D_{spot} \times \pi}{8}$ for a uniform circular spot close to the center of the QPD [MÄK 00]. In the figure 2.12, the value r is the measurement range of the PSD. In fact, for a spot initially centered on the active surface of the PSD, the latter can detect the spot displacement only if it moves by $\pm \frac{r}{2}$.

For the LEP, the range of measurement r is equal to the size of its active surface. In fact, the signals yield in the position of the center of the light spot with respect to the photo-detector's center regardless of the size of the light spot. The LEP detector faces a major; issue with the nonlinearity problem. The relation between the estimated position and the real position becomes nonlinear as the spot gets farther from the center of the PSD and tends to be linear as it gets closer to the center.

Figure 2.13, compares the measurement range between two different spot sizes received over the QPD's active surface. The graph in this figure represents the variation of the value x with respect to the spot position (X_{QPD}) moving over the horizontal axis. As mentioned above x is a normalized value that varies between -1 and 1, the intermediate values are described in a function of a straight line having a defined slope, for X_{QPD} values between $-\frac{r}{2}$ to $+\frac{r}{2}$. As the value of r increases, the steepness of slope, as shown in figure 2.13 (a), decreases to give a slope of

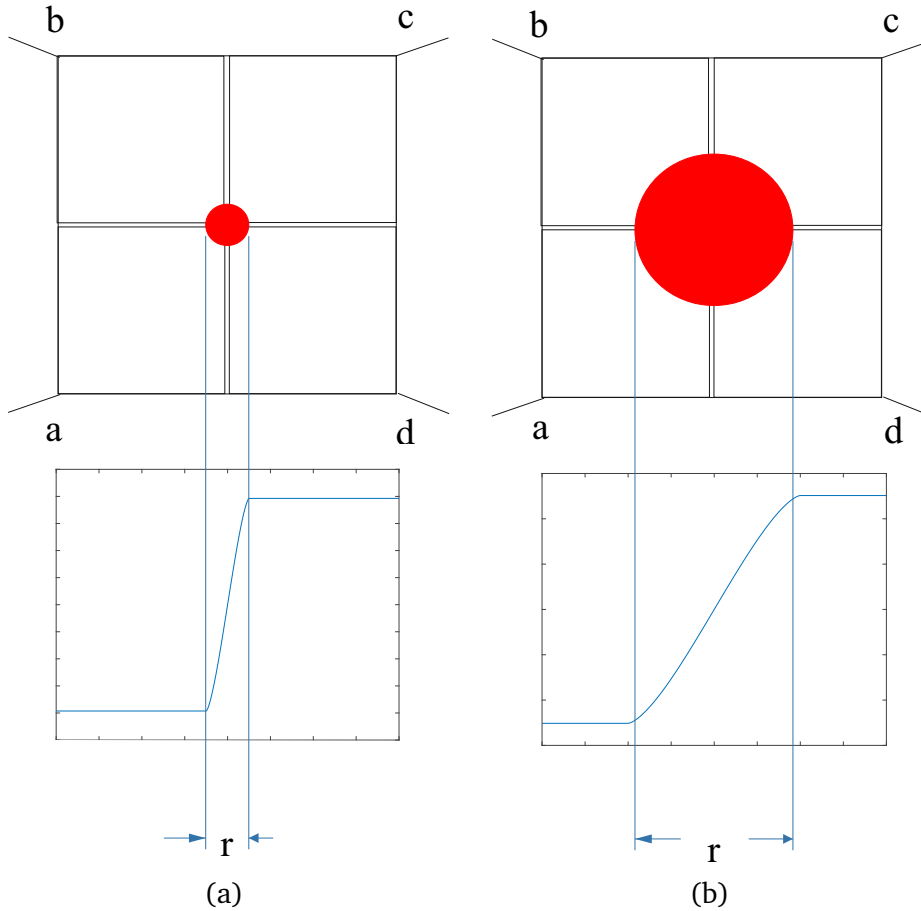


Figure 2.13: Range measurement of the QPD with respect to two different spot sizes

reduced steepness as in figure 2.13 (b). Figure 2.13 (b) gives more informations of the spot displacement over the QPD's active surface compared to the case of figure 2.13 (a). For X_{QPD} equal to +1 and -1, the QPD cannot detect the spot's movement. For example, the position 1, 2 and 3 of the spot in figure 2.14 gives the same value of $X_{QPD} = -1$. Same analysis is obtained for the variation of Y_{QPD} value with respect to the vertical displacement of the spot. Thus, the larger the spot size, the larger measuring range is achieved. Unfortunately, as the spot size increases, the position resolution decreases as well. Finally, the optimal solution is to scan the QPD surface with a spot diameter equal to the radius of THE QPD.

2.6 Conclusion

In this chapter, we have proposed an original optical method to localize and track a target moving in a 2D plane. The working principle of each element used for localization and tracking has been described in detail: the steering device, CCR, beam splitter and PSD. Furthermore, the architecture and system model were presented to explain the localization phase and the functioning principles of tracking.

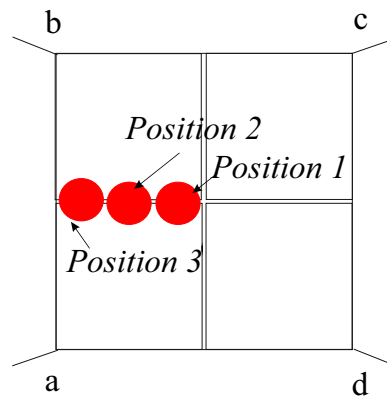


Figure 2.14: Three different positions of the spot giving same value of X_{QPD}

In addition, from the mathematical model, the relation was established between the value of spot diameter received over the conveying surface with respect to the rotation angles of the steering device (θ_x, θ_y). The surface coverage was also extracted based on the maximum orientation angles of the steering device. Next chapter is an application and validation of the proposed method presented in this chapter, in order to localize a miniaturized target called micro-conveyor moving in a relatively large surface.

Chapter 3

Validation of a closed loop tracking of a mobile micro-conveyor

3.1 Introduction

This chapter validates and affirms the technique of localization and tracking, presented in the previous chapter, in the context of a micro-factory. One of the most crucial micro-factory objectives is micro-conveying. In this case, the micro-conveyor should transport mechanical parts from one point to another in the purpose of realizing any kind of transport needing task (micro-assembly, pick and place, packaging, etc ...) [Zhak 17]. A supervision system is mandatory, first, to verify that the micro-robot hasn't lost its trajectory for any reason such as friction, actuation mal-functioning, external factors, collision with another micro-conveyor. More importantly, the system monitors and ensures that the robots have reached with high precision their final position. This chapter focuses on tracking the micro-conveyor, moving freely over the surface, under closed loop control with sensor feedback.

3.2 Micro-conveying Actuation Principles

In the context of the Factory of Future, the development of micro-factories has gained significant importance, particularly when it comes to handling micro-parts that require a miniaturized production line adapted to their size. The concept of micro-factory was introduced in 1990 by Japanese researchers at the Mechanical Engineering Laboratory (MEL), [Tana 01]. The main fundamentals of the micro-factory are to optimize the consumption of resources, space, energy and also time saving. Smart surfaces are developed to be used to convey these micro-parts between different positions on the production or assembly line. The main advantage of a smart surface is that it transports or manipulates fragile and miniaturized

parts, placed over micro-conveyors, without damaging or braking them. The smart surface is composed of a set of identical micro-actuators working together, usually distributed in a 2D matrix layout. A micro-actuator transforms energy, such as electrical, thermal, magnetic., into controlled motion of the micro-conveyor [Pole 18]. Our system of interest is composed of several micro-conveyors moving freely over a smart surface. The goal of our proposed remote optical method is to supervise and control the motion of the micro-conveyors by locating and tracking each of them. Using real-time feedback from the optical sensor, the path of the micro-conveyor can be controlled to ensure that it reaches its correct station position with high accuracy. In addition, collisions between micro-conveyors can be eliminated and resolved by controlling their speed or modifying their trajectory according to tasks priority. In reality, the possibility that one of the micro-actuators composing the intelligent surface may be damaged is inevitable. Thus, by locating the micro-conveyor and by knowing that it is approaching a defective area, the micro-conveyor can deviate to prevent its being locked by the dysfunctional micro-actuator. Over the years, different micro-actuation systems have been developed of which we mention:

- The contactless conveyor systems based on an aerodynamic traction principle [Zhu 15], [Fuku 06]. The device levitates and moves flat objects like silicon wafer or glass sheets without any contact, to the desired location using controlled airflow or fluid injection. Chen et al. developed a smart surface of $228 \times 110 \text{ mm}^2$ to convey a flat object using controlled airflow in the gap between the object and surface [Chen 18]. The surface is composed of an array of 16×8 actuating cells, each having a square surface shape of 100 mm^2 . Each cell has an inlet and outlet port connected to positive and negative pressure, respectively. Through the air pressure difference, the air-conveyor can be transported over the surface. The conveying is stable for objects having a diameter greater than at least four cells. In [Zhu 15], the conveyance of two different objects with different masses was tested within a horizontal step motion of 100 mm. The first object having a mass of approximately 10 g and the other of 16 g resulted in static errors of 0.45 mm and 0.35 mm, respectively.
- Electrostatic based systems, where electrostatic induction motors are used in order to convey dielectric objects [Edo 99]. In [Moda 10], an electrostatic induction motor technology is adopted to convey a dielectric slider sheet. The surface is composed of parallel identical electrodes fed by three phase AC voltages. Thus, running charges waves are generated on the dielectric

sheet and the electrodes. In an asynchronous phase, an electrostatic force moves the slider sheet along the surface. The surface has a dimension of $265 \text{ mm} \times 285 \text{ mm}$ with a 1 mm electrode pitch. The authors validated their conveying systems by transporting two paper sheets each having an area of $10\,000 \text{ mm}^2$ but with different masses of 0.655 g and 0.7355 g, [Moda 10].

- In electromagnetic based systems, the micro-conveyor motion is ensured by a Lorentz force generated in a magnetic environment and controlled by injected currents in coils [Khan 17]. In [Shi 18b], a prototype of a digital electromagnetic conveying surface composed of 5×5 actuator array of cells with an area of $50 \text{ mm} \times 50 \text{ mm}$ is presented. Each cell is composed of 4 fixed permanent magnets (PM), one mobile PM placed in a silicon square cavity and 2 coils underneath the mobile PM used for the x and y motions, respectively. The mobile PM can move to four discrete positions determined by the attraction of the fixed PMs. In [Shi 18b], the conveying principles were validated by placing a glass sheet of $100 \text{ }\mu\text{m}$ thickness covering the 25 actuators. The conveying system was able to perform a maximum stroke of $115 \pm 21 \text{ }\mu\text{m}$, where all the actuators worked together. By increasing the injected current amplitude from 2.5 A to 7 A, the maximum stroke was decreased to $60 \pm 5 \text{ }\mu\text{m}$.
- (SMA) actuators are based on the property of a material that changes in shape when heated above a transition temperature, in order to create motion. Once the material is cooled, it recovers and returns to its previous physical shape, if it is a 'two-ways' form. This material is an alloy between metals such as nickel-titanium (NiTi or Nitinol) or Copper Zinc Aluminum (CuZnAl). In order to reach the transition temperature, the SMA can be internally heated by injecting currents or by exposing them to an external heat source. Wireless bistable micro-actuators composed of four active SMA were proposed in [Shi 18a]. Focusing a light beam over one of the SMA leads to its deformation which pushes and moves the bistable beam. A stroke of $274 \pm 11 \text{ }\mu\text{m}$ was achieved. By placing multiple actuators in an array surface the displacement of a micro-conveyor can be realized.

Our proposed localization and tracking technique is independent on the choice of the conveying system, since it is remote and does not require adding a heavy elements on the conveyor's surface. A lightweight corner cube reflector (CCR) or a retro reflected tape is the only element added onto the micro-conveyor's surface,

serving to provide a passive feedback, ensured by a simple reflection of the incident light, in order to obtain its position over the conveying surface. Unlike an active receiver, which is based on the retransmission of information using emitter/receiver optical components, this method is described in chapter 5 for another application approach.

The following section characterizes the architecture and the mode of employment for localization and tracking of a micro-conveyor using a retro reflective corner cube.

3.3 Application of the optical system modeling

As part of this work, we have adopted the smart surface based on electromagnetic principles, developed at the Roberval laboratory, FRE UTC-CNRS 2012, in order to test our developed optical sensor, [Bosc 16]. The conveyance is based on the electromagnetic (EM) actuation principle. More details on surface functionality are provided in section 4.3. Among possible steering devices, we have chosen to scan the surface with a 2D electrostatic MEMS mirror to benefit from its low power consumption, its high operating speed, its high accuracy, and its small chip size. A quadrant photodiode (QPD) was selected to receive the reflected beam coming from the CCR, placed on the micro-conveyor. Thus, the range measurement depends on the radius of the beam received on the QPD's plane. Indeed, the recommended beam spot diameter is equal to the radius of the QPD's active surface (R_{QPD}), to give the best compromise between the measurement range and resolution as explained in section 2.5 of chapter 2.

As mentioned before, the principle of tracking consists in the MEMS mirror continuing to follow the target displacement, by directing the light towards the center of CCR. This is ensured, in a closed loop control system with the QPD generated signal, by maintaining the position of the received beam at the center of the QPD's active surface. The beam reflected from the MEMS mirror to the conveying surface is noted as beam 3, and the beam received on QPD is noted as beam 6. The difference between the velocity of the target, as it moves, relative to the speed of the tracking system, defines the distance at which the beam 3 and 6 will be shifted from the center of the CCR and the QPD, respectively. The faster the micro-conveyor moves, compared to the system tracking rapidity, the more the beams will be shifted away from their original centered position. For a velocity of the micro-conveyor greater than a threshold value, noted V_{max} , the control system fails to track the micro-conveyor, where V_{max} is written as follows:

$$V_{max} = \frac{d_{max}}{t_R} \quad (3.1)$$

and t_R is the response time of the tracking system. The response time is the interaction time between the QPD and the MEMS mirror, each having a defined time responsivity. d_{max} is the distance traveled by the CCR from its initial centered position to the edge of the light spot of beam 3, as seen in figure 3.1. Moreover, d_{max} is written as function of D_{beam3} as follows:

$$d_{max} = \frac{D_{beam3} - D_{CCR}}{2} \quad (3.2)$$

As a conclusion, the threshold value (V_{max}) of the target's velocity increases by

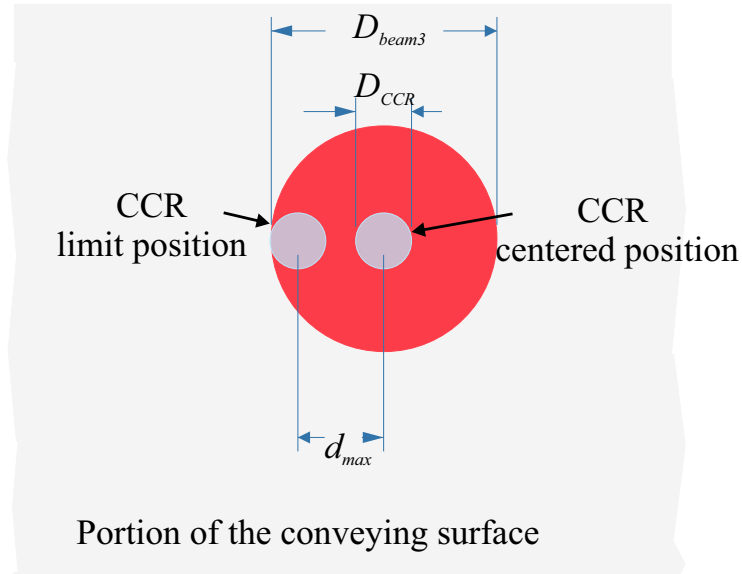


Figure 3.1: Position of the CCR inside the optical spot

reducing the t_R value and by increasing the surface of the spot illuminating the conveying surface (i.e D_{beam3}). t_R is enhanced by adopting a MEMS mirror and a QPD having high response time and by implementing a proportional regulator, or PID. On the other hand, with an increase in the D_{beam3} value, a bigger CCR is required in order to increase the intensity of the reflected light beam, i.e, increase the signal to noise ratio (SNR). However, a limitation is imposed on the CCR volume, because a bigger CCR leads to more weight onto the micro-conveyor.

Figure 3.2 is a 2D representation of Gauss's approximation of our optical system during the tracking phase, where the CCR is centered with respect to beam 3 and beam 6 is centered with respect to the QPD's active surface.

In Fig 3.2, the ray's trajectory starts with the incident beam coming from the laser source (beam number 1 and 2). The incident beam is marked with a dotted red line and the reflected beam by the CCR is marked with a full red line. As a collimated laser source is employed, the incident light converges at the focal point

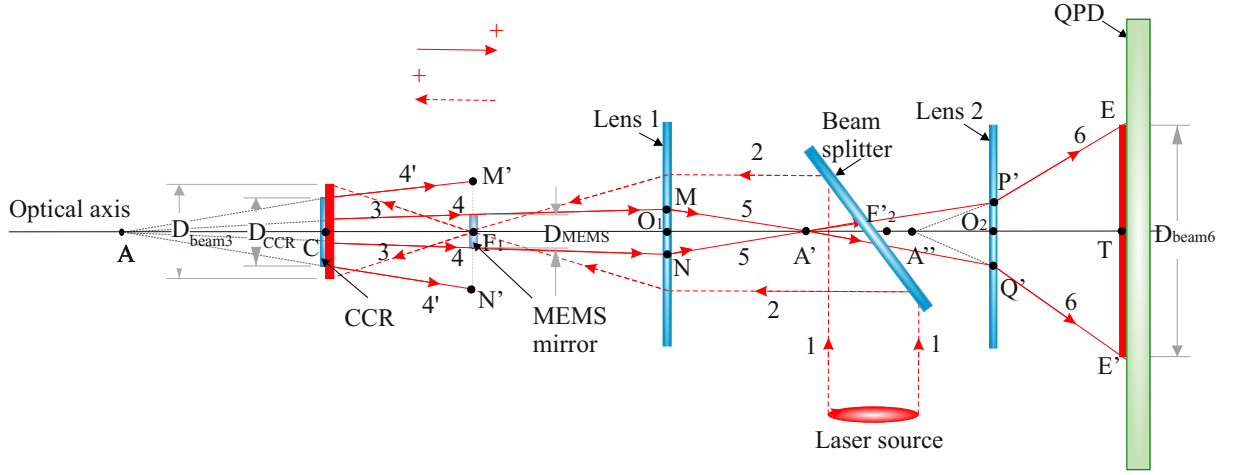


Figure 3.2: Optical presentation of the system

F_1' , of the first lens, where the MEMS is positioned. In fact, the MEMS is at F_1' , when the light is coming from the laser source, and it is at point F_1' , when the light comes from the CCR. Then, the MEMS mirror reflects the ray towards the conveying surface (beam number 3). For simplicity, the optical path of beam3 is presented on same axis. Upon reaching the corner cube reflector, the beam is reflected and heads back towards the convergent lens 1 to converge at point A' which is the net image of the point A (step 4 and 5). In fact, the point A is the virtual intersection point of the extensions of the two reflected rays coming from the corner cube reflector's extremities. Each reflection is parallel to the incident dotted beam and shifted by a distance equal to the corner cube reflector's diameter (D_{CCR}). In this figure, the CCR is presented at the position point C .

The MEMS mirror positioned on the focal plane F_1 , receives the reflected light beam with a diameter $M'N'$ equal to the double of D_{CCR} . This value is proven by applying Thales' Theorem in the $AM'N'$ triangle:

$$\frac{AC}{AF_1} = \frac{D_{CCR}}{M'N'} = \frac{1}{2} \quad (3.3)$$

The distance AF_1 is equal to the double of that of AC , where C is the center of AF_1 , thanks to Snell-Descartes first law. In this application, the corner cube reflector has a relatively larger dimension than that of the MEMS mirror (D_{MEMS}). Thus, the latter acts as a diaphragm with respect to the reflected beam $M'N'$. The amount of light received at lens 1 is then reduced to a spot having a diameter equal to MN . Depending on the configuration of our system, the second lens placed in front of the QPD should be divergent, in order to obtain a value of D_{beam6} equal to R_{QPD} at a such short distance between the second lens and the QPD's plane.

Thus, A' is considered as the object with respect to the second lens 2. The light

diverges from the point A'' , which is the virtual image of A' , towards the plane of the QPD giving a spot diameter equal to EE' . The rest of this section focuses on calculating the value EE' with respect to the system's parameters:

- focal lengths of lens 1 and lens 2 (which are the values of O_1F_1 and O_2F_2 , respectively),
- distance between the two lenses O_2O_1 ,
- distance between the corner cube reflector and focal point of lens 1 ($\overline{CF_1}$)
- distance between lens 2 and the QPD (O_2T).
- EE' equal to R_{QPD} .

Applying Thales' Theorem in the $A''EE'$ triangle allows EE' to be expressed in terms of $A''T$, O_2A'' , and $P'Q'$ as follows:

$$EE' = \frac{A''T}{A''O_2} \times P'Q' \quad (3.4)$$

Where $A''T$ is written as:

$$\overline{A''T} = \overline{A''O_2} + \overline{O_2T} \quad (3.5)$$

O_2A'' is the distance between the image of A' and the center of lens 2 calculated by applying the Descartes' conjugate equation:

$$\overline{O_2A''} = \frac{\overline{O_2F_2'} \times \overline{O_2A'}}{\overline{O_2A'} + \overline{O_2F_2'}} \quad (3.6)$$

To reduce the number of parameters, the object distance O_2A' is replaced by the sum of O_2O_1 and O_1A' .

$$\overline{O_2A'} = \overline{O_2O_1} + \overline{O_1A'} \quad (3.7)$$

Where O_1A' is the distance between the image of A and the center of lens 1, obtained from the Descartes' conjugate equation:

$$\overline{O_1A'} = \frac{\overline{O_1F_1'} \times \overline{O_1A}}{\overline{O_1A} + \overline{O_1F_1'}} \quad (3.8)$$

As for $P'Q'$, applying Thales' Theorem in triangle $A'PQ$ and triangle $A'M'N'$ gives $P'Q'$ to be equal to:

$$P'Q' = \frac{A'O_2}{A'O_1} \times MN \quad (3.9)$$

Where MN is obtained, from Thales' theorem in triangle $A'MN$, giving:

$$MN = \frac{AO_1}{F_1A} \times D_{MEMS} = \frac{O_1F_1 + 2CF_1}{CF_1} \times D_{MEMS} \quad (3.10)$$

Finally, each parameter of EE' is determined as a function of geometrical distances.

3.4 Control unit

After the dimensional study and the installation of system's components such as lenses and optoelectronic devices, the next step is to control the scanning of the MEMS mirror based on the optical sensor's feedback. A C code and a LabVIEW interface have been developed to complete this task, in order to locate and track the micro-conveyor. The C code is integrated in a PIC32 microcontroller [MICR 16] to control the orientation of the MEMS mirror. The LabVIEW code is implemented to facilitate the application of the user interface, in order to monitor the QPD signals and to send the desired control signals to the micro-controller, corresponding to the new orientation of the MEMS mirror. LabVIEW is the abbreviation for Laboratory Virtual Instrument Engineering Workbench. It is used for: ii) data acquisition (by reading the QPD signals), ii) instrument control (by controlling the command signals sent to the MEMS mirror) and iii) implementation of automatic blocks (by correcting the orientation of the MEMS mirror based on the tracking algorithm). Figure 3.3 illustrates the control chain composed of the elements used in this work, such as, QPD sensor from 'first sensor' [Quad], USB 6009 of the 'national instruments', PIC32 microcontroller, MEMS driver, called Pico-amp, and MEMS mirror from 'mirrorcle Inc', [Inc 16]. The USB National Instrument Data Acquisition De-

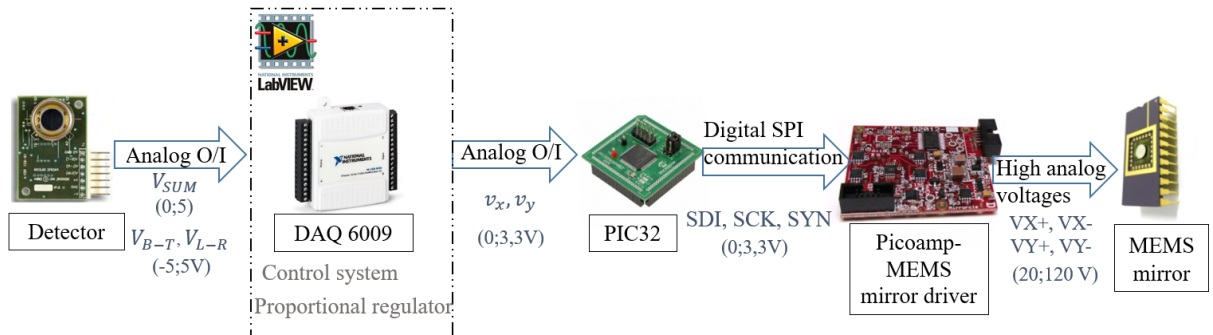


Figure 3.3: Control chain of the localization and tracking system

vice (NI DAQ 6009) is equipped with analog input and output pins handled using the labVIEW code. The analog inputs are assigned to receive the signals generated by the QPD and the output pins are assigned to the generated analog output sig-

nals sent to the PIC32. The latter transmits the output signals to the MEMS driver via a peripheral serial interface (SPI). More details on the functionality of each component are presented in the rest of this section.

3.4.1 QPD signals

The QPD (QP50-6-TO8) purchased from 'First Sensor' corporation generates the following output voltages [Quad]:

$$V_{SUM} = [V_I + V_{II} + V_{III} + V_{IV}] \quad (3.11)$$

$$V_{B-T} = [(V_{III} + V_{IV}) - (V_I + V_{II})] \quad (3.12)$$

$$V_{L-R} = [(V_{II} + V_{III}) - (V_I + V_{IV})] \quad (3.13)$$

where V_i , ($i = I, II, III$ or IV) is the voltage generated by the i_{th} quadrant, which is proportional to the received light intensity. V_{SUM} is the value corresponding to the summation of these four voltages. It indicates whether the QPD is exposed to the light beam or not. V_{L-R} is equal to the subtraction of the output voltages of the left and right quadrants. Similarly, V_{B-T} is the difference between the voltages generated by the bottom quadrants from those of the upper quadrants. The position of the light beam on the active surface of the QPD (x_{QPD} and y_{QPD}) can be interpolated by analyzing these output signals.

For our application, the light beam being studied is the reflection coming from the corner cube reflector, i.e it is the beam number 6. Table 3.4 shows four different examples of the light spot positioning on the active surface of the QPD, providing the corresponding analysis of the QPD output signals and the beam position (x_{QPD} and y_{QPD}):

In case 1, the QPD is not illuminated by light beam6. V_{SUM} has a relatively low value. For the other three cases, the QPD receives beam6 and V_{SUM} increases in value. A threshold value (V_{Th}) is introduced to test the reception of the beam6. The threshold value depends on the power of the laser in use, electronic noise, and the ambient light. V_{L-R} and V_{B-T} values undergo analysis to determine the spot's position, once V_{SUM} becomes greater than V_{Th} . For case 2 ($V_{L-R} \simeq V_{B-T} \simeq 0$), this means that the spot light is near the center of the QPD, giving $X_{QPD} \simeq Y_{QPD} \simeq 0$. It is impossible to reach zero value for the mentioned parameters due to the electronic noise and due to the fact that the spot cannot have a flawless symmetric circular shape. In case 3, the reflected light spot shifts from the center to the top, V_{B-T} decreases to a negative value and the Y_{QPD} value becomes positive. The

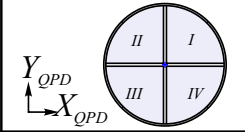
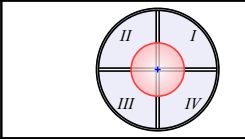
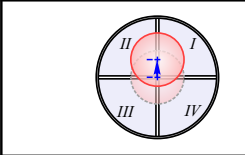
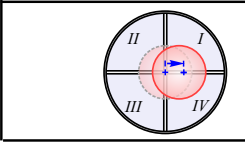
	$V_{SUM} < V_{Th}$	Case 1: $V_{B-T} \approx V_{L-R} \approx 0$ No information on values of X_{QPD} and Y_{QPD}
	$V_{SUM} > V_{Th}$	Case 2: $V_{B-T} \approx V_{L-R} \approx 0$ $X_{QPD} \approx Y_{QPD} \approx 0$ The light beam is near the center of the QPD
		Case 3: $V_{L-R} \approx 0; V_{B-T} < 0$ $X_{QPD} \approx 0; Y_{QPD} > 0$ The light beam shifted to the top
		Case 4: $V_{L-R} < 0; V_{B-T} = 0$ $X_{QPD} > 0; Y_{QPD} = 0$ The light beam shifted to the right

Figure 3.4: Quadrant photodiode with different spot positions

V_{L-R} value as well as the X_{QPD} remains near to zero. For a light spot at the middle right, as seen in case 4, V_{L-R} becomes negative and X_{QPD} becomes positive. V_{B-T} as well as the y_{QPD} remains near to zero.

3.4.2 Localization and tracking algorithm

Figure 3.5 illustrates the block diagram of the tracking algorithm. At first, the control system commands the MEMS mirror to operate in the scanning phase, making it rotate as it seeks the micro-conveyor's position. In parallel, the NI-DAQ continues to read the QPD output signals. V_{SUM} is compared, via LabVIEW, to V_{Th} . If V_{SUM} remains less than the threshold value, the system remains operating in the scanning phase. Once V_{SUM} becomes greater than V_{Th} , the system switches into tracking mode where the MEMS mirror rotates to remain in the same line of sight with the micro-conveyor having V_{L-R} and V_{B-T} values that are near to zero.

3.4.3 MEMS mirror control

The micro-mirror developed at Mirrorcle Technologies Inc., is driven based on the bias-differential quad-channel (BDQ) principle [Mila 09]. Moreover, it rotates in two orthogonal axis, by applying 4 analog voltages (V_{X+} , V_{X-} , V_{Y+} and V_{Y-}) to its electrostatic comb-drive actuators based on the following formulas:

$$V_{X\pm} = V_{bias} \pm \frac{V_{diffx}}{2} \quad (3.14)$$

$$V_{Y\pm} = V_{bias} \mp \frac{V_{diffy}}{2} \quad (3.15)$$

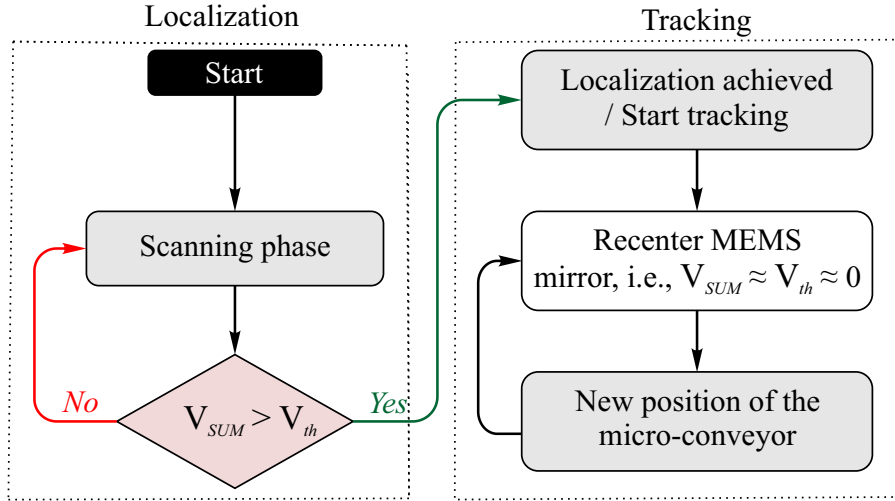


Figure 3.5: Block diagram of the localization and tracking algorithm

where V_{bias} is the voltage value corresponding to the rest position of the mirror, i.e., $\theta_x = \theta_y = 0^\circ$. Each mirror has a specific V_{bias} declared in its own datasheet. The differential voltages of x - and y -axes (V_{diffx} and V_{diffy}) are proportional to θ_x and θ_y , respectively:

$$\theta_x = K_x \times V_{diffx} \quad (3.16)$$

$$\theta_y = K_y \times V_{diffy} \quad (3.17)$$

where k_x, k_y are the linearity factors that differ from one mirror to another.

In this work, the MEMS mirror of $1700 \mu\text{m}$ diameter, selected to perform the scanning task had the following features:

- Maximum angle-X axis of 5.21 degrees
- Maximum angle-Y axis of 5.33 degrees
- Maximum coupled angle of 6.72 degrees
- Bias voltage of 70 V

A calibration of the MEMS mirror was carried out in order to find the exact values of K_x and K_y . A graph paper was placed in front of the MEMS mirror at a known distance (D), as shown in figure 3.6 (a). The origin of the parallel plane (O') corresponds to the spot position where the MEMS mirror is in the rest position, i.e. $v_{diffx} = v_{diffy} = 0$. x', y' are the spot coordinates in this parallel plane. The calibration of the MEMS mirror in the y -axis was performed by sending

different values of V_{diffy} but with a null value of v_{diffx} . The light spot scans the x' -axis and the corresponding θ_x is calculated by applying the trigonometric formula:

$$\theta_x = \frac{\arctan(\frac{x'}{D})}{2} \quad (3.18)$$

$$\theta_y = \frac{\arctan(\frac{y'}{D})}{2} \quad (3.19)$$

The same procedure is repeated for the y-axis (equation 3.19). Figure 3.6 (b) explains the fact that when the MEMS rotates by an angle θ the reflected beam moves by an angle 2θ . In this example, the incident beam is reflected by an angle α when the MEMS mirror is in position 1, that is the rest state. Then, the MEMS rotates by an angle of θ leading to a reflection of the same incident light beam but with a reflected angle equal to $\alpha + \theta$. The angle between the first reflection and the second reflection is equal to 2θ .

Figure 3.7 a (b) illustrates the variation of θ_x (θ_y) as a function of V_{diffx} (V_{diffy}). The linear behaviors, observed for v_{diffx} and v_{diffy} , are between -100V and 100V for a $V_{bias} = 70V$. The linearity coefficients were measured to be equal to $k_x = 0.040$ and $k_y = 0.043$. From equations 3.14 and 3.15, the four applied voltages ($VX+$, $VX-$, $VY+$ and $VY-$) sent to this MEMS mirror must be between 20V and 120V.

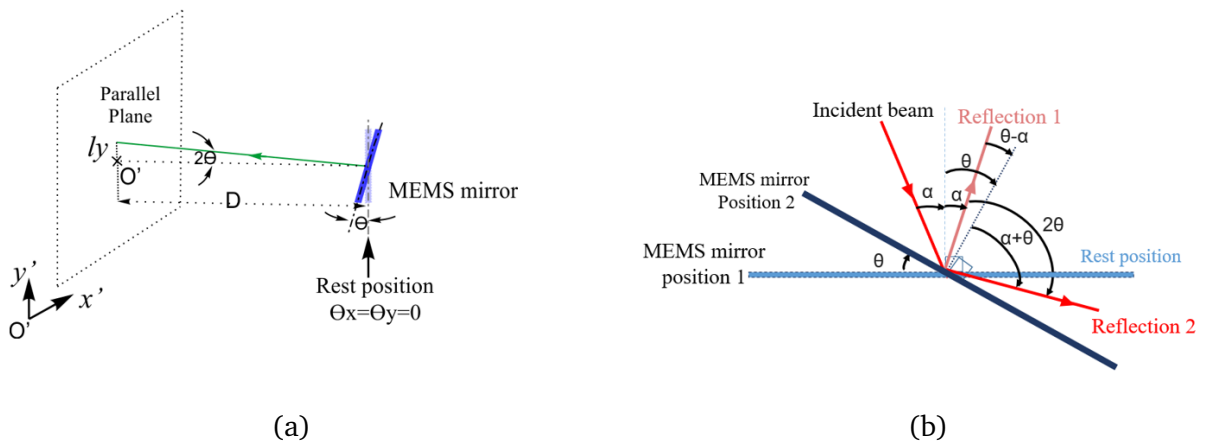


Figure 3.6: (a) Schematic description of the MEMS mirror angular variation; (b) detailed description in 2D.

By sending series of consecutive voltage pairs ($VX+$, $VX-$) and ($VY+$, $VY-$), we are able to obtain different patterns such as spiral and rectangular patterns as shown in Fig.3.8 (c and d), respectively. The variations of $VX+$ with respect to $VY+$ between 20 V and 120 V are illustrated in figures 3.8 (a and b) corresponding, respectively, to the obtained spiral and rectangular scanning patterns. The same graph is observed for the variation of $VX-$ with respect to $VY-$.

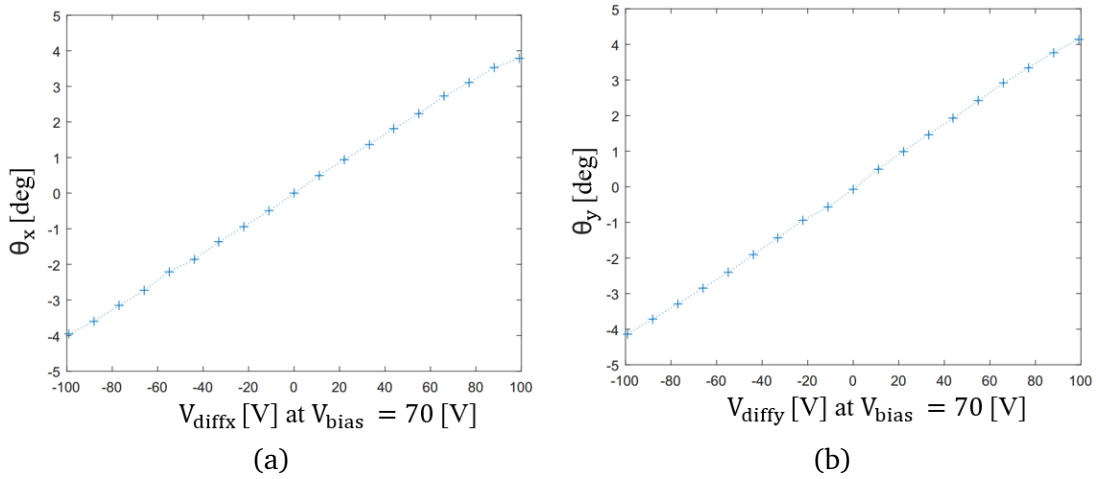


Figure 3.7: Variation of (a) θ_x as a function of V_{diffx} , (b) θ_y as a function of V_{diffy}

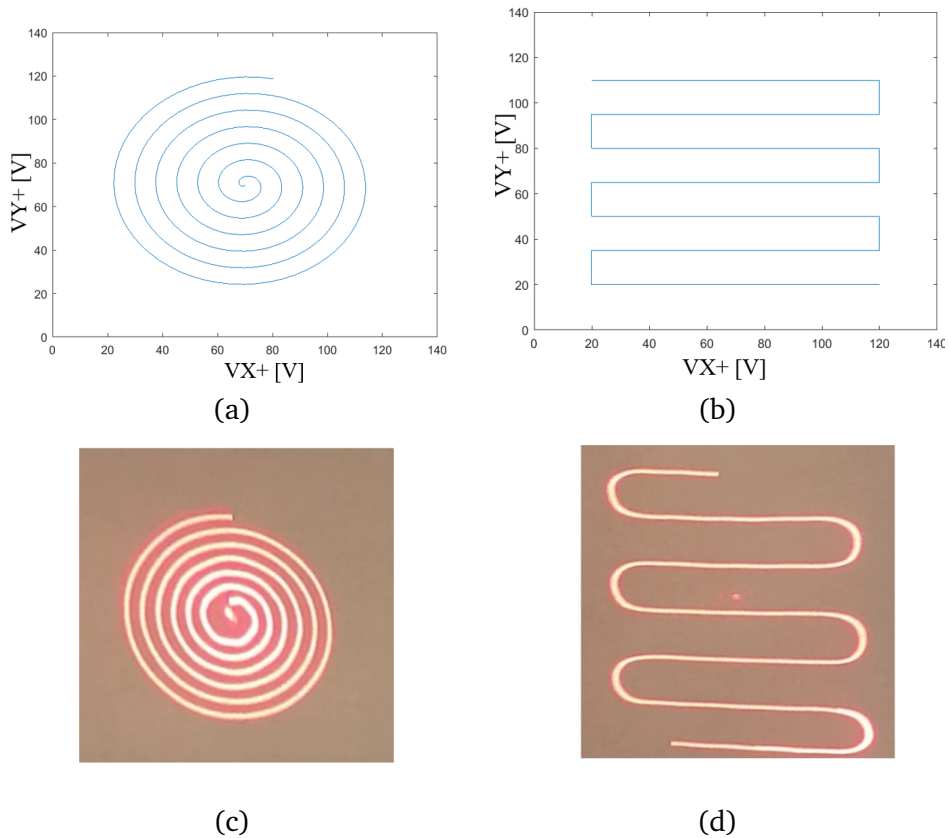


Figure 3.8: Applied voltages for $VX+$ vs $VY+$ for different scanning shapes (a) spiral (b) rectangle, with their corresponding resulting laser scanning pattern (c) and (d), respectively

A spiral pattern is chosen to cover the scanning surface for its smoothness. Such a pattern is more suited to the dynamic behavior of the micro-mirror where the high frequencies are avoided. In the spiral mode, the angular variation between different positions of the mirror is less than the angular variation in the case of rectangular scanning. The spiral pattern should cover the entire surface and possess a pitch value lower than the QPD active area dimension, in order that the laser spot could be detected.

The MEMS mirror driver is the component dedicated to deliver these four high analog voltages to the micro-mirror. There are two types of MEMS driver, the first with an analog input and the second with a digital input. Either way, the driver converts the low input voltages into two differential pairs of high output analog voltages.

The analog driver contains a bias differential quad-channel circuit receiving analog input voltages between -10 and 10 V. Hence, the range is preset and the bias voltage cannot be adjusted. As for the digital driver, chosen in this work, the four output channels are set via software, thus, the full voltage range can be used and V_{bias} and differential voltages can be set to any desired value.

A digital to analog converter (DAC), four filters and an amplifier are embedded in the driver circuit. The 16-bit DAC converts the digital input into four analog voltages to drive the micro-mirror. The four embedded filters act as low pass filters to smooth the output signals. Thus, the mirror is prevented from entering resonance mode and is protected from overshoot and ringing. The filter clock frequency ($FCLK$) is digitally controlled via software and is set to 60 times the recommended cut-off frequency indicated in the mirror datasheet. The integrated regulated DC/DC converter amplifies the low voltage input, with a range of 0 to 2.5 V, to a high output voltage of between 0 and 200 V [Inc 16]. However, as mentioned above, the operating range is between 20 and 120 V to ensure that the adopted MEMS mirror rotates in the linear zone. Next, the micro-controller is developed in such a way to communicate with the MEMS driver, in order to control the orientation of the MEMS mirror.

3.4.4 Micro-controller development environment

The MPLAB X Integrated Development Environment (IDE) software from microchip was used to download and compile our C code into the PIC32 micro-controller. It sends a sequence of input command to shift registers, via a SPI bus towards the MEMS's driver, in order to set up the four channels of the integrated DAC, see figure 3.9. The input shift register content is composed of command bits to identify its functionality (control or data register), address bits to specify the chosen channel to which the information should be sent, and 16 bits dedicated for the value

corresponding to the new mirror orientation. After enabling each of the DAC's four channels, the micro-controller is ready to send data registers. The output compare module of the micro-controller is configured into pulse width modulation, in order to generate the required FCLK signal ('clock' signal). The localization and tracking algorithm can be added to the C code, making the micro-controller works in a standalone mode. However, the signals V_{B-T} and V_{L-R} generated by the QPD, has a range of +5 V to -5 V and the micro-controller can receive only over its pins a range of 0 V to 3.3 V. For that an electronic circuit composed of two operational amplifier (Op-Amp) should be added to the system with corresponding resistors and source supply power. The first Op-Amp is used to shift the signal from [-5 V, 5 V] to [0V, 10 V] and the second to divide the range to the desired range [0 V, 3.3 V], that the micro-controller can receive. LabVIEW code is added to the control chain to avoid any additional electronic circuitry, where the USB 6009 receives signals from -10V to 10V, but mainly LabVIEW is used to provide a user interface.

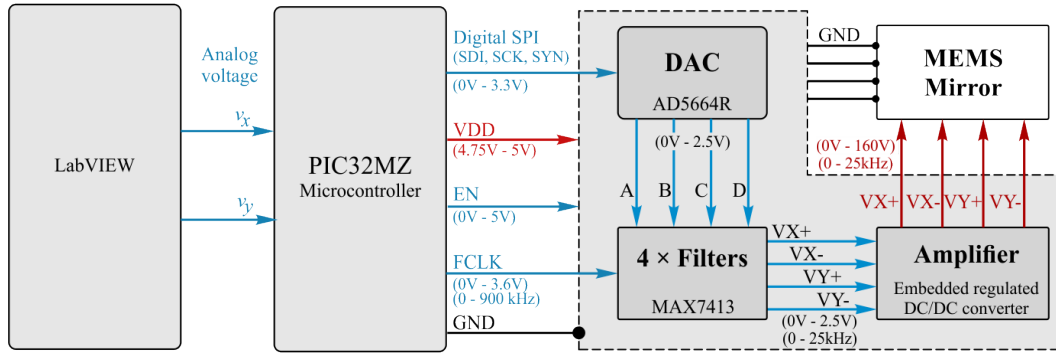


Figure 3.9: Schematic layout of the control unit of the MEMS mirror driver.

3.4.5 Labview interface

The LabVIEW interface receives the voltages V_{SUM} , V_{B-T} and V_{L-R} from the QPD and according to these values, generates two output voltages named (v_x, v_y) . The PIC32 micro-controller converts the v_x and v_y values that correspond to $VX+$ and $VY+$ values, respectively. The generation of only two output voltages is sufficient, since $VX-$ and $VY-$ can be interpolated in C code by using equations 3.14 and 3.15 as follows:

$$VX- = 2 \times V_{bias} - VX+ \quad (3.20)$$

$$VY- = 2 \times V_{bias} - VY+ \quad (3.21)$$

The LabVIEW code is composed of 4 main parts, as seen in Fig. 3.10:

- Data acquisition: V_{sum} , V_{L-R} and V_{B-T} photodiode signals are captured from

the NI DAQ module with an acquisition mode of 1 sample on demand. Three waveform graphs are used to visualize the voltages over the time.

- scanning: By pressing the send button, the system starts scanning the surface. The user can choose the scanning pattern (point to point, spiral, square scanning) by choosing the value of “case pattern”. In the point to point mode, the value of v_x and v_y can be chosen manually using the horizontal pointer slides.
- Localization: An “if/else” bloc is implemented to compare the V_{SUM} with the threshold value (V_{Th}), in order to trigger the tracking mode once V_{SUM} exceeds the V_{Th} value which is chosen experimentally. The led “4Q localized” is on when the localization occurs.
- Tracking: the values of v_x and v_y are corrected using a proportional regulator Kp. In this implementation, Kp is equal to 0.06 (chosen experimentally). The correction of v_x and v_y pauses for V_{L-R} and V_{B-T} voltages less than a tolerance (ϵ_0) equal to 10 mV. As the QPD cannot generate an exact zero voltage, the tolerance value is present and is experimentally determined. For a fixed position of the micro-conveyor and while tracking is launched, the QPD generates a non zero voltage which will be considered as the 10 mV tolerance threshold.

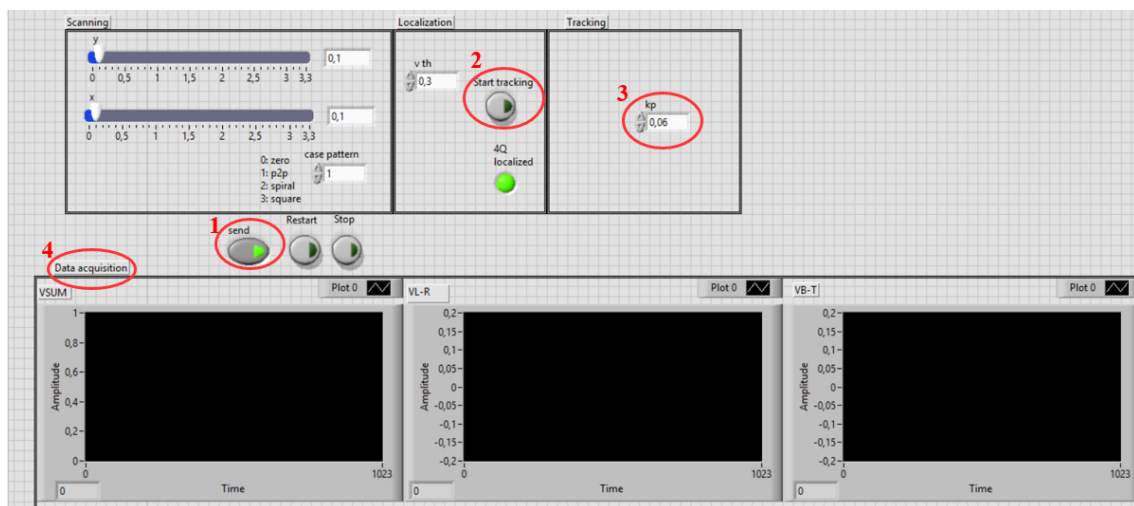


Figure 3.10: LabVIEW front-end interface

Figure 3.11 illustrates the flowchart of the entire system, including the sequential interaction between the user, LabVIEW interface, PIC32 micro-controller, Pico-amp and the MEMS mirror over the time.

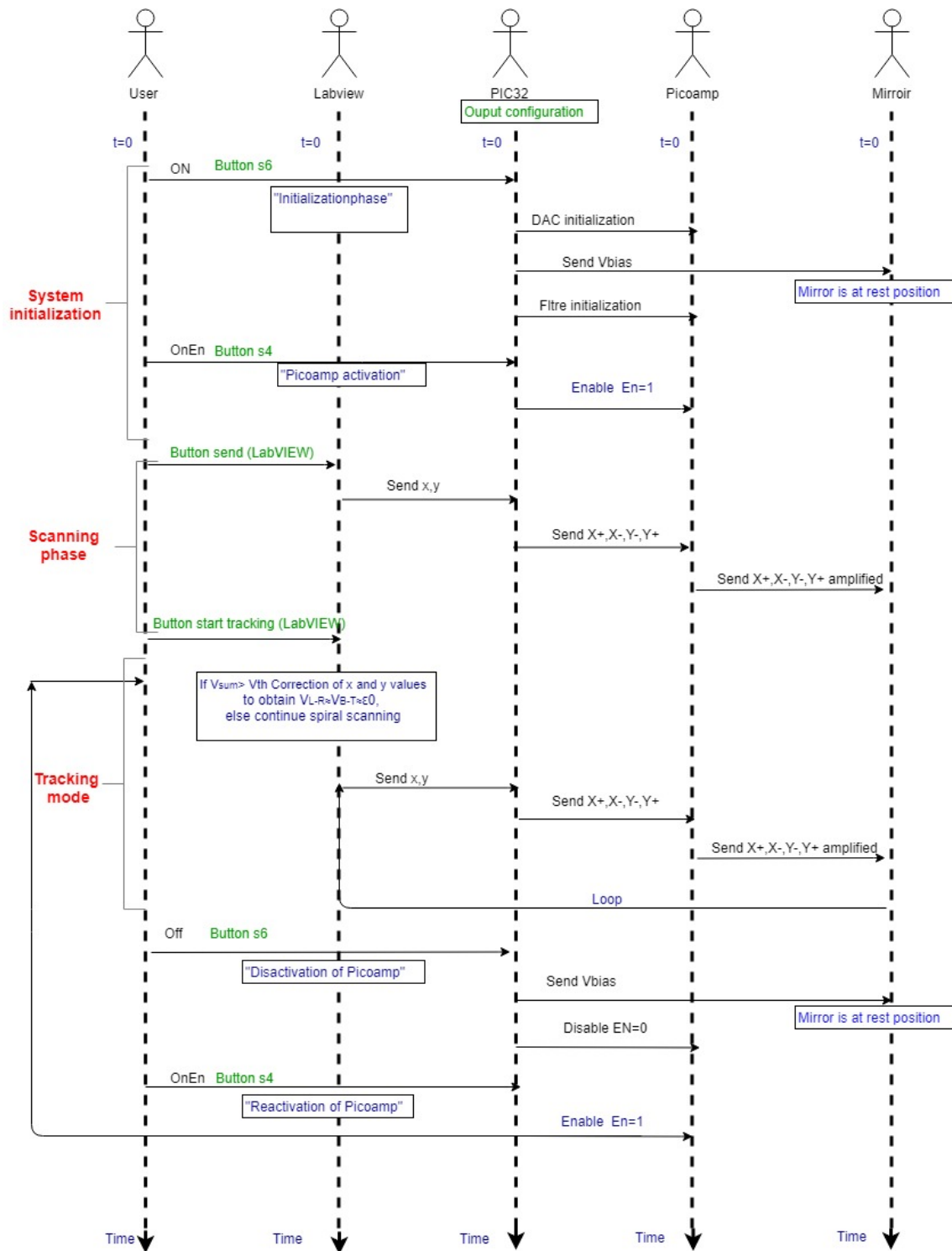


Figure 3.11: Organizational chart of the entire system

3.5 Experimental results

The goal of this experimental setup, as a first step, is to test the functionality of the scanning phase and to test the control system that localizes and tracks one micro-conveyor moving over the conveying surface. Figure 3.12 is a photograph

of the developed optical system. As mentioned before, the ray trajectory starts

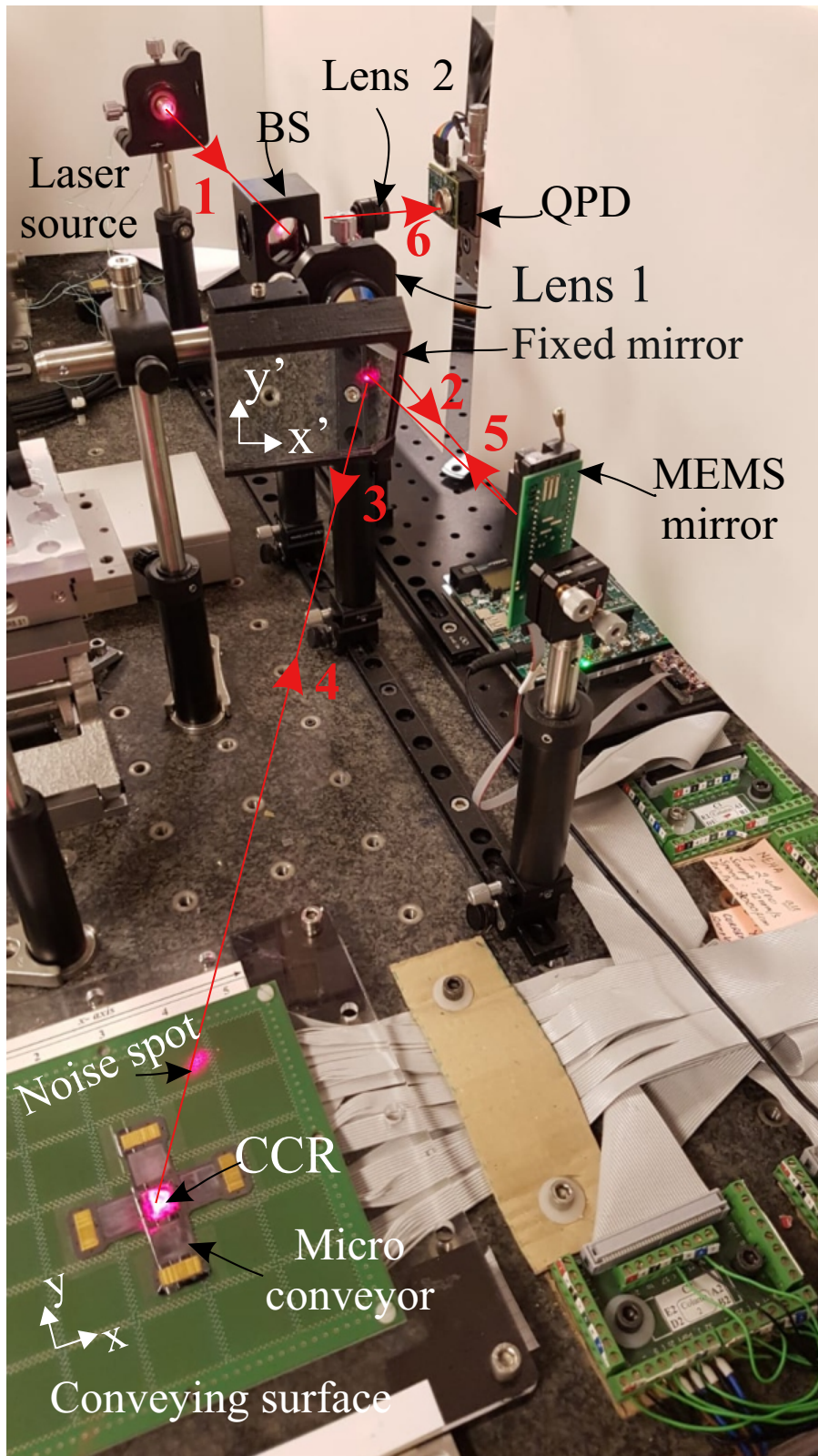


Figure 3.12: Photography of the control system

with a the light ray emitted by a collimated laser diode (beam 1) directed towards

the (50%/50%) beam splitter. The useful light is transmitted towards the MEMS mirror (beam 2) and the reflected beam is considered to be lost and blocked by a beam absorber, in order to not disturb the working environment. Next, the MEMS mirror, directs the light towards the conveying surface (beam 3). However, due to the fact that the MEMS mirror cannot be implemented on top of the conveying surface easily, a fixed mirror is used to direct the light towards the conveying plane. In this figure, the light beam reaches the CCR, which means that a reflection will occur (beam 4) to be directed towards the QPD. As seen in the figure, a second light spot is observed on the surface with a fixed position and low power intensity. It is considered as a noise spot light. In fact, there is a fixed integrated glass sheet in front of the MEMS mirror for protection purposes, which causes this noisy reflection. In order not to be disturbed by this spot, the fixed mirror is oriented in such a way to place the noise spot's position at the edge of the surface, a zone which the micro-conveyor cannot reach.

In such a configuration, there are three main factors that causes significant loss of optical power. First factor results from the beam splitter, where half of beam 1 and half of beam 5 are lost since they are not used in our system. Secondly, a portion of beam 3 is lost due to the fact that the diameter of CCR is smaller than D_{beam3} . Third, the small diameter of the MEMS, which acts as a diaphragm for beam 4, resulting in the loss of a portion of the optical power of beam 4, as seen in figure 3.2.

As a result, a powerful laser diode is mandatory for such system. In this work, we adopted the red laser diode L660P120 from thorlabs having a 120 mW output power and is driven by the TLD001 driver from thorlabs. From the initial power source value, only 0.3 mw is received on the QPD. This value is measured by an optical powermeter placed in front of the QPD. This received value is sufficient for generating a significant value of V_{SUM} during localization and tracking phase.

The dimension of the spot received over the conveying surface should be relatively larger than the diameter of CCR, in order to not lose lots of optical power. The parameters that define the D_{beam3} value are: i) the beam width of the source, ii) the MEMS mirror elevation with respect to the conveying surface, and iii) the focal length of lens 1. In fact, the laser source has a defined beam width and the MEMS mirror will be positioned at a certain elevation, suitable for experimental work. Thus, the focal length of lens 1 imposed so as to focus the light on the MEMS mirror, giving the desired beam width over the conveying surface. Lens 2 is then chosen to ensure that D_{beam6} received by QPD's active surface is equal to the radius of this surface, for a relatively short distance between the BS and the QPD.

A pre-step phase is mandatory to calibrate the QPD. The CCR is positioned at

the center of beam3 and then the QPD's position is regulated in the x and y-axes using Newport translation stages, in order center the QPD with respect to beam6.

After installing the setup and centering the position of the QPD. The system is ready to be tested.

The experiment starts by the scanning phase, where the MEMS mirror draws a spiral pattern over the conveying surface, looking for the micro-conveyor. In parallel, the control system continues to monitor the output signal generated from the QPD, to find a position where V_{SUM} is greater than V_{Th} . Once this occurs, the localization of the micro-conveyor is completed and the system switches from surface scanning to micro-conveyor tracking. Figure 3.13 illustrates the QPD output voltages as a function of time. At time $t < t'$, the system runs during the scanning phase. At time $t = t'$, the value of V_{SUM} becomes greater than the threshold value ($V_{Th} = 0.15V$, chosen experimentally), indicating that the QPD has received the light beam reflected by the corner cube reflector on the micro-conveyor. For $t > t'$, the system exits the scanning mode to start the tracking of the micro-conveyor. The values of V_{B-T} and V_{L-R} then oscillate around zero indicating that the micro-conveyor is tracking correctly.

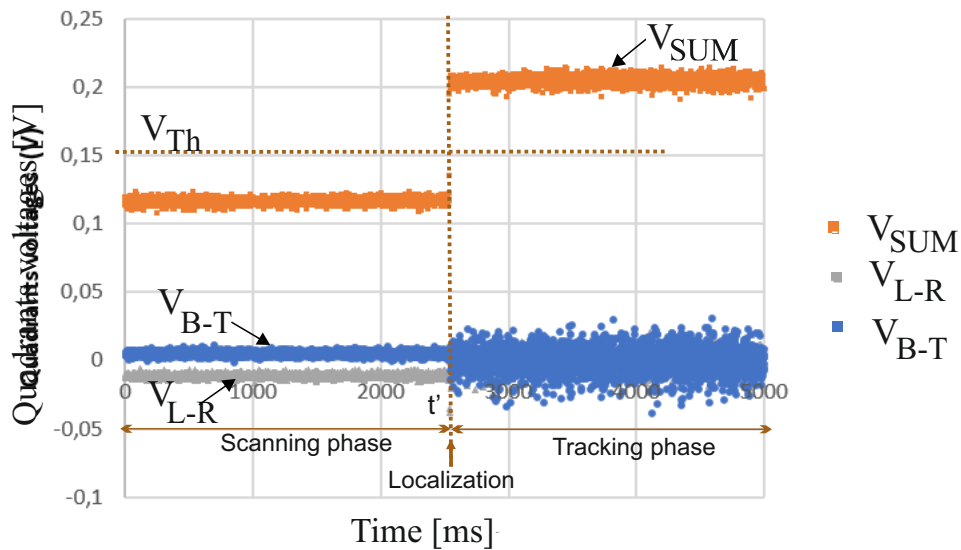


Figure 3.13: Quadrants output voltages during scanning, localization and tracking phase

Figure 3.14 illustrates the tracking of the micro-conveyor in x and y directions, moving over the smart surface in an open loop. The path of the micro-conveyor is not controlled by our optical sensor. Fig. 3.14 (a) shows the micro-conveyor placed at the center of the surface, before localization for time $t < t'$. Fig. 3.14 (b), shows that the laser light illuminates the CCR placed at the center of the micro-conveyor indicating that the micro-conveyor is localized at time $t = t'$. Next, in an

open loop control, the micro-conveyor starts to perform linear movements along the x-and y-axis. Fig. 3.14 (c and d) show two positions of the micro-conveyor over the smart surface, where the micro-conveyor carries out displacements of Δy and Δx from the center, for $t > t'$. We can see that the light beam successfully followed the conveyor while translating in the x- and y-axis.

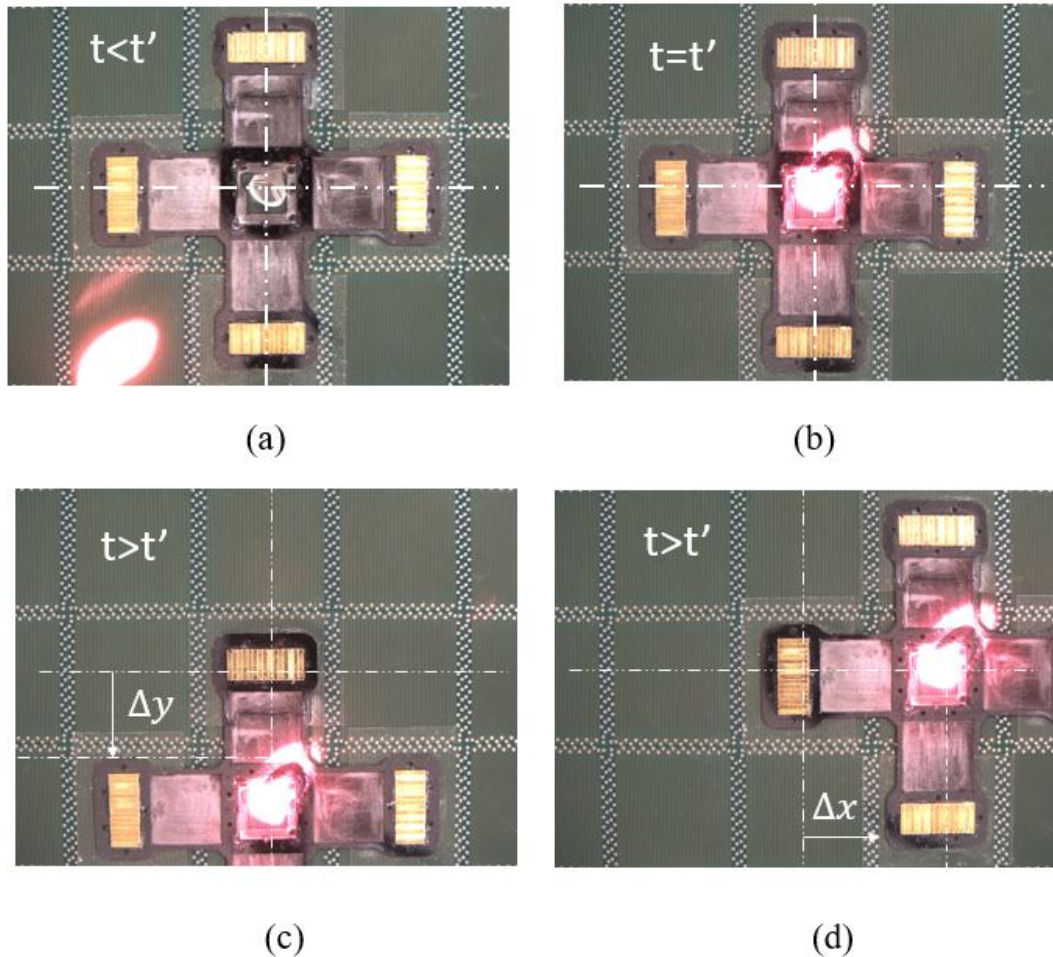


Figure 3.14: (a) The micro-conveyor holding a corner cube reflector at the center of the smart surface, (b) micro-conveyor holding a corner cube reflector at the center of the smart surface with light illuminating the corner cube reflector, (c) micro-conveyor with Δy displacement in y direction and light tracking and (d) micro-conveyor with Δx displacement in x direction and light tracking.

Next task is to test the tracking system for a couple movement of the micro-conveyor moving in a random trajectory. The micro-conveyor was moved by hand due to the difficulty of performing a complex trajectory using the conveying surface. An example of a random trajectory is presented in figure 3.15 (a). As seen in figures 3.15 (b, c and d), the laser beam continues to follow the micro-conveyor for each new position, which validates the system's capability to track the micro-conveyor's movement over a complex path. In the two previous experimental tests,

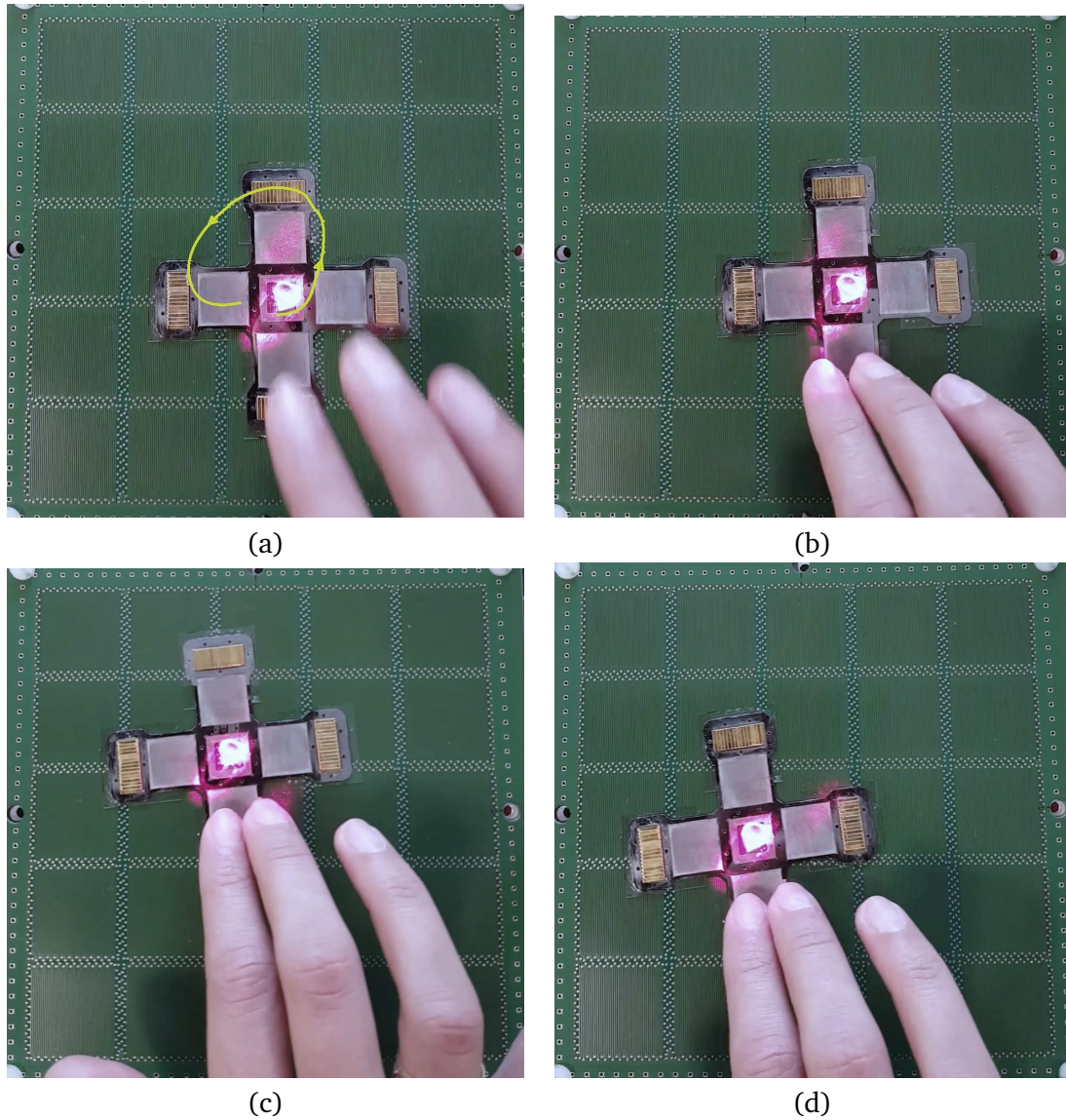


Figure 3.15: (a) Random trajectory of the micro-conveyor being tracked with (b, c, d) three different captures each for different positions of the path

we considered that the micro-conveyor was moving at a speed below the threshold value V_{max} , which is the speed limit above which tracking no longer works.

The rest of the section focuses on determining the V_{max} value. As mentioned in section 3.3, V_{max} is equal the maximum distance that CCR can travel before exiting the spot light (d_{max}) divided by the execution time of the tracking system to cover this distance (t_R).

Multiple factors influence the execution time of one iteration of the tracking system, such as the sensitivity of QPD, the MEMS mirror reconfiguration time, NI DAQ frequency and K_p 's value. Experimentally, the execution time of one iteration of the tracking system was measured to be equal to 14 ms. d_{max} is measured experimentally as the distance between the position of the CCR when at the center of spot ($V_{L-R} \approx V_{B-T} \approx 0$ and $V_{SUM} > V_{Th}$), and the position when the CCR exits

the light spot ($V_{SUM} < V_{Th}$). Using a camera, the distance was measured to be equal to 3.4 mm. Thus, by dividing the latter value by 14 ms, the system maximum speed should be 250 mm/s. However, in experimentation, the tracking was lost for a micro-conveyor having a velocity of 30mm/s. This means that the system performed 8 iterations in the control loop. To increase the V_{max} value, the number of iterations can be reduced by using a PID or a QPD with faster response. In addition, V_{max} can be increased by scanning the surface with a larger beam spot. However, in this case the QPD will receive less power and SNR decreases. A first possible solution is to use a laser with higher optical power. A second possible solution is to use a MEMS with a larger diameter to reflect more of the light returned by the CCR. Another solution is to use a bigger CCR to reflect more light. Nevertheless, by increasing the volume of the CCR, more weight will be added to the micro-conveyor, which cannot support a mass above 10g.

After validating our developed localization and tracking method, the next step is to control the trajectory of the micro-conveyor, in a closed loop control with the developed optical system.

3.6 Conclusion

In this chapter, a validation of the localization and tracking method (proposed in chapter 2) was presented and applied for a micro-conveyor moving over a 2D plane.

An electrostatic MEMS mirror was controlled using a controller and LabVIEW interface, in order to scan the surface, then to track the micro-conveyor after localization. The system demonstrated its capability to localize the micro-conveyor and to track it while moving over the surface. Two tests of the micro-conveyor's displacement were investigated during tracking phase. The first was in open loop with the surface, by making horizontal and vertical displacements. The second test, was done manually, making random and coupled trajectories. Finally, the maximum allowable speed for the micro-conveyor, before losing tracking, was analyzed and determined to be 30 mm/s

In the following chapter, the path of the micro-conveyor will be controlled, in a closed loop control system with the conveying surface according to the feedback from our developed optical sensor.

Chapter 4

Closed loop tracking with the smart surface

4.1 Introduction

This chapter pursues the system concepts and presentations that were developed in the previous chapter. In chapter 3, the localization and tracking of the micro-conveyor were realized in an open loop control system where the developed optical sensor was not used to command the conveying system. In this chapter, the micro-conveyor path is controlled in a closed loop with the smart surface using the feedback of our optical sensor. The system has to ensure the proper arrival of the micro-conveyor at its destination point with high accuracy by comparing its actual measured position with the final destination position. Thus, surface calibration is mandatory to obtain the coordinates of the micro-conveyor with respect to the surface, in order to sketch the outline of the conveyor's trajectory. In addition, the closed loop control system also highlights the need to know how to control the micro-conveyor's movements by understanding the functionality of the adopted electromagnetic conveying surface. This chapter is organized in the following order. First, it describes the actuation principle of the conveying surface. Next, it illustrates the importance of localization and tracking. Then, the chapter pursues by presenting the calibration solution to obtain the real time position of the micro-conveyor. Finally, it ends with the application of the closed loop control and presents the corresponding results.

4.2 Significance of localization

For a miniaturized robotic system, it is mandatory to supervise the micro-conveyor's displacement by a remote localization system, especially if there exist defective regions in the surface and/or if several micro-conveyors move at the same time on

the surface. With a remote localization system, the real time position of the micro-conveyors can be obtained. Then, the trajectory of each micro-conveyor can be optimized and the collision between micro-conveyors can be prevented by accelerating or decelerating their velocity of displacement depending on their respective positions and their task's priority order.

4.3 Electromagnetic conveying surface principle

At Roberval Laboratory, a planar flexible electromagnetic micro-conveyor was developed [Khan 17]. The advantage of our optical localization and tracking method is that it is less sensitive to the electromagnetic noise coming from the environment, such as the conveying surface.

The micro-conveyor's actuation degrees of freedom (DOF) are provided by four linear motors (LM). Each LM is an electromagnetic actuator composed of moving permanent magnets and fixed coils injected by supplied currents. Permanent magnet arrays (PMAs) are attached to the four edges of a thin cross-shaped platform, called a 'micro-conveyor'. Planar Electric Drive Coils (PEDCs) are placed in an orthogonal manner in the xy plane. LMs can be configured by arranging each PMA so as to face PEDCs. In this manner, we can represent four LMs such as LM_1 , LM_2 , LM_3 and LM_4 (see figure 4.1).

The four LMs are activated in order to generate motion forces which allow the micro-conveyor to move between any two points in the xy plane. By presuming that the LMs are installed along an axis without any error, then the resulting generated electromagnetic force is sum of the generated forces from each LM within an axis. Only, two active LMs are needed to achieve any linear displacement along a single axis. For instance, LM_1 and LM_2 are deployed to carry out a linear displacement along X-axis. In the same manner, LM_4 and LM_3 are deployed for a displacement along the Y-axis. The direction of the current that is injected into each LM controls the direction of the generated force. As a result, the direction of the motion can be reversed by changing the sign of the current injected into the PEDCs.

A torque is generated around the center of the mobile micro-conveyor upon reversing the direction of one parallel of the LMs with respect to the other along the same axis. Applying this technique results in the rotation of the micro-conveyor.

4.3.1 Actuation principle

For a single linear motor, the actuation principle is based on the generation of Lorentz forces. By placing a PMA above current carrying coils, an electromagnetic force is generated over the PMA. Since the PEDCs are fixed and the PMA is free, the PMA will displace in the xy-plane due to the generated force. The magnitude

of this force is calculated using the following equation:

$$F = I \int_{wire} dl \times B_{ext} \quad (4.1)$$

Where, F is the generated Lorentz force, l is the common length between the PMA and PEDCs, I is the current supplied into the PEDCs and B_{ext} is the external magnetic flux density, produced by the PMA. The relative orientation of the PMA magnetic field (B_{ext}) and the direction of the current carrying conductor determine the direction of the electromagnetic (Lorentz) force. The magnitude of this force is proportional to the magnitude of the supplied current (I), the intensity of the magnetic flux (B_{ext}), and the length of the coil underneath the PMA (l). These parameters can be maximized to increase the electromagnetic force intensity. This maximum value is limited by design constraints. For instance, increasing the magnitude of the current contributes to the Joule's heating effect. This heating in turn, harms the permanent magnetization of the PMA or may damage the coils. Also, any increase in the intensity of the magnetic flux density from the PMA demands a similar increase in the geometrical dimensions of the PMA. This implies that more weight is added and hence friction is increased between the micro-conveyor and the conveying surface when in motion. In order to decrease the force of friction between the two bodies, a glass plate is placed underneath each LMA.

4.3.2 Conveying surface architecture

To minimize energy consumption, the smart surface is decomposed into a matrix of cells to permit independent local activation. The smart surface has a dimension of $150 \text{ mm} \times 150 \text{ mm}$ and is composed of an array of 5×5 cells, [Bosc 16].

Each cell consists of two orthogonal layers of a set of serpentine coils as shown in Fig. 4.1. Each layer consists of two phase coils set in an overlapping planar coil layout each supplied with a current phase shifted by $\pi/2$. This layout achieves accordance with the magnetic pole orientation of the Permanent Magnets (PMs) in the PMA minimizes the number of input current source lines. The top and the bottom layers aid in generating motion along the x - and y -axes, respectively. The coils in the top (bottom) layer are fed with currents I_{x1}, I_{x2} (I_{y1}, I_{y2}). Where I_{x1} (I_{y1}) is phase shifted by $\pi/2$ with respect to I_{x2} (I_{y2}) as mentioned above.

Complex motion trajectories in the xy -plane are obtained through controlling the currents that are injected into the coils of the top and bottom layer. The velocity of the micro-conveyor is directly proportional to the frequency of the applied currents. By increasing the frequency, the micro-conveyor motion is accelerated.

The objective of the presented work is to control the micro-conveyor motion over the conveying surface in a closed loop control system in order to reach a

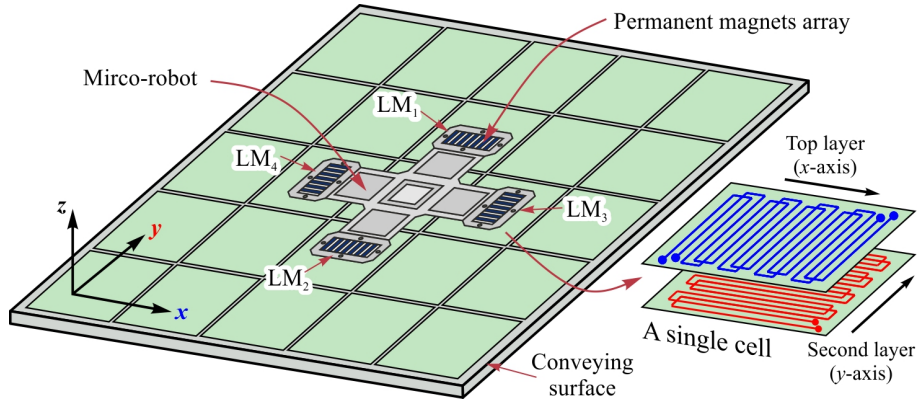


Figure 4.1: Schematic view of the micro-conveyor placed onto the conveying surface

defined final destination with high accuracy. To do this, the injected currents in the top and bottom layers of the conveying surface are regulated depending on the difference between the micro-conveyor's current position and its desired final destination. The current position is obtained in a real time application using feedback from the developed optical sensor and after calibrating the conveying surface.

4.4 Conveying surface calibration

The surface can be calibrated by finding the relation between the MEMS mirror's tip tilt angle (θ_x, θ_y) and the corresponding position coordinates x, y of the conveying surface. The sensor developed in the previous chapters is based on the tracking of the micro-conveyor by the MEMS mirror rotating over its axes. Each orientation of the mirror corresponds to a light spot position on the surface. The tracking principle requires that the micro-conveyor is placed at the center of this light spot. Due to the linearity between the applied voltages and the MEMS tip tilt angles, the control system is able to calculate the actual orientation of the MEMS mirror from the equations 3.16 and 3.17 illustrated in chapter 3.

In the experimental setup, a fixed mirror is installed between the MEMS mirror and the conveying surface, due to difficulties in directing the light directly from the MEMS to the conveying surface. Therefore, affine geometric formulas are not sufficient to find the desired relation. In addition, the occurrence of errors related to the measurement of angles and distance leads to imprecise measurement resolution. In this work, we have adopted the 2D projective transformation method between a fictive plane parallel to MEMS mirror, whose coordinates can be extracted by knowing the MEMS orientation, and the plane of the conveying surface [Mala 17], [Mala 18]. This method called homography, will be described in the

following subsection.

4.4.1 Homography method

Homography is a method that maps a set of points and lines from a plane to the corresponding projective plane and vice versa. Homography is also known by the terms projectivity or planar projective transformation [Dubr 09]. In fact, Homography is a projectivity mapping from plane π to plane π' if there exists a strictly non-singular 3×3 matrix \mathbf{H} that allows any point in the plane π represented by vector X_π to be mapped by a corresponding vector $X_{\pi'}$ on the plane π' and equal to HX_π . For instance, the 3D vector $X_\pi = (x_1, x_2, x_3)$ is a homogenous representation of a 2D point (x, y) , in the plane π , where $x = \frac{x_1}{x_3}$ and $y = \frac{x_2}{x_3}$. Similar reasoning is used for the vector $X_{\pi'}$.

In this work, π represents the micro-conveyor plane, which is the projection of a fictive plane parallel to that of the MEMS mirror $X_{\pi'}$ and vice versa, see fig 4.2. Homography projects quadrilateral shape between planes. For example, a

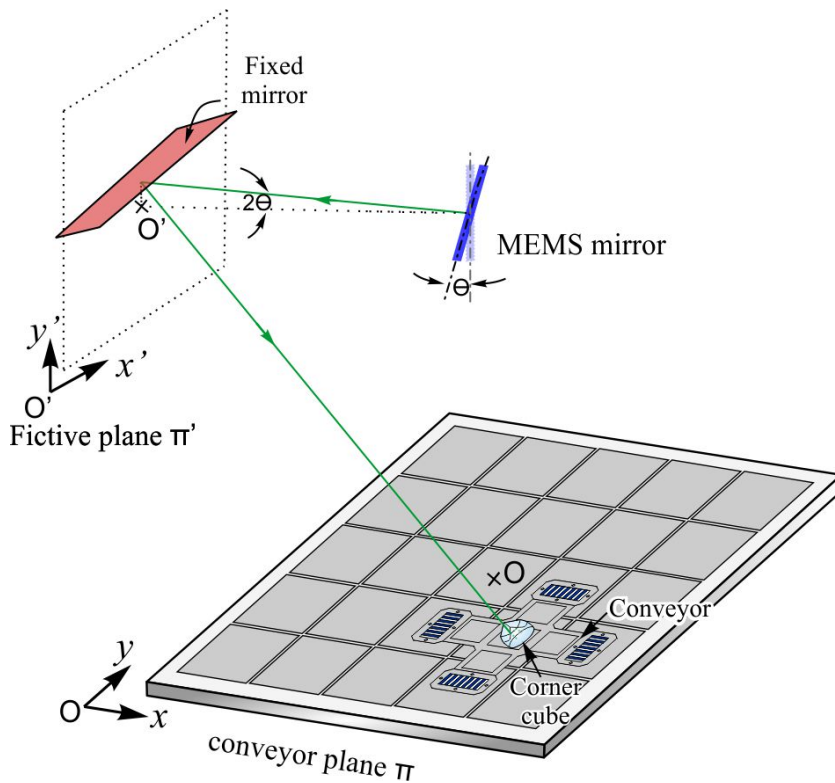


Figure 4.2: Projection between the fictive plane π' and the smart surface plane π .

square in the MEMS referential plane, by applying the matrix \mathbf{H} , gives another quadrilateral shape in the conveying surface, as shown in Fig.4.3. Moreover, the projection of the same quadrilateral by applying $\text{inv}(\mathbf{H})$ allows us to find the same square in the MEMS referential plane. Finally, in order to find the relation between those two planes, it is sufficient to determine the 3×3 homography matrix \mathbf{H} .

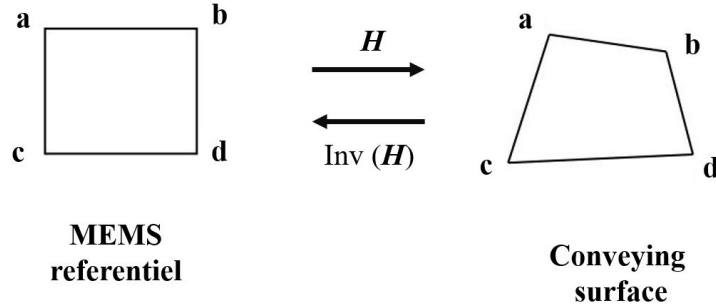


Figure 4.3: Homographic transformation between the MEMS and the conveying referentials.

4.4.2 Homography matrix calculation

The direct linear transformation (DLT) algorithm is adopted to solve the non-singular (3×3) homography matrix \mathbf{H} , given a sufficient set of point correspondences between the two planes [Dubr 09]. In this work the two planes are the conveying surface plane and the MEMS referential. The relationship between the two planes can be written as follows:

$$c \begin{pmatrix} x \\ y \\ 1 \end{pmatrix} = \mathbf{H} \begin{pmatrix} x' \\ y' \\ 1 \end{pmatrix} \quad (4.2)$$

Where $\mathbf{H} = \begin{pmatrix} h_{11} & h_{12} & h_{13} \\ h_{21} & h_{22} & h_{23} \\ h_{31} & h_{32} & h_{33} \end{pmatrix}$, c is a non zero constant, $(x \ y \ 1)^T$ represents \mathbf{X}_π

where (x, y) are the coordinates in the conveyor plane. $(x' \ y' \ 1)^T$ represents $\mathbf{X}_{\pi'}$ where (x', y') are the coordinates in the fictive plane parallel to the MEMS mirror.

The matrix \mathbf{H} contains 9 unknown elements h_{ij} (i, j from 1 to 3). However, the third row of the equation 4.2 is multiplied by a non zero constant (c), which implies that the elements h_{31} , h_{32} and h_{33} are directly related and one of those elements can be extracted from the two others. By consequence, the degree of freedoms of the matrix \mathbf{H} is reduced from 9 to 8. This implies that only 8 unknowns need to be solved.

A point correspondence between two planes gives the following two equations. They are obtained through the division of the first row of equation 4.2 by that of the third row, and the division of the second row by that of the third row.

$$h_{11}x'_i - h_{12}y'_i - h_{13} + (h_{31}x'_i + h_{32}y'_i + h_{33})x_i = 0 \quad (4.3)$$

$$-h_{21}x'_i - h_{22}y'_i - h_{23} + (h_{31}x'_i + h_{32}y'_i + h_{33})y_i = 0 \quad (4.4)$$

Equations 4.3 and 4.4 can be re-written in matrix form as follow:

$$\mathbf{A}_i \mathbf{h} = \mathbf{0}$$

where

$$\mathbf{A}_i = \begin{pmatrix} x'_i & -y'_i & -1 & 0 & 0 & 0 & x_i x'_i & x_i y'_i & x_i \\ 0 & 0 & 0 & x'_i & y'_i & 1 & -x'_i y_i & -y'_i y_i & -y_i \end{pmatrix}$$

and

$$\mathbf{h} = \left(h_{11} \quad h_{12} \quad h_{13} \quad h_{21} \quad h_{22} \quad h_{23} \quad h_{31} \quad h_{32} \quad h_{33} \right)^T$$

Since every correspondence point results in two equations that are linearly independent, it is enough to provide 4 correspondence points in order to solve \mathbf{H} with 8 degrees of freedom. A single (8×9) matrix \mathbf{A} can be formed by stacking four (2×9) \mathbf{A}_i matrices on top of one another. Each \mathbf{A}_i is obtained from one correspondence point. \mathbf{H} will be extracted from \mathbf{h} . In reality and due to system noise, the correspondences are not exact, thus there will be no exact solution for \mathbf{H} . Using more than four correspondences provides a more concrete solution of \mathbf{H} . However, the new challenge is to solve \mathbf{H} with more than 8 equations. The adopted solution is to minimize the norm of $\|\mathbf{A}\mathbf{h}\|$, i.e by minimizing the algebraic distance. To ensure that the selected \mathbf{h} isn't the zero vector, the constraint $\|\mathbf{h}\| = 1$ is added. The solution to the problem is to obtain the Singular Value Decomposition (SVD) of \mathbf{A} . In fact, \mathbf{A} is decomposed to be equal to the product of three matrices $\mathbf{A} = \mathbf{U}\mathbf{S}\mathbf{V}^T$, where the diagonal elements of \mathbf{S} are positive real entries, the columns of \mathbf{U} and \mathbf{V} are orthonormal. The solution of \mathbf{h} is the last column of the matrix \mathbf{V} . Finally, by reshaping the matrix \mathbf{h} , the homography matrix \mathbf{H} is obtained.

We have developed the DLT algorithm for n measurements in MATLAB code, which can be summarized by the following steps:

- Enter the n correspondence data in the system
- Compute \mathbf{A}_i for each correspondence point
- Assemble n (2×9) matrices of \mathbf{A}_i into a single $2n \times 9$ matrix
- Obtain \mathbf{h} from the SVD calculation of \mathbf{A}
- Obtain \mathbf{H} from \mathbf{h}

The set of n corresponding points used to construct the matrix is measured and stored in an offline database. The coordinates x' and y' from the fictive plane can

be calculated from the values of θ_x and θ_y , since this plane is parallel to the MEMS mirror plane. In fact, when the mirror rotates by an angle θ , the reflected beam moves by an angle equal to 2θ (as illustrated figure 3.6 of chapter 3) so from the following trigonometric formulas x' and y' can be written as:

$$x' = D \times \tan(2\theta_x) = D \times \tan\left(2 \times \frac{V_{diffx}}{k_x}\right) \quad (4.5)$$

$$y' = D \times \tan(2\theta_y) = D \times \tan\left(2 \times \frac{V_{diffy}}{k_y}\right) \quad (4.6)$$

Where D is the distance between the MEMS mirror and the fixed plane mirror. θ_x and θ_y are obtained from the applied voltages sent to the MEMS mirror (V_{diffx} , V_{diffy}) by applying the linearity formulas of equations 3.16 and 3.17, from chapter 3. Thus, the second part of the equality of equations 4.6 and 4.5 is obtained. In practice, the command voltages to which we have access are v_x , v_y sent by the LabVIEW code. However, a proportional relationship exists between these values and the values V_{diffx} and V_{diffy} , respectively. As a result, the coordinates x' , y' of each point can be obtained by reading the v_x and v_y values sent by the LabVIEW code.

The x , y position, i.e the corresponding center of the spot position can be extracted and measured using a vision method using a camera placed above the conveying surface, following an algorithm explained in section 4.4.4. Thus, the offline database records n applied voltages with their n corresponding captured photos.

4.4.3 Homography applications

Once matrix \mathbf{H} is calculated, two applications can be carried out. The first is to find the unknown coordinates relative to the conveying surface (x , y) from knowledge of the corresponding coordinates in the MEMS referential, based on equation 4.2. This application is used for the closed loop tracking system with the conveying surface. The system corrects the extracted current position of the micro-conveyor to get closer to the final destination point.

The second application is to find the coordinates of a point in the MEMS referential from the knowledge of a point on the conveying surface, by applying the inverse of matrix \mathbf{H} as follows:

$$\begin{pmatrix} x' \\ y' \\ 1 \end{pmatrix} = c \text{inv}(\mathbf{H}) \begin{pmatrix} x \\ y \\ 1 \end{pmatrix} \quad (4.7)$$

This method serves in scanning the surface with a specified desired shape with defined values of x and y . For example, due to the fixed mirror used in the setup (see figure 3.12, in chapter 3) the circular spiral sent to the MEMS mirror gives an elliptical spiral pattern over the conveying surface, since the two planes are not parallel.

In order to obtain a circular spiral as seen in figure 4.4, the following steps must be performed.

First, calculate the desired spiral coordinates x and y in the conveying surface plane 4.4 (a), then calculate the corresponding coordinates in the referential plane 4.4 (b) from equation 4.7, and finally send the applied voltages to the MEMS mirror obtained from equations 4.5 and 4.6. The result is shown in figure 4.4 (c).

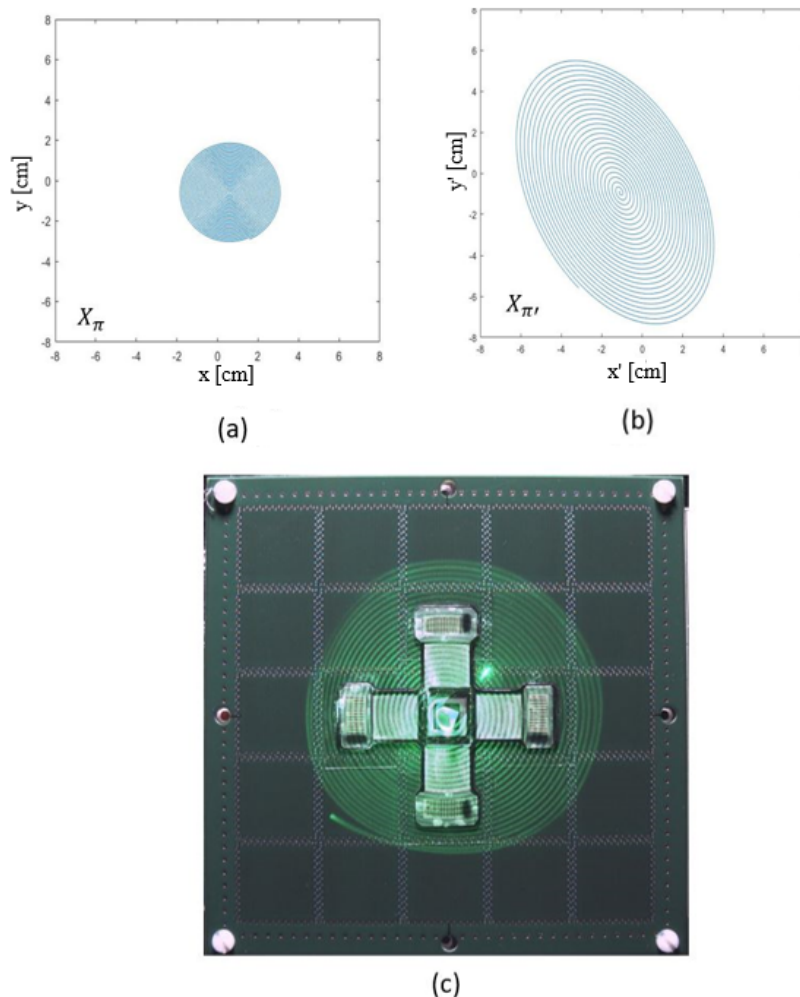


Figure 4.4: Full circular spiral scanning over the conveying surface (a) in the conveying referential; (b) in the MEMS referential; (c) photography of the surface with spiral scanning

4.4.4 Vision system camera calibration

Vision-based systems are commonly used to locate and track a mobile target [LAUR]. However, the resolution of a vision method is inversely proportional to the field of view captured by the camera, which in our case is the size of the conveying surface. In order to maintain a high tracking resolution over a relatively large surface, several cameras must be implemented above the surface, leading to complex image processing and increasing the cost of the system. In addition, the operating speed becomes slower, in the case of a camera-based tracker, due to the limited frame rate of the image sensors and the much greater amount of data processing required [MÄK 00].

Yet, the vision system will serve, in a preliminary step, to calibrate the conveying surface. The advantage of our method is that there is no speed constraint on the acquisition and extraction of the (x, y) coordinates by the camera, since this is an offline process that is performed only once before the localization and tracking system is launched. Moreover, the proposed calibration process can be applied regardless of the size and shape of the conveying surface and using a single camera. This camera can be translated in order to cover the whole conveying surface. The displacement of the camera can be ensured by placing it on two orthogonal accurate linear mechanical actuators.

Figure 4.5 describes the vision system algorithm scheme used to obtain the matrix \mathbf{H} , for n correspondence points (between the conveying plane and the MEMS referential). The process starts by calibrating the camera using a distortion target as a reference (dots grid from Edmund Optics with a pitch of $125 \mu\text{m}$). In this work, a camera with a resolution of 2580×1536 pixels is placed above the conveying surface. The camera must be aligned with the conveying surface such that its lines and columns are aligned with the axes of the conveying surface, as seen in Fig. 4.6. The resolution depends on the camera elevation above the conveying surface and its zoom setting. The position zero of the camera captures the center of the conveying surface. For the case where the camera captures a portion of the conveying surface, an offset will be added to the extracted x, y position inside the frame depending on the camera position, in order to maintain one general plane reference.

For simplicity, the light spot on the conveying surface is considered as the reference template used to extract the (x, y) coordinates of the micro-conveyor. The tracking system makes the center of the spot light confounds with the center of CCR, i.e, center of micro-conveyor. This simplification avoids the need to control and modify the position of the micro-conveyor, by injecting currents into the coils of the surface. In addition, in the case where n is relatively large and the

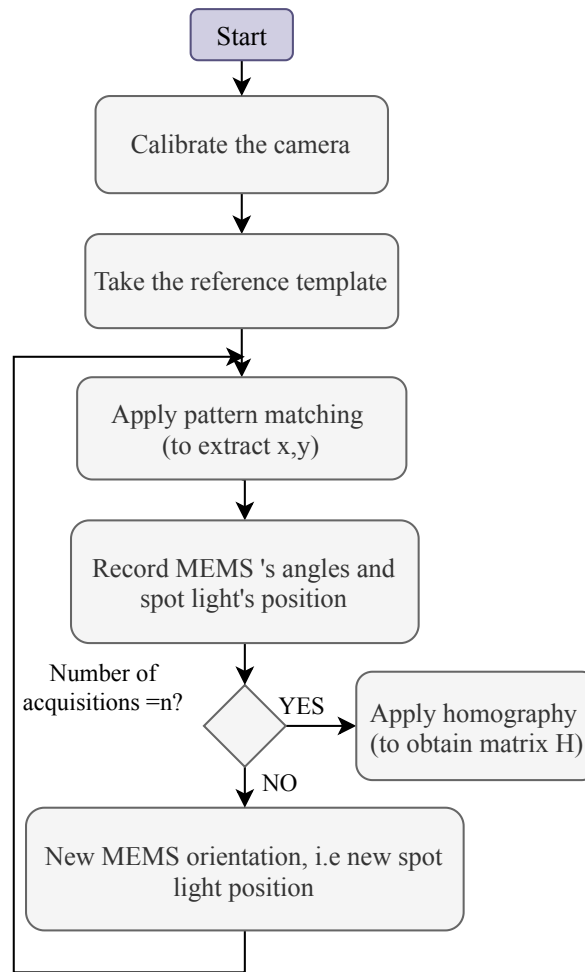


Figure 4.5: Vision system scheme algorithm used for the surface pre-calibration

micro-conveyor is actuated for a long time, the surface can heat and damage the micro-conveyor. Thus, to save energy and time, the calibration is performed using the spot light as the pattern.

Next, the image pattern (i.e, reference template) with the dimensions of the spot light, as seen in figure 4.7, serves for the pattern matching process to extract the coordinates of the spot to be recorded in the offline data base with the corresponding MEMS orientation. The process of pattern matching is repeated for a new orientation of the MEMS until the number of the acquired data points is equal to the desired size of the offline data base which is equal to n . As mentioned before, four correspondence points ($n = 4$) is the minimum number to construct the matrix \mathbf{H} . An optimization study is carried out in the next section to find the optimal value n that constructs the most accurate matrix \mathbf{H} possible.

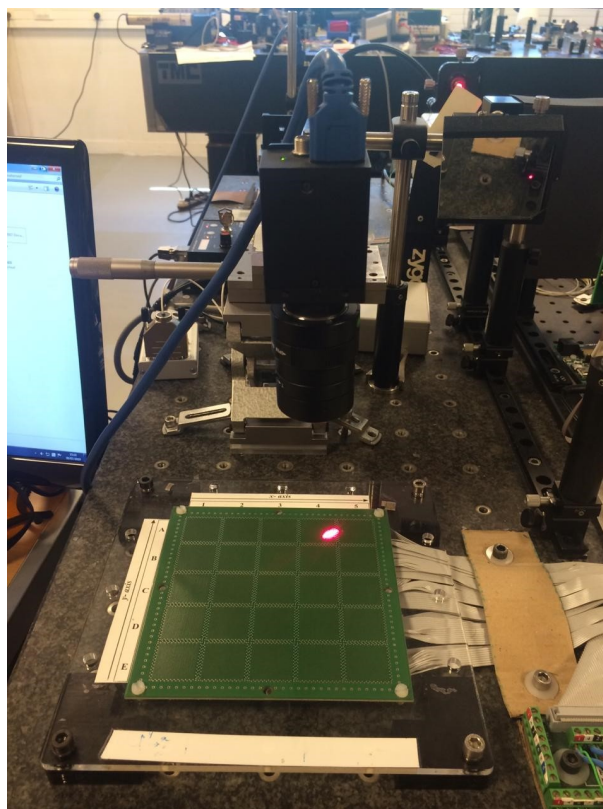


Figure 4.6: Implementation of the camera above the conveying surface

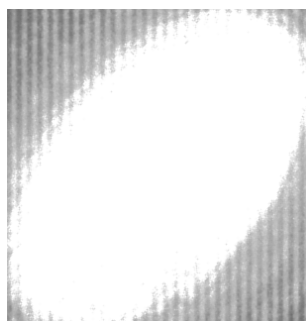


Figure 4.7: Spot template to be acquired

4.4.5 Optimization of homography matrix

A study was performed to obtain the most accurate matrix \mathbf{H} possible, that is the one giving the smallest error between the projected values (using homography) and the exact values of the spot light coordinates (x, y) . The exact values are considered to be the values measured by the camera in offline mode. In order to find the best homography matrix with the lowest possible error, an investigation of the number n used to build the matrix \mathbf{H} was carried out. In this work, only the 3×3 centered cells of the conveying surface are functional and connected to the current generators, thus the center of the micro-conveyor will not reach the

other areas. For this purpose, calibration will only be performed in the zone of interest illustrated in fig 4.8. This figure represents the field of view captured by the camera. In such a setup, the camera resolution is equal to $45 \mu\text{m}/\text{pixel}$.

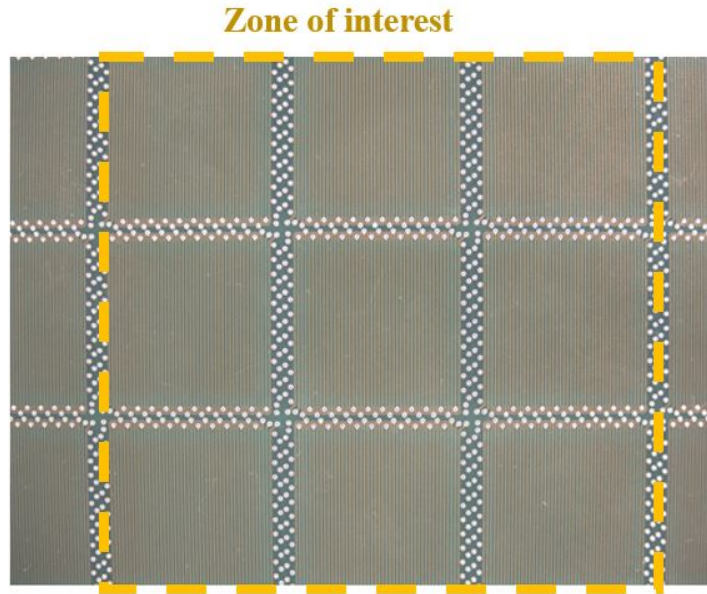


Figure 4.8: Field of view of the camera for a resolution equal to $45 \mu\text{m}/\text{pixel}$

In the experimental work, the system acquires $39 \times 39 = 1521$ points. we chose 39 because it is multiple of 3, where 3 cells need to be covered. Figure 4.9 shows how the 1521 points are distributed over the zone of interest. Each point in this graph represents the x and y coordinates of the light spot measured by the camera.

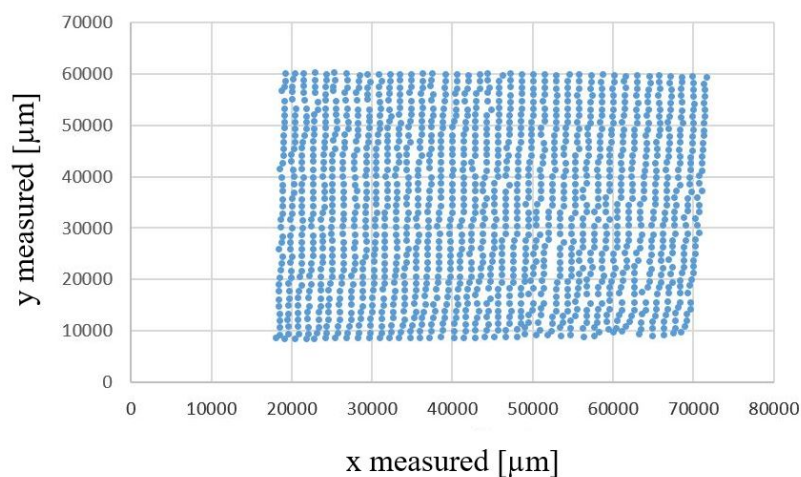


Figure 4.9: The distribution of the 39×39 measured points over the conveying surface

Although the data acquisition was carried out to have identical steps between

each consecutive point, it can be observed in the figure 4.9 that the pattern of measurement points is deformed. This is due electronic and digitization noise affecting the control voltages sent to the MEMS. As a consequence, errors occurs in the θ_x , θ_y angles obtained, i.e. spot positions over the conveying surface. In addition, errors can occur from camera measurements, such as optical distortion due to a fisheye effect of the camera lens and errors in pattern matching when the spot size changes from one position to another (as demonstrated in chapter 2 and 3), whereas it is still compared with the same referential spot light pattern.

In order to analyze the influence of the number of points, n , used to construct the matrix \mathbf{H} , we calculated from the same set of 1521 points, 9 different matrices \mathbf{H} each with different number n . Figure 4.10 shows the positions of the $n \times n$ chosen points (presented in blue dots), with respect to the total set of points (the 1521 points presented in orange dots). The sizes of n are $n = 2 \times 2$, 4×4 , 5×5 , 6×6 , 10×10 , 13×13 , 20×20 and 30×30 . In addition to the matrix with $n = 39 \times 39$, which uses the whole set of a variable points, see fig 4.9.

For each matrix \mathbf{H} , we recalculated the values (x, y) of the $N = 39 \times 39 = 1521$ points by multiplying the matrix \mathbf{H} by the correspondence points in the referential plane (see equation 4.2).

$Errorx_i$ and $Errory_i$ are the absolute error values in the x-and y-axes between the measured and recalculated values, based on the following formula:

$$Errorx_i = \|x_{measured\ i} - x_{recalculated\ i}\| \quad (4.8)$$

$$Errory_i = \|y_{measured\ i} - y_{recalculated\ i}\| \quad (4.9)$$

Where i varies between 1 and $39 \times 39 = 1521$. The error in the distance of one point (i) is equal to:

$$ED_i = \sqrt{Error\ x_i^2 + Error\ y_i^2} \quad (4.10)$$

The average and root mean square of the distance error are calculated, for each matrix H having the following formulas:

$$AVG = \frac{1}{N} \sum_{i=1}^N (ED_i) \quad (4.11)$$

$$RMS = \sqrt{\frac{1}{N-1} \sum_{i=1}^N (\|ED_i - AVG\|^2)} \quad (4.12)$$

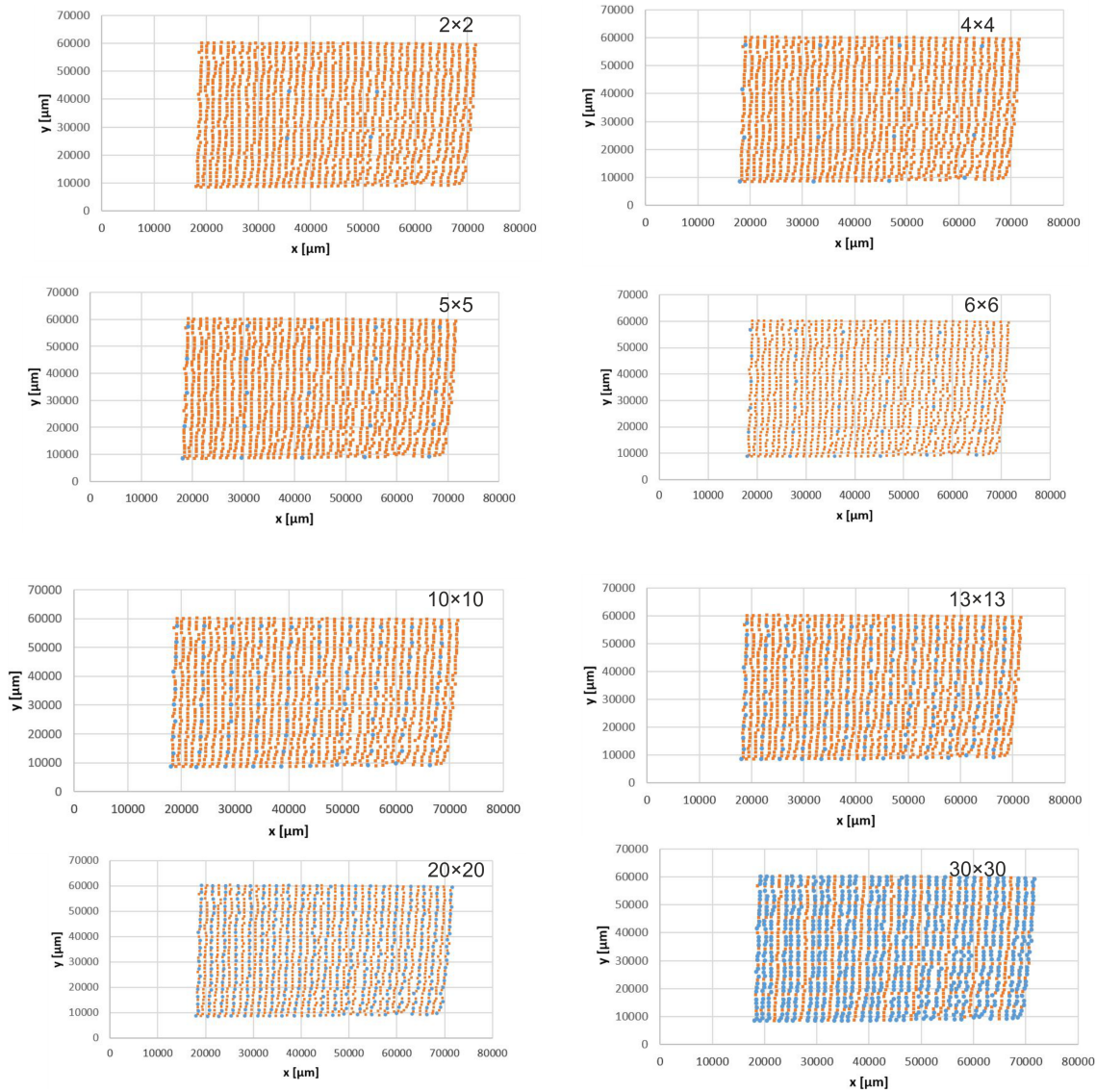


Figure 4.10: Evolution of the distance error with respect to the number of acquisition points

Where N is the total size of the set of points equal to $39 \times 39 = 1521$. The obtained values for each matrix are compared and presented in table 4.1.

The figures 4.11 and 4.12 show the evolution of the average and the root mean square of the error distance as functions of \sqrt{n} . From these results, we state with increasing in the number of n , the error improves up to a certain limit. Thus, we chose the first n that gives a low error, so as not to overload our database. An optimal solution is for n equal 20×20 , that gives an average and root mean square of the error distance, equal to $276.37 \mu\text{m}$ and $159.39 \mu\text{m}$, respectively.

The recalculated x, y values obtained from the matrix H for $n = 20 \times 20$, are presented in 4.13. As seen in figure 4.13, the distribution of points does not have the same layout as the layout of the original measured points presented in figure

Table 4.1: Average (AVG) and root mean square (RMS) of the error distance (ED) for different H matrices calculation using camera sensibility equal to $45 \mu\text{m}/\text{pixel}$

Number of points [n]*	AVG of 39×39 ED [μm]	RMS of 39×39 ED [μm]
2×2	631.09	492.69
4×4	381.33	229.67
5×5	320.89	178.71
6×6	314.61	179.29
10×10	297.25	167.20
13×13	285.80	160.93
20×20	276.37	159.39
30×30	274.31	158.26
39×39	270.39	157.56

*: n is the number of points used to construct the matrix H

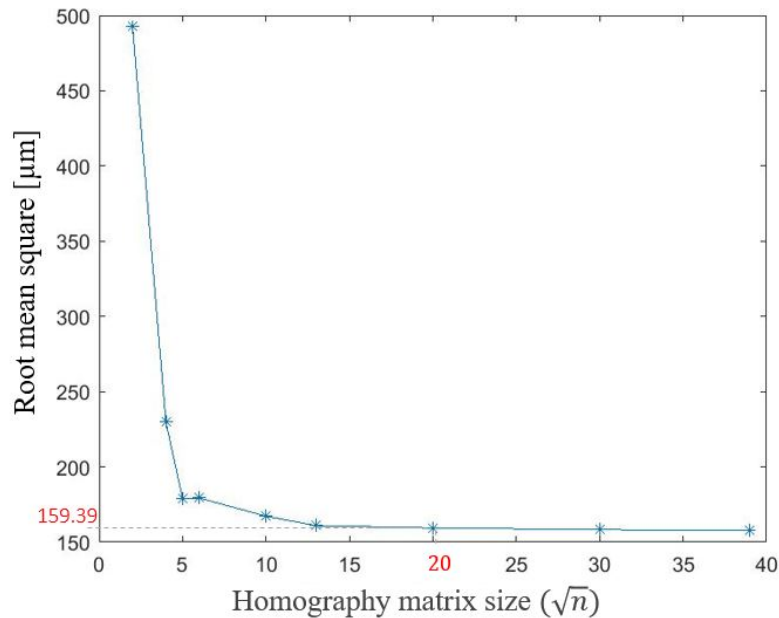


Figure 4.11: Evolution of the root mean square of the error distance with respect to the number of acquisition points

4.9. This is due to the fact projection homography does not work properly when the measured data are distorted. In fact, the role of homography is to find the best quadrilateral that replaces the measurement points with the least error. Figure 4.14 is an example of disturbed measured points with the corresponding recalculated points using homography. The recalculated points are obtained in a way that they matches the layout of the measurement points, with least distance error between them. If a single global homography is used, a significant distance error is obtained (see figure 4.14 (a)), when compared to the error obtained when us-

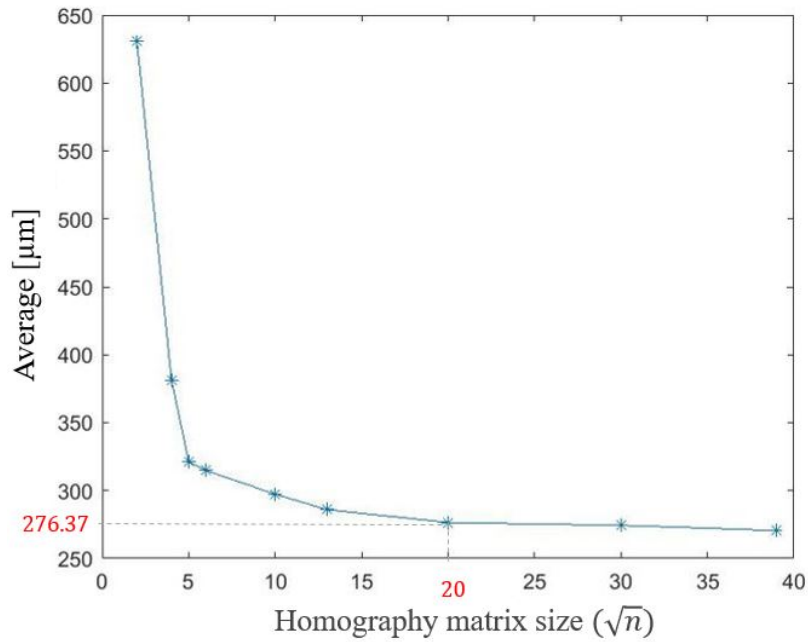


Figure 4.12: Evolution of the average of distance error with respect the number of acquisition points

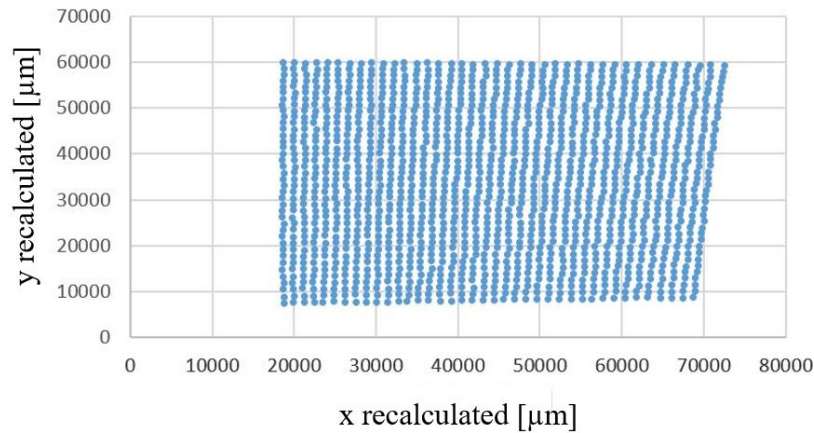


Figure 4.13: The distribution of the 39×39 recalculated points using matrix H of $n = 20 \times 20$

ing local homography (see figure 4.14 (b)). Local homography divides the global region into sub-regions, each possessing its own homography matrix. The trapezoid of each sub-region will adjust better to its local region, giving a lower error distance.

In this work, the zone of interest is divided into 9 sub-regions, named: C1, C2, C3 ... C9, as seen in Figure 4.15. In this case, during the tracking phase when the micro-conveyor is moving on the surface, its coordinates are calculated using

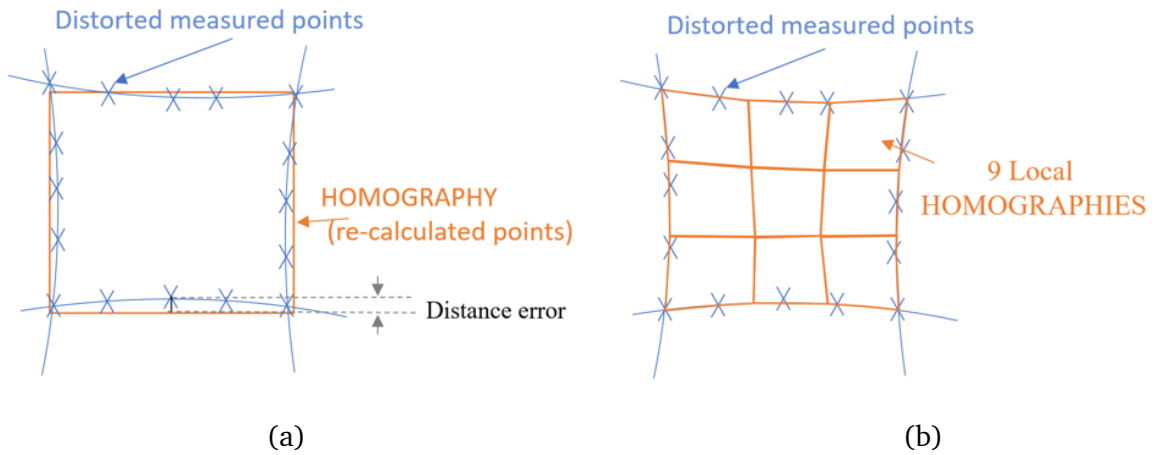


Figure 4.14: Difference between global (a) and local (b) homography: local homography better fits the distorted measured points

the matrix \mathbf{H} that corresponds to the region it occupies. To know which region the micro-conveyor occupies, we apply the least square distance method between the actual MEMS orientation and the MEMS orientation stored in the database.

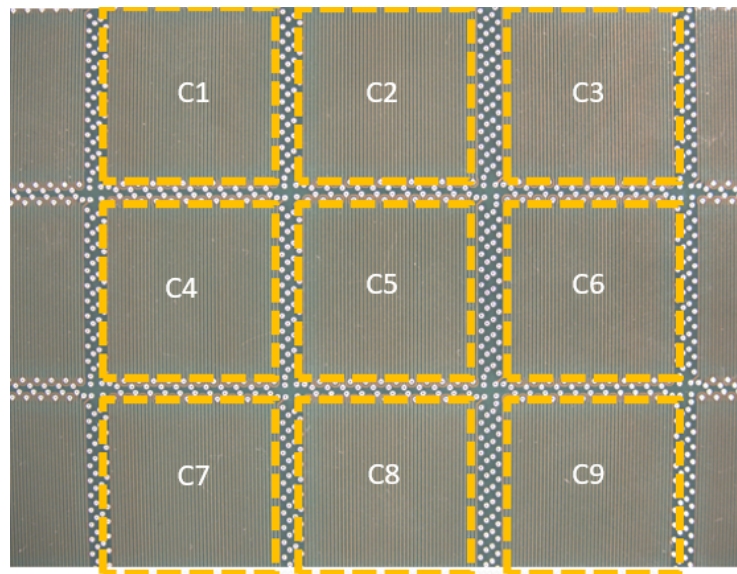


Figure 4.15: Regions of local homography over the conveying surface

To calculate the matrix \mathbf{H} of each local region, we use the already stored correspondence points of $n = 39 \times 39$. In fact, for nine cells, 39 is divided by 3 in columns and rows, thus, each local homography is calculated for $n = 13 \times 13$.

An evaluation of each matrix \mathbf{H} was performed by re-projecting the $13 \times 13 = 169$ points, and calculating the distance error of each point, i.e. ED_i between the measured and recalculated values, where i ranges from 1 to 169. Average and the root mean square of the error distance are calculated from equations 4.11 and

4.12, respectively, for N equals 169. The results of each cell are listed in table 4.2 of each cell.

Table 4.2: Average (AVG) and root mean square (RMS) of the error distance (ED) for the nine local homography matrices, using camera resolution of $45 \mu\text{m}/\text{pixel}$

Cell [$n = 13 \times 13$] *	AVG of 13×13 ED [μm]	RMS of 13×13 ED [μm]
C1	129.40	73.87
C2	142.53	92.42
C3	245.59	139.14
C4	122.12	65.28
C5	125.97	72.45
C6	136.02	83.73
C7	181.69	110.40
C8	149.18	76.29
C9	125.95	65.86

*: n is the number of points used to construct the matrix \mathbf{H}

The in-homogeneity between the errors values obtained for each cell, as presented in table 4.2, is related to the way the laser reaches the surface. Indeed, the size of the light spot, on the conveying surface, differs from one cell to another, with the variation of the values θ_x and θ_y of the MEMS mirror. Thus, the pattern matching application between the light spot to be measured and the pattern reference, will not be same. This results in the in-homogeneity of the error values obtained in table 4.2.

Furthermore, the values obtained from local homography method in table 4.2 show better accuracy compared to the values resulting from the global method, presented in table 4.1. Figure 4.16 illustrates the combination of the recalculated points of each zone of the nine cells. The assembled layout is closer to the original measurement of the figure 4.9, than the results of 4.13, indicating that in this case local homography is a better solution than global homography.

Another test was performed, by changing the camera's field of view, to examine the ability to further optimize these values. The zoom setting and/or camera elevation was changed to capture only one cell of the smart surface. Figure 4.17 represents the field of view of the camera capturing the central cell (C5).

The camera vision system algorithm was repeated with the new setup, with the new field of view. The camera was re-calibrated and a new spot light pattern captured. The new resolution of the camera setup was equal to $20 \mu\text{m}/\text{pixel}$, instead of $45 \mu\text{m}/\text{pixel}$. A new set of correspondences points was acquired to calibrate the zone of interest (C5). The size of the set of correspondence points, within this cell, was chosen to be 20×20 , since the previous study gave the best

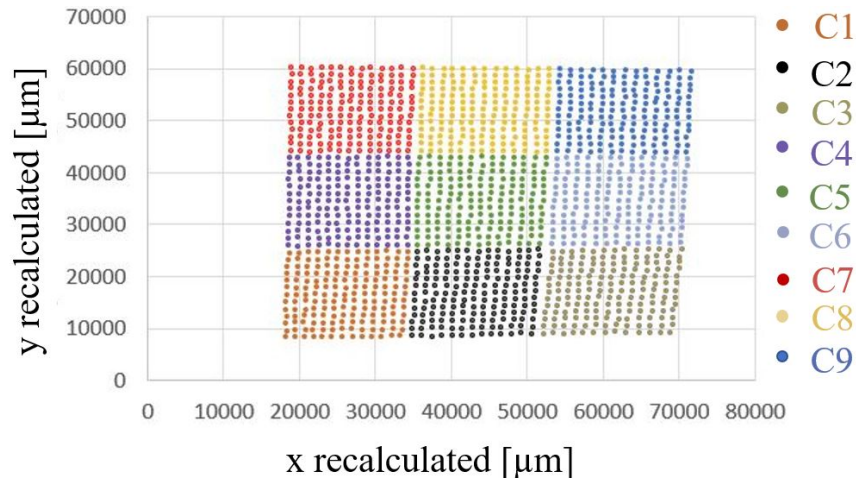


Figure 4.16: Assembled measured points from the local homography

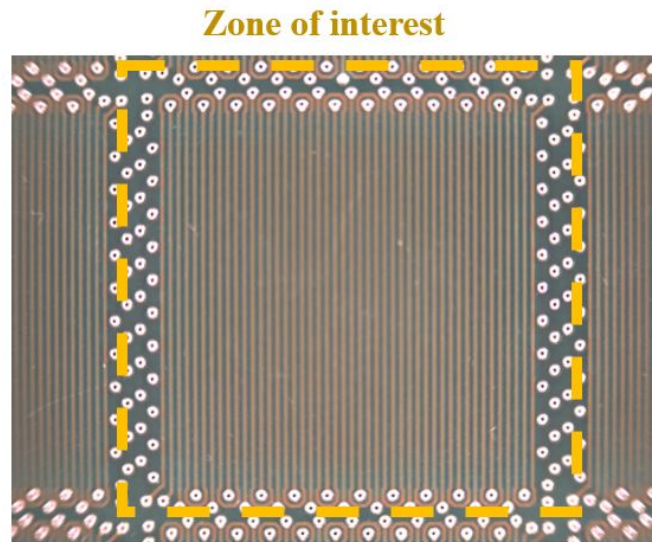


Figure 4.17: Field of view of the camera for sensibility equal to $20 \mu\text{m}/\text{pixel}$

error value for $n = 20 \times 20$, see table 4.1.

Different tests were performed to examine the effect of increasing n , used to construct the matrix \mathbf{H} , on the resulting errors. The values of n used were: $n = 2 \times 2$, 4×4 , 7×7 , 10×10 and 20×20 , generating 5 different values of \mathbf{H} . The error distances (ED_i) are calculated between the measured points and the recalculated distance obtained for each matrix \mathbf{H} , where i varies from 1 to 20×20 . The average and root mean square of the obtained error distance, obtained from each matrix \mathbf{H} , are calculated using equation 4.11 and 4.12. The obtained values are presented in table 4.3. As seen in this table, the error improved by increasing the value of n until a certain limit reaching an average and root mean square of error distance equal to $129.6 \mu\text{m}$ and $67.9 \mu\text{m}$, respectively.

Table 4.3: Average (AVG) and root mean square (RMS) of the error distance (ED) for different H matrices calculations using a camera resolution of $20 \mu\text{m}/\text{pixel}$

Number of points [n]*	AVG of 20×20 ED [μm]	RMS of 20×20 ED [μm]
2×2	154,09	88,96
4×4	152,47	87,44
7×7	132,68	72,38
10×10	128,86	70,84
20×20	129,57	67,93

*: n is the number of points used to construct the matrix \mathbf{H}

These limit values, which correspond to the field of view at $20 \mu\text{m}/\text{pixel}$, are better than the limit values obtained in table 4.1 for a camera having a larger field of view $45 \mu\text{m}/\text{pixel}$. However, the values for a small field of view are similar to the values of the cell C5 presented in table 4.2. This can be explained by the fact that in both cases, the local homography principle is adopted but with different pixel resolutions. For such surfaces, the pixel resolution didn't enhance the AVG and RMS of the error distance.

As a conclusion, in this work and for the size of surface we are using, we will adopt local homography for $n = 13 \times 13$, using a camera resolution of $45 \mu\text{m}/\text{pixel}$. In this way, we avoid complexity of moving the camera with smaller field of view, to cover the entire surface. However, for a larger surface area, with the same field of view ($45 \mu\text{m}/\text{pixel}$), the camera must move to maintain the same order of accuracy, the number of local homography matrices increasing to cover the new size of the surface.

4.5 Closed loop tracking of micro conveyor with electromagnetic surface

4.5.1 Control chain

The block diagram of the closed loop control of the micro-conveyor's displacement is presented in Figure 4.18 (used in chapter 3). The goal is to guide the micro-conveyor to move from its current position to a desired position, by using the feedback signal provided by our developed optical sensor.

At first, the desired position of the micro-conveyor with coordinates (x_{des}, y_{des}) is compared to the measured position (x_{mes}, y_{mes}) , is calculated via the homography matrix \mathbf{H} . The difference between these two values (Δ_x, Δ_y) is regulated with a proportional controller, implemented in a LabVIEW interface, to generate the

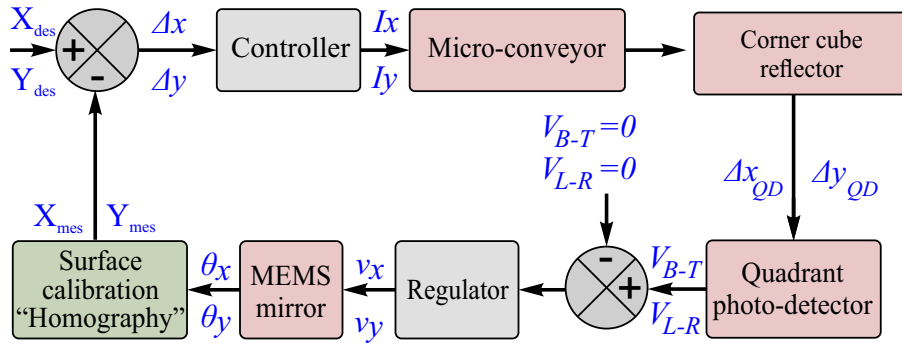


Figure 4.18: Block diagram of the closed loop control of the tracking system

corresponding supplied currents values (I_{x1} , I_{x2} , I_{y1} and I_{y2}) sent to the conveying surface. With the new current values, the micro-conveyor moves to a new position thanks to the Lorentz force. As a consequence, the photo-detector (QPD) receives a new orientation of the reflected beam 6 coming from the CCR (see Fig.3.12, chapter 3) resulting in significant values of V_{B-T} and V_{L-R} . Then, the MEMS corrects its orientation to re-center the beam light over the photo-detector's surface, as described in section 3.4.1. Using the homographic calibration method, the new position of the micro-conveyor is calculated by reading the new values of v_x and v_y , (in direct relation to the angles θ_x and θ_y of the MEMS mirror). Δ_x and Δ_y are the positioning errors between the actual and the desired position in x - and y -axis, respectively. If these values are less than a defined threshold value ε , the closed loop stops.

4.5.2 Experimental results

In this section, a validation test of the proposed method along the x - and y -axis is presented. Figure 4.19 represents a capture of the system setup with a zoom on the conveying surface. In the zoomed in capture, the micro-conveyor is illuminated by the light spot reflected by the MEMS mirror.

In figure 4.19, the origin of the coordinate system (x , y) is the point O which is the center of the surface and the micro-conveyor is at position A. As a first experimentation, the goal is to test the closed loop tracking over the conveying surface. For simplicity, the global homography was adopted to extract the x , y coordinates of the micro-conveyor in a real time application.

The experimentation starts by scanning the surface, to localize and track the mobile micro-conveyor. Fig 4.20, shows the variation of the angles of the MEMS mirror, θ_x and θ_y , as a function of time.

For $t < t_1$, the system is launched to seek for the micro-conveyor by sending v_x and v_y voltage values as spiral coordinates in order to scan the conveying surface. Due to the linearity between applied voltages and the MEMS angles, the mirror

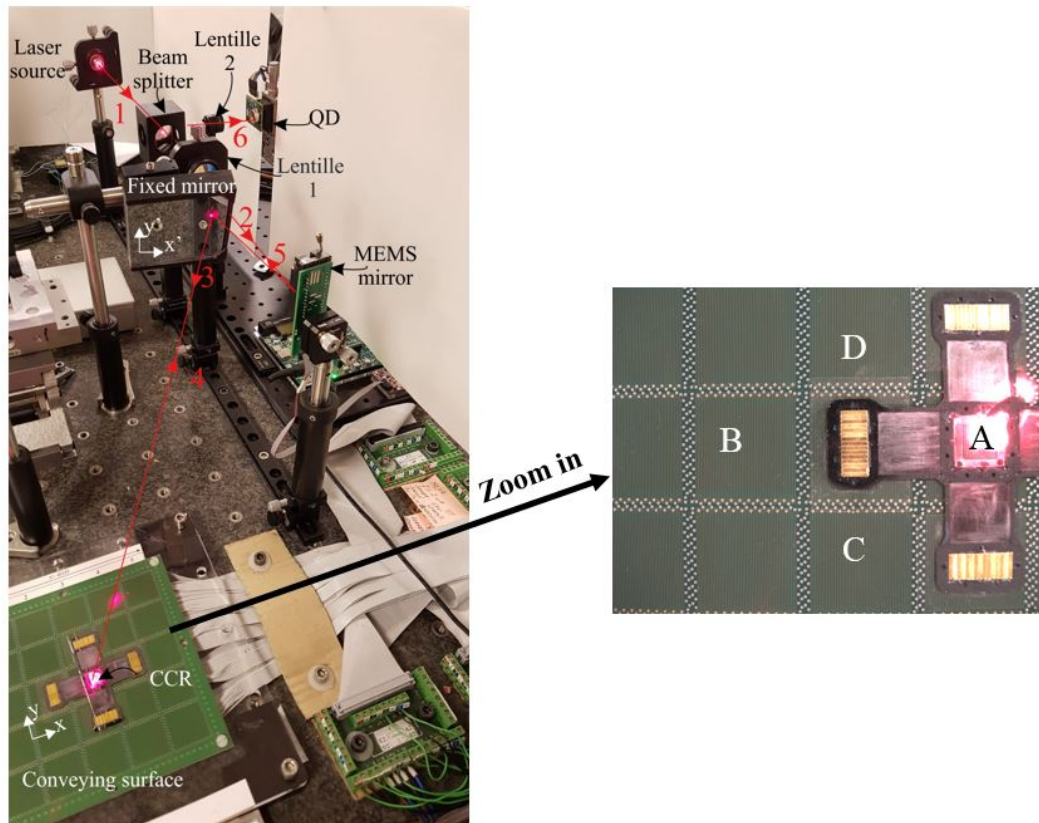
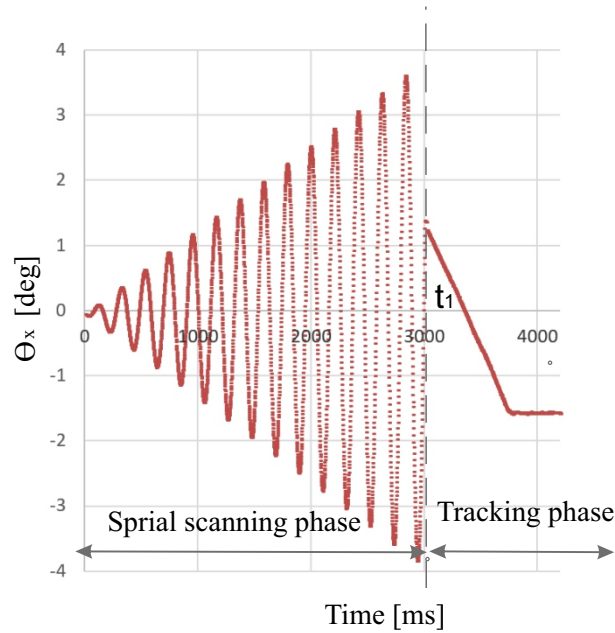


Figure 4.19: Photography of setup with a zoom in capture of the coordinates system of the conveying surface

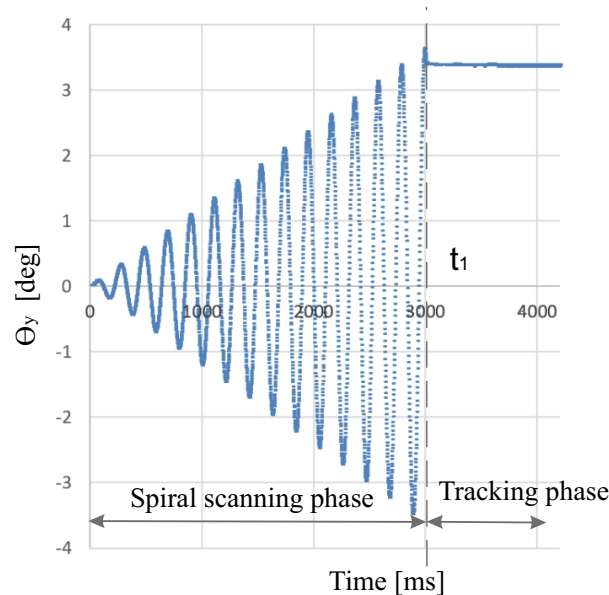
rotates to create a spiral scanning pattern. At time $t = t_1$, the laser beam reaches the micro-conveyor and hence localization occurs. The QPD generates a significant V_{SUM} value greater than V_{th} when receiving the reflected light beam coming from the corner cube reflector (beam 6, see fig 4.19). The MEMS mirror then stops the spiral scanning to switch to the tracking phase where the signals of V_{B-T} and V_{L-R} of the QPD oscillate around zero. For $t > t_1$, in a closed loop control system, the MEMS follows the displacement of the micro-conveyor moving over the surface.

Figure 4.20 is an example of a horizontal displacement along the x-axis of the micro-conveyor. However, the system is capable of tracking any random movement of the micro-conveyor. In this example, θ_x has a constant value while the value of θ_y increases. The oblique variation of θ_y is due to the fixed mirror that causes angle deviation between the conveying surface and the MEMS referential plane. Knowing the values of θ_x and θ_y , the micro-conveyor's position can be calculated by applying the homography method.

In a closed loop control system, the micro-conveyor is guided to make a horizontal trajectory moving from point A to point B, see figure 4.19. The corresponding evolution of the x coordinate as a function of time is shown in Fig.4.21



(a)



(b)

Figure 4.20: Variation of (a) θ_x and (b) θ_y as a function of time during scanning and tracking phase

(a). The system continues to send corrected currents I_{x1} , I_{x2} to reach the desired position B . To evaluate the tracking error between the measured value and the desired value at position B , a portion of 300 measurements of Δx was analyzed to extract the average and RMS errors which are equal to $24.2 \mu\text{m}$ and $18.1 \mu\text{m}$, respectively.

In Fig.4.21 (b), a command to make a round-trip trajectory is set to the conveying surface in order to demonstrate the reliability of the system. At time $t = t_0$, the desired x position value is equal to x_B , making the micro-conveyor translate

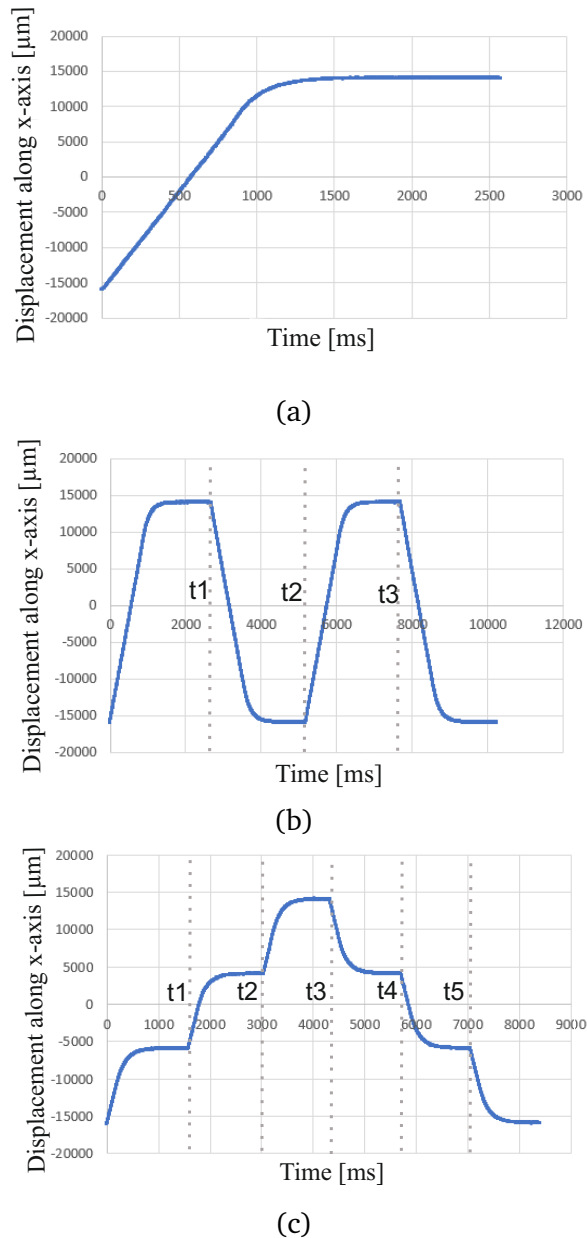


Figure 4.21: Micro-conveyor's position in the x -axis with respect to time for horizontal: (a) step response, (b) round trip trajectory and (c) staircase step response.

towards the right of the surface to position B where it stabilizes. After a certain time, at time $t = t_1$, a new control position value, x_A , is sent so the micro-conveyor returns to the left of the surface, position A . This procedure is repeated at time $t = t_2$ and t_3 .

Figure 4.21 (c), is a stair case step response, where at different times, a new command is sent, guiding the micro-conveyor to make the path (A, O, B, O, A) , leaving and returning to the same position A . The same results can be obtained for the y -axis. The micro-conveyor trajectory in Fig.4.22 (a, b and c) corresponds to (D, C) , (D, C, D, C, D) and (D, O, C, O, C, D) , respectively. For a portion of the final 300 points, the error between the measured and desired value at point D

for example gives an average and root mean square of error equal to $31.4 \mu\text{m}$ and $22.8 \mu\text{m}$, respectively.

As a result, the closed loop tracking is achieved between our proposed developed optical sensor and the conveying surface. The next step is to test and implement the local homography matrix. The micro-conveyor used in the previous experiment cannot move in the cells C1, C3, C7 and C9, due to its large size. For that, a smaller version of the micro-conveyor was developed in order to convey over the entire conveying surface, see figure 4.23. For example, in this experiment, the small micro-conveyor is controlled to follow a square path of $50 \text{ mm} \times 50 \text{ mm}$. The points a, b, c and d are the edges of the square and their coordinates

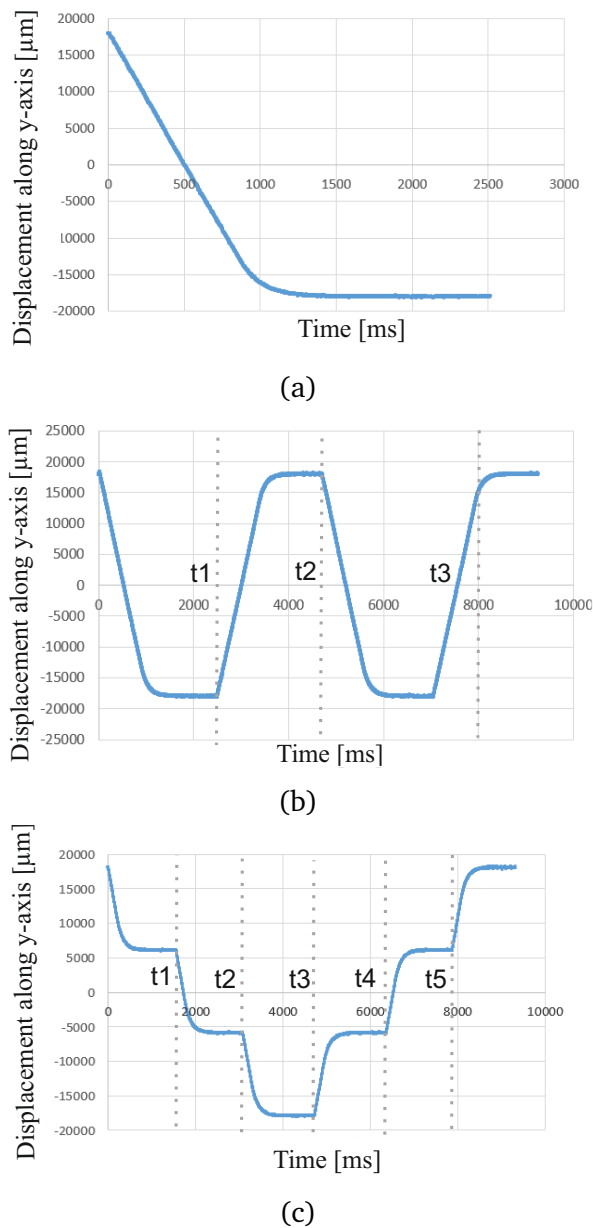


Figure 4.22: Micro-conveyor's position in the y -axis with respect to time for vertical: (a) step response, (b) round trip trajectory and (c) staircase step response

are the desired input of the closed loop control described in figure 4.18.

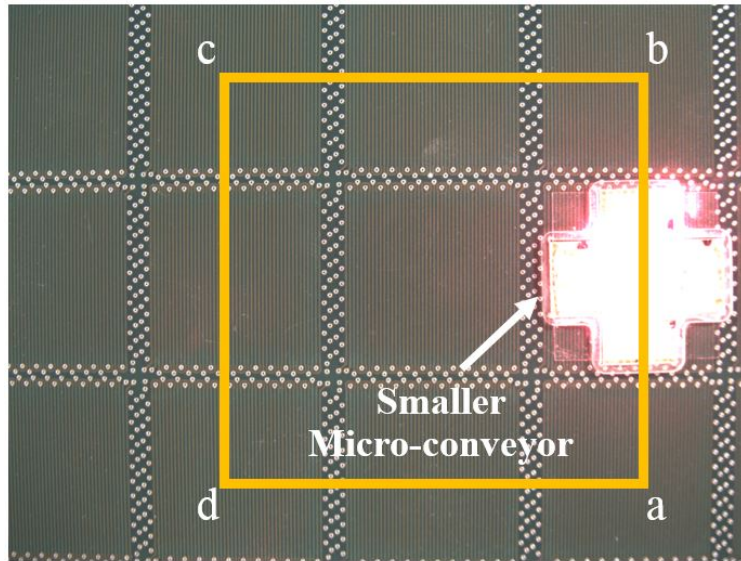


Figure 4.23: Capture of the small micro-conveyor performing the square trajectory

Once the micro-conveyor is localized at position a, the command is to go to position b, then c and d to finally return to the start point position a. Fig. 4.24 (a) illustrates the θ_x as a function of θ_y during scanning and tracking phase. The MEMS mirror rotates first as a spiral pattern, then as a deformed square which is the projection of the desired straight square onto the conveying surface. Fig. 4.24 (b), is the path realized by the micro-conveyor moving from point a and returning to the same start position in a square path. The deformation in the vertical lines of the square path, which are marked with red circles, in the figure 4.24 (b), corresponds to the transition of the micro-conveyor moving from one cell to another. In fact, in the transition zone, there are no integrated coils, resulting in the loss of control of the micro-conveyor. However, as soon as it enters the new cell, the closed loop control system corrects its trajectory. In the horizontal axes, we don't see this deformation because the coils controlling the horizontal movement are in the upper layer, while the vertical direction coils are in the lower layer causing more loss of energy for the vertical displacement. This is a clear demonstration of one of the goals of the closed loop which is to correct the trajectories if the surface is dis-functioning, which has been observed in this case.

As conclusion, such results verify the capability of the system to track and maintain the desired trajectory of the micro-conveyor, using local homography, moving in a 2D plane.

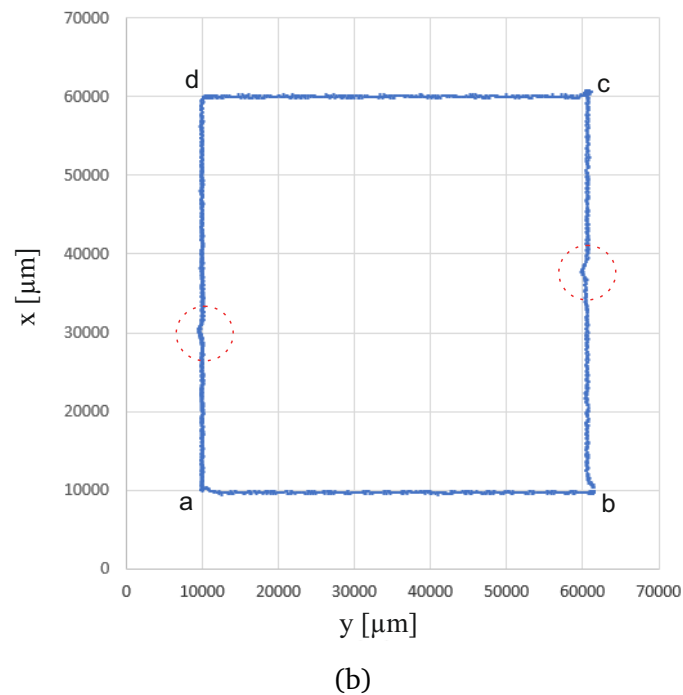
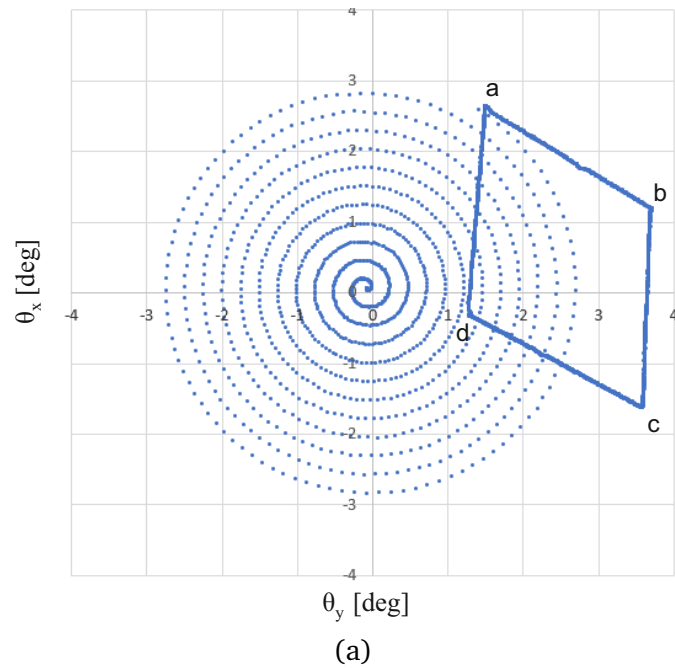


Figure 4.24: (a) θ_x as function of θ_y during the scanning and tracking of the micro-conveyor moving in a (b) square path.

4.6 Multiple micro-conveyors control

This section aims to describe the methodology to localize and track multiple micro-conveyors moving over the smart surface. The first approach to do so is to duplicate the system and to orient each corner cube reflector toward a single MEMS, in this case, there is no interferences in the reflected signals and each micro-conveyor has an independent tracking system and can execute at the same time t , as seen

in figure 4.25. However, this method is expensive, demands larger space and gets more complicated when more than two micro-conveyors are on the surface. Time multiplexing is a more convenient approach which will be discussed and tested further in this section.

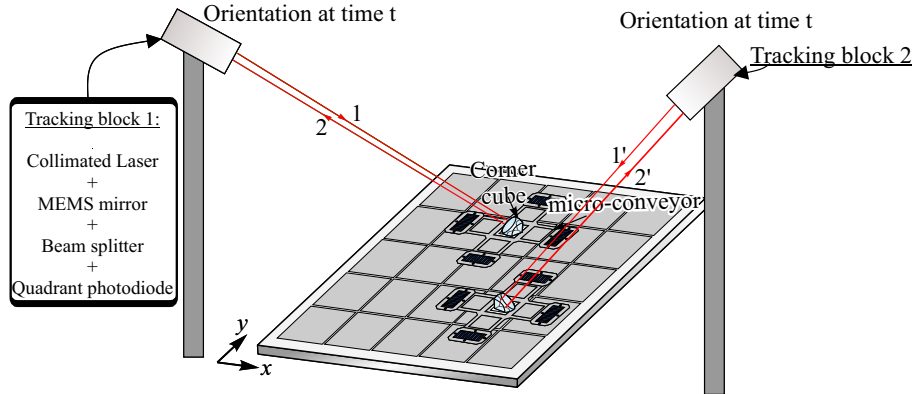


Figure 4.25: Localization of multiple micro-conveyors using duplicate system at time t (without multiplexing)

4.6.1 Time multiplexing method

The principle of time multiplexing is based on the idea of continuously scanning the surface with a spiral pattern, as well as successively switching from one micro-conveyor to another to follow them. The first signal of localization corresponds to the first micro-conveyor and the second signal corresponds to the second micro-conveyor, and so on. The advantage of this technique is that it is less expensive because a single tracking system can be used for multiple micro-conveyors. Figure 4.26 illustrates the time multiplexing concept.

The tracking system localizes the first micro-conveyor at time t , then the system continues scanning until time t' , where the second micro-conveyor is located, and so on.

A block diagram of time multiplexing algorithm for locating two micro-conveyors is presented in figure 4.27.

First the system starts scanning the surface with a spiral pattern, by sending v_x and v_y to the MEMS mirror having the following formulas:

$$v_x = K \times s \cos(k' \times s)$$

$$v_y = Z \times s \cos(Z' \times s)$$

Where K , Z , K' , and Z' are constant and chosen in such a way that the spiral covers the entire conveying surface with the desired pitch. The spiral index varying from

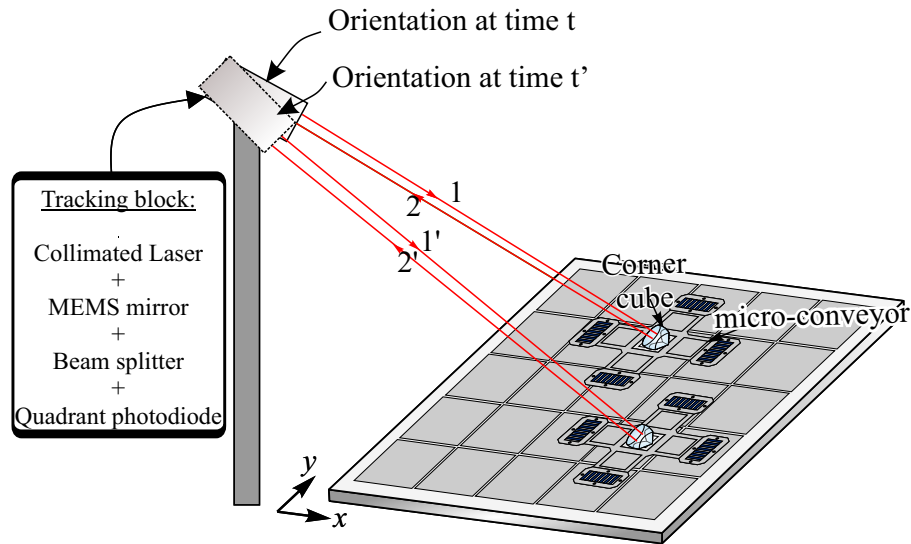


Figure 4.26: Localization and tracking system block diagram at time t and t' (multiplexing)

1 to the total number of points corresponding to one complete round of scanning is named s .

During a single round of the scanning process, each of the two micro conveyors should be localized once. As a result, the spiral scanning must be faster than the speed of movement of the micro-conveyor in order to detect uniquely one position per round for each micro-conveyor. V_{SUM} generated by QPD is still compared to the V_{th} . The system continues incrementing the index s until V_{SUM} exceeds the threshold value. After exceeding the threshold value for the first time, the actual spiral index then would correspond to the position of the first micro-conveyor. After that, the spiral continues scanning by re-incrementing the index s . When V_{SUM} exceeds the threshold value for the second time, the corresponding spiral index will be then assigned for the position of the second micro-conveyor. After this stage, the system starts the second round of scanning by returning to $s = 0$ and starts seeking the second new position of each micro-conveyor, and the process is repeated for each round of scanning. The position of the micro-conveyors can be calculated from the indexes s_1, s_2 , having direct relation with v_x, v_y (i.e θ_x and θ_y of the MEMS mirror) by applying homography transformation between the MEMS referential plane and the micro-conveying surface.

The drawback of time multiplexing is displayed in the case when the progressive sequence of positions of each micro-conveyor throughout every single round is mixed up between that of other micro-conveyors. In other words, there is no ID for each micro conveyor. Thus, such a system can localize the micro-conveyor without extracting its identity (s_1 or s_2). In fact, this method is limited when

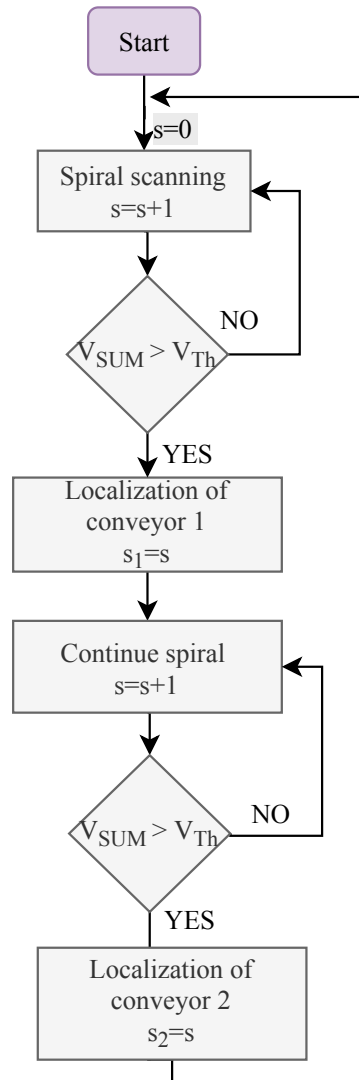


Figure 4.27: Localization and tracking system block diagram

the speed of the micro-conveyors becomes higher than the scanning speed, which prevents knowing between one scan and the next one, if the detected point corresponds to the same micro-conveyor or to the other. However, this approach well fits the goal of preventing collisions between micro-conveyors where the identity and progressive order of positions of the micro-conveyors is irrelevant.

4.6.2 Proof of concept

In this work, the small version of the micro-conveyor is used to test the time multiplexing, in order to have two micro-conveyors moving in parallel over the surface. It is complicated to convey two micro-conveyors of the original version (see fig 4.19), over the $15\text{cm} \times 15\text{cm}$. Figure 4.28 shows the trajectories of two micro-conveyors (small version) while a continuous spiral scan is performed over the surface. The micro-conveyor number 1 is ordered to go through positions 1, 2

and 3, in parallel the micro-conveyor number 2 is moved through positions 1', 2' and 3'. These trajectories must be followed during time multiplexing. By applying the algorithm explained in figure 4.27, the trajectories of each micro-conveyor are reconstructed. The time between one point extraction and another is equal to the time taken by the MEMS to do a new complete spiral scanning over the entire surface, during this time the micro-conveyor moves a distance equal to the velocity of the micro-conveyor multiplied by the time. The calculated coordinates of each micro-conveyors are presented on the front panel of the LabVIEW code as a graph, as shown in figure 4.29. These results confirm the functionality of the time multiplexing method by obtaining the trajectory of the two micro-conveyors.

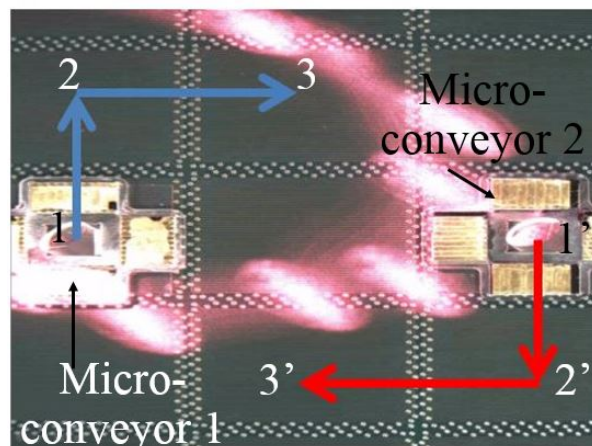


Figure 4.28: Trajectory of two micro-conveyors

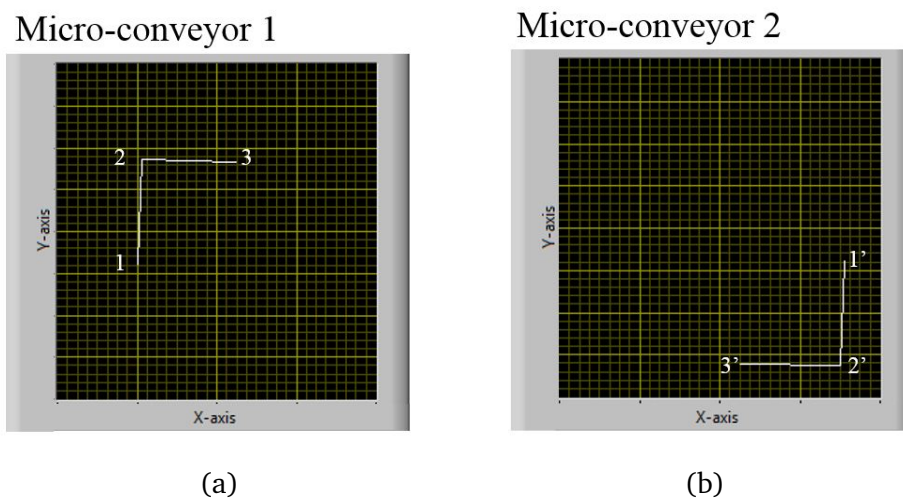


Figure 4.29: Time multiplexing results showing the resulted trajectory of (a) micro-conveyor number 1 and (b) micro-conveyor number 2.

4.7 Conclusion

In this chapter, the closed loop tracking of a mobile micro-conveyor was presented and validated, after calibrating the conveying surface using a Homography matrix H . During the offline process of calibration, n measurements of the conveying surface's coordinates and those of the corresponding parallel plane to the MEMS mirror were collected. The vision system resolution sensitivity of $45 \mu\text{m}/\text{pixel}$ was able to portray the entire field of 3×3 central cells. The values of the rotation angles of the MEMS were used to calculate the corresponding MEMS referenced coordinates. The impact of the measurements on the accuracy of matrix H showed that increasing the number of measurements n to a limit value of $n = 20 \times 20$ improves the error. The distance error average and root mean square values were calculated and were equal to $267.4 \mu\text{m}$ and $159.4 \mu\text{m}/\text{pixel}$, respectively. The local homography process favors improving the distance error through setting 9 matrices having each matrix deployed for the calibration of a single cell. Therefore, the coordinates of the micro-conveyor were calculated by using the matrix H that corresponds to its cell position. The local homography method with a camera resolution of $45 \mu\text{m}/\text{pixel}$ proved to be convenient for the static collection of the needed measurements. After travelling a maximum horizontal distance of 3 cm, 300 measurements were collected for the error in x-axis and the average and root mean square errors of $24.2 \mu\text{m}$ and $18.1 \mu\text{m}$, respectively. The reliability of the system was tested by following a round trip trajectory over the conveying surface. Similarly, 300 measurements in the y-axis were collected to yield in average and root mean square error of $31.4 \mu\text{m}$ and $22.8 \mu\text{m}$, respectively. The reliability test was also verified for the vertical axis. During the local homography test, the tracking system was capable of tracking and correcting the path of a smaller version of the micro-conveyor when crossing a square trajectory of $5\text{cm} \times 5\text{cm}$. The time multiplexing principle was validated for the localization and tracking of micro conveyors.

Chapter 5

Application of the localization and tracking in macro-scale with an active reception system

5.1 Introduction

This chapter is an application in the macro-scale of the optical localization and tracking method proposed in chapter 2. Here, the purpose of the tracking is to ensure high bit-rate wireless optical communication between mobile systems. In fact, the bandwidth and the bit rate are inversely proportional to the surface of an optical detector, thus a fibered detector is implemented in each terminal of the system to transmit the data. As the terminals are mobile and moving in real time at high speed, a tracking module is required to maintain the narrow LOS between the mobile systems, in order to inject light into the optical fiber. Furthermore, the terminal to be tracked acts here as an active receiver that is an essential component of the tracking. In fact, the terminals work together to ensure the tracking, i.e, to maintain the LOS between them.

At present in a meso/micro scale, it is not possible to have an active reception and to embed heavy opto-electronic components. Therefore, this method of an active reception was tested on a macro-scale application. A pan-tilt motor replaced the passive corner cube that was used in the previous chapters. The target can be an actuated drone, a mobile robot or people holding the active receiver. We propose an optical tracking module (OTM) mounted over each terminal in order to maintain the line of sight between them. This chapter first describes the general architecture of the system, introduces the structure of the pan tilt module and discusses the functionalities of each component of the OTM. Experimental work validates the closed-loop control between two terminals by maintaining the same

LOS between them.

5.2 Optical communication system description

The system consists mainly of two modules that will interact with each other and align to enable optical data transfer. The first element is called the fixed pan-tilt terminal (FPT) which is mounted on a fixed platform, e.g., the ceiling, see figure 5.1. This FPT consists of the mechanical systems including drive unit (i.e., pan-tilt module (PTM), optical tracking module (OTM) and embedded electronic circuitry (to control/pilot these mechanical systems). In a relative coordinates frame of reference, the FPT has a fixed origin. The second communicating system is called the mobile pan-tilt terminal (MPT). In a relative coordinates frame of reference, the origin of the MPT can move in three dimensional space. The design of the MPT is exact replica of the FPT with additional mobility characteristics. In 3D space, if exact alignment is achieved, the tilt-angles of the FPT (α_f) and

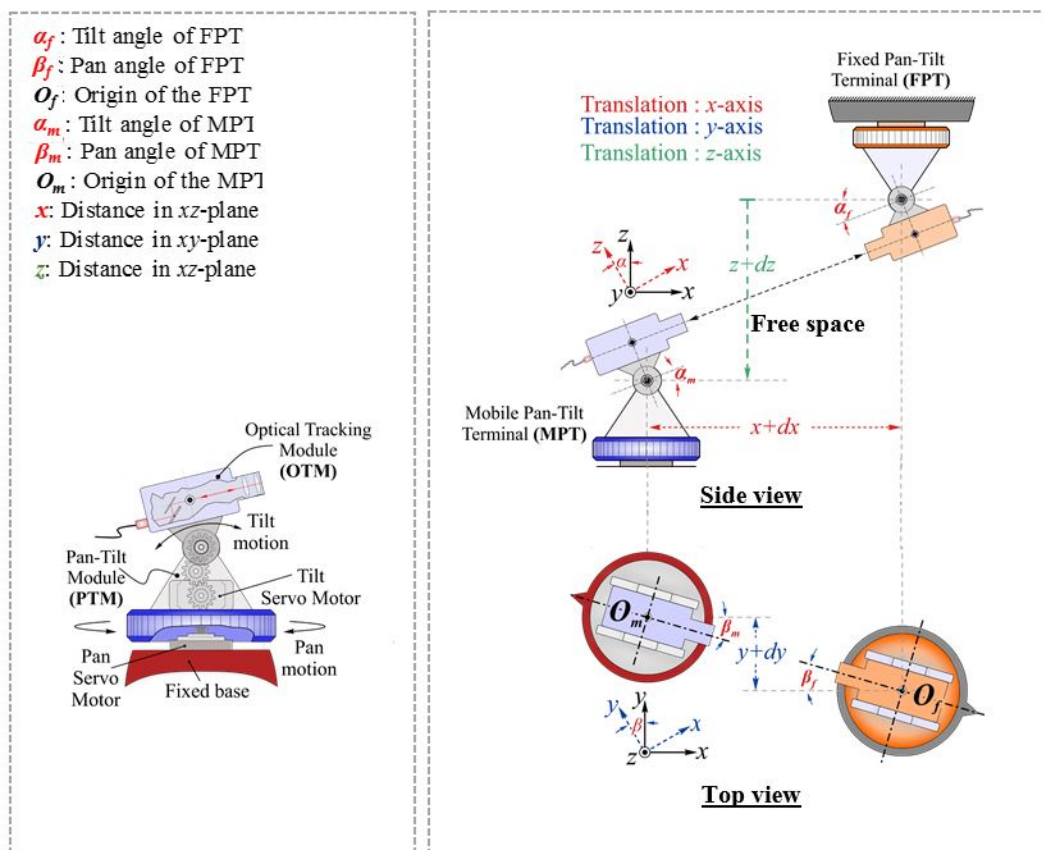


Figure 5.1: Generalized approach for the system

the MPT (α_m) will be identical. Likewise the pan-angles of the two systems will be equal, i.e $\beta_m \approx \beta_f$. These angles in practice are achieved with the help of two servomotors, each is dedicated to one angle. The principle of the proposed optical communication system is based on the use of the same laser beam as both

a communication signal and an angular alignment signal. For this purpose, a part of the incoming optical signal is used for the angular alignment between the two terminals, and then processed by Quadrant Photodiodes (QPDs) integrated onto the OTM. For instance, the QPDs of the MPT are used in such a way to extract the translation and angular information of the incident light ray coming from the FPT. As a result, from this extracted information, in a closed loop control system, the MPT corrects its orientation in order to maintain the LOS with the new position of the FPT. And vice versa.

5.3 Pan-Tilt module (PTM) structure

The PTM design is based on the SPT200H module from ServoCity Corporation (see Fig. 5.2 (b)), [SPT2]. We selected this PTM design because the tilt and pan servomotors rotation axes are collinear with respect to the pan servomotor. The advantage of this collinear axis of the pan and tilt motors is that the load distribution is along a single axis. This eliminates the inconvenience of torque generation due to the lengths of the mechanical support elements during motion. In addition, during motion, the friction forces due to the both servomotors shaft rotations are reduced by integrating bearing supports (i.e., roller bearing). This results in smooth pan and tilt rotatory motion. The aforementioned characteristics of this mechanical design lead to better resolution in pan and tilt positioning. In

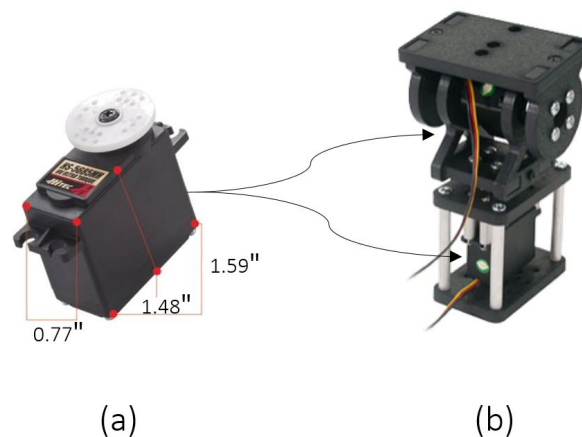


Figure 5.2: (a) Servomotor (b) pan tilt module

the PTM design, the drive elements to generate the pan and tilt angles are the servomotors. Two DC servomotor HS-5685MH [HS 5] were selected to generate both pan and tilt angles (see Fig. 5.2 (a)) by sending an electrical pulse width modulated signal (PWM), through the control wire. The HS-5685MH is a high torque, high voltage and metal gear digital sport servomotor.

5.4 Optical tracking module (OTM) description

The OTM module consists of two main blocks that are called telescope block and MEMS block in order to guide the entry laser beam towards the attached fiber optic cable, as shown in figure 5.3.

The telescope block is dedicated towards controlling the pan-tilt unit, thus delivering coarse positioning. It integrates two Quadrant photodiodes (QPD₁ and QPD₂), an entry lens (L₁) and two beam splitters (BS₁, BS₂). These two QPDs are used to extract angular and translation information with respect to the incident light beam at L₁. The two beam splitters are identical and used with QPD₁ and QPD₂.

The second block is called the MEMS block. This block is dedicated to fine-tuning by directing the incoming laser beam at Lens (L₂) onto the center of the fiber optic cable core mounted on the fiber mount (PF). This block includes three lenses (L₂, L₃, and L₄), a beam splitter (BS₃), a Quadrant photodiode (QPD₃), a fiber mount (PF) and a MEMS mirror for beam steering. An FC/PC Fiber adapter is used as a fiber mount (PF), in order to connect the fiber cable to the MEMS block. Lens L₂ is used to focus the light onto the MEMS mirror, L₄ is used for QPD₃ and L₃ is used to focus the light at the center of the fiber mount. The subassembly of the BS₃, L₄ and QPD₃ is used to detect the alignment of the laser light reflected from the MEMS mirror to steer the beam into the fiber mount at PF.

In addition, the OTM design prototype includes four compact dovetail linear stages for XYZ manipulations. Three of these stages are used to calibrate three QPDs and one is installed for PF to align the fiber mount in front of L₃. The three QPDs are identical and are the same as the one used in the previous chapters (i.e., QP50-6-TO8 purchased from First Sensor).

The description provided in Fig. 5.3, is merely the schematic arrangement of the optical elements in the OTM design using top view. The geometrical parameters between the central axis of each optical element of the OTM are marked as a_0, a_1, \dots, a_{11} and they will be defined according to the focal distance of selected lenses.

5.5 Optical ray propagation model

As shown in figure 5.4, which represents light ray distribution model, the incident light beam, coming from the second OTM, enters through lens (L₁). Due the optical characteristics of the beam splitter (BS₁) used in the telescope block, a 10% portion of the light beam is reflected onto the first QPD (i.e., denoted as QPD₁). The rest of the light (i.e., 90%) is transmitted towards beam splitter 2. Similar in optical characteristics, a portion (i.e., 10%) of the incident beam on BS₂

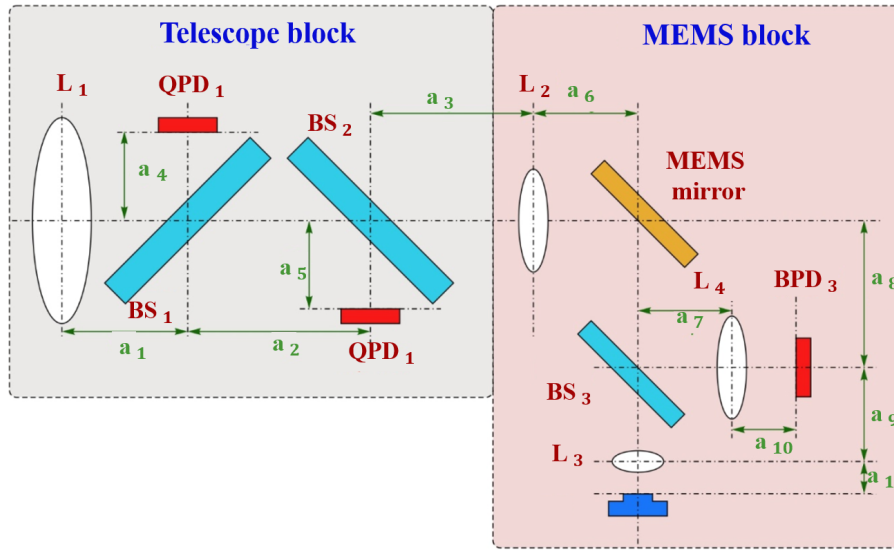


Figure 5.3: Schematic layout of the different components of the OTM

is reflected onto the second QPD (denoted as QPD_2). The rest of the incident beam is transmitted towards lens (L_2). L_2 focuses the light beam towards the surface of the mirror, which in its turn, reflects the light to BS_3 . 10% of this beam is received by QPD_3 . The rest of the light power, i. e. 90%, corresponds to the useful optical power for data transmission that will be injected into the optical fiber.

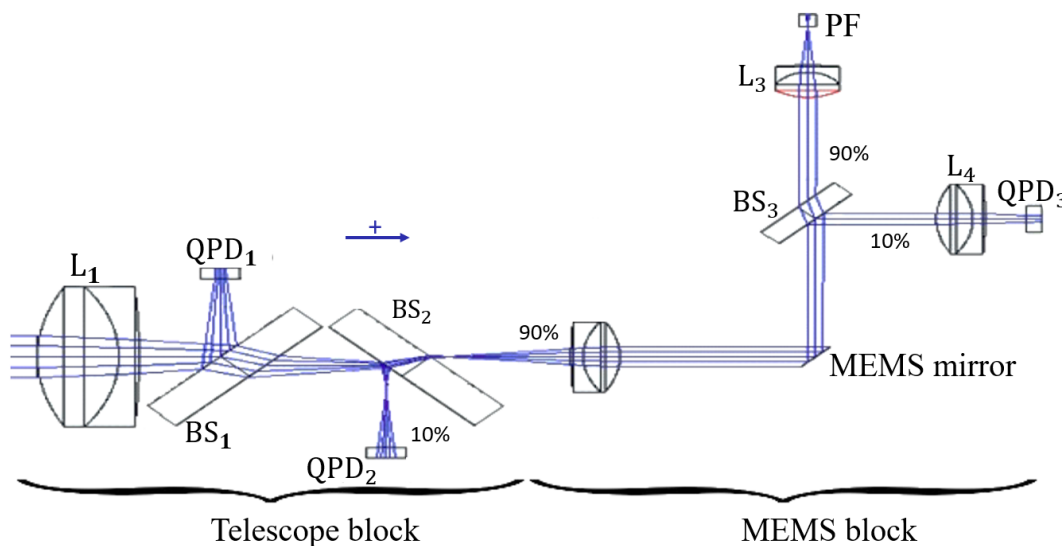


Figure 5.4: Schematic of the Zemax ray distribution model of the OTM

The division of the OTM into two blocks is necessary to design and validate both blocks individually and then collectively. The telescope block will be presented first, then the MEMS block.

5.6 Telescope block of the OTM

In this section the telescope block of the OTM design will be separately presented and validated using the pan-tilt servo motor system.

5.6.1 Modeling of the optical path and geometric equations

The path of the incident beam towards two QPDs is described in Fig. 5.5. For the purpose of simplification, the two beam splitters are not shown in this figure. The main reason why we need to use two QPDs is that two parameters have to be tuned to obtain a perfect alignment of the OTM with the incident beam. The first parameter denoted by T corresponds to the position of the centroid of the incoming beam relative to the center of the input lens of the OTM (L_1). This T value must be set near to zero, which means that the incoming center ray enters at the center of L_1 , thus maximizing the optical link power budget. The second parameter denoted by θ is related to the angle between the incident beam and the optical axis of L_1 . This second parameter must also be near to zero, which means that the incoming ray must be parallel to the optical axis of the OTM. This also contributes to maximize the optical link power budget, with the help of a dynamic angular correction performed at the emitter/receiver module. The T and θ parameters are illustrated in Fig. 5.5, where the translation T value is equivalent to the distance between the optical center of L_1 (notated O_1) and the projection point coordinates of the ray coming from the other OTM (named O_{2p}), and θ the angle between the direction of the OTM's axis and the incident beam. When the translation T and rotation θ are equal to zero, the optical spot is centered on both QPDs. That will indicate that the OTMs are facing each other.

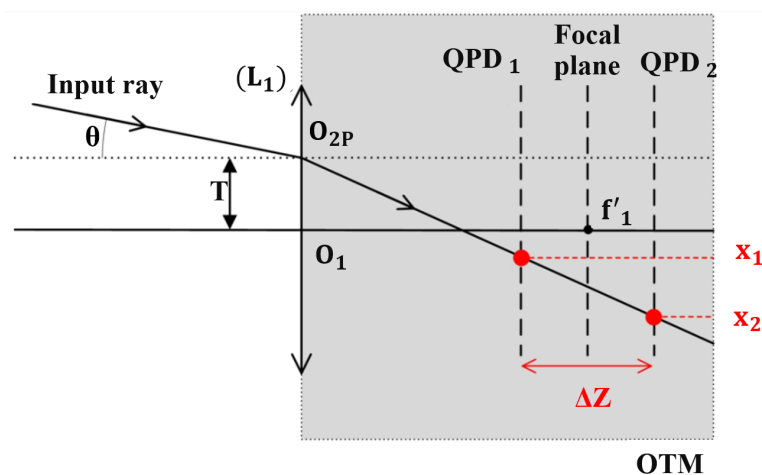


Figure 5.5: Schematic description of the ray propagation from the input lens to the two QPDs.

If a single QPD is placed in the vicinity of the back focal plane of lens L_1 , as

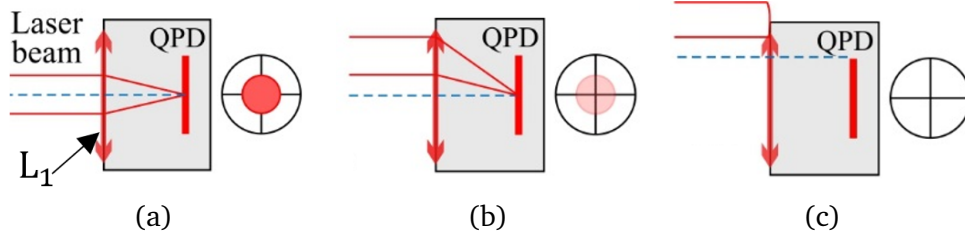


Figure 5.6: Incident laser beam misalignment effect on the QPD with (a) centered beam, (b) vertically shifted and (c) vertically shifted and outside.

seen in figure 5.6, the device will provide individual voltages proportional to θ (in both directions). However, a shift on the T parameter would not be detected: a translation of the incident laser beam has no effect on the position of the spot on the QPD, and thus is not detected. Figure 5.6 (a) represents the case where the incident beam is centralized and the translation T is equal to zero. By translating the laser beam, i.e. increasing the T value, the QPD cannot detect or extract this T variation since the spot light on its surface has remained in the center 5.6 (b). The intensity of the received optical power decreases until extinction, when the incident beam no longer reaches the active surface QPD, see Fig. 5.6 (c)).

Thus, the proposed solution consists in placing two QPDs on each side of the focal point of the first lens, in such a way that both translation and angular informations of the PTM can be extracted from the incident light beam. The distance between lens L_1 and the first QPD is $f'_1 - \frac{\Delta Z}{2}$, the distance between L_1 and the second QPD is $f'_1 + \frac{\Delta Z}{2}$, where f_1 is the focal of lens 1, ΔZ is defined to ensure that the diameter of the beam incident on the QPDs is equal to the radius of the QPD. The θ angle and T translation are estimated using the following formulas:

$$\theta_x = \arctan \left(\frac{1}{f'_1} \cdot \frac{x_2 + x_1}{2} \right) \quad (5.1)$$

$$\theta_y = \arctan \left(\frac{1}{f'_1} \cdot \frac{y_2 + y_1}{2} \right) \quad (5.2)$$

$$T_x = \frac{x_2 + x_1}{2} + f'_1 \cdot \frac{x_2 - x_1}{\Delta Z} \quad (5.3)$$

$$T_y = \frac{y_2 + y_1}{2} + f'_1 \cdot \frac{y_2 - y_1}{\Delta Z} \quad (5.4)$$

Where θ_x , θ_y , T_x and T_y are the incident beam angles and translations in xy -plane, respectively, and x_1 , y_1 , x_2 and y_2 denote the positions of the light spots focused onto the QPD₁ and QPD₂ respectively. The next section will be dedicated to simplify the previous equations of the angular dependence of the QPD output voltages.

5.6.2 Simplified calculation of θ and T from the QPD voltages

If we consider that, the angles (i.e., θ_x and θ_y) are small, for both angles $\tan(\theta) = \theta$, we can re-write the above equation in following manner:

$$\theta_x = \frac{1}{f'_1} \cdot \frac{x_2 + x_1}{2} \quad (5.5)$$

$$\theta_y = \frac{1}{f'_1} \cdot \frac{y_2 + y_1}{2} \quad (5.6)$$

The first QPD measures two differential voltages ($V_{(B-T)1}$, $V_{(L-R)1}$) that can be considered proportional to the distances (x_1 , y_1). V_{B-T} and V_{L-R} are the generated output signals, see section 3.4.1 for more details. Similarly, the second QPD measures two differential voltages ($V_{(B-T)2}$, $V_{(L-R)2}$) that can be considered proportional to the distances (x_2 , y_2). Therefore, we can consider that:

$$\begin{aligned} \theta_x &\propto (V_{(B-T)2} + V_{(B-T)1}) \\ \theta_y &\propto (V_{(L-R)2} + V_{(L-R)1}) \end{aligned} \quad (5.7)$$

Where \propto symbol indicates proportionality. Thus, θ can be estimated directly from the voltage values measured through both QPDs by adding them together.

To further simplify the estimation of T_x and T_y , we can consider at first that the OTM has turned to the incident ray and therefore the angle θ has become zero. Taking this assumption, we consider that the servo will first seek to cancel the value of θ , and then it will seek to cancel the value of T_x and T_y . Consequently, if we consider that $\theta \simeq 0$, we can simplify the calculation of T_x and T_y from equation 5.3 and 5.4:

$$T_x = f'_1 \cdot \frac{x_2 - x_1}{\Delta Z} \quad (5.8)$$

$$T_y = f'_1 \cdot \frac{y_2 - y_1}{\Delta Z} \quad (5.9)$$

In a similar fashion, the above reasoning is carried out to determine θ_x and θ_y . We can consider that:

$$\begin{aligned} T_x &\propto (V_{(B-T)2} - V_{(B-T)1}) \\ T_y &\propto (V_{(L-R)2} - V_{(L-R)1}) \end{aligned} \quad (5.10)$$

In this case, T can be estimated directly from the voltage values recovered by the QPDs by subtracting their measured values. Once these estimations on the θ angle and T translation are done, they are injected into the control part of the system in order to maintain them close to zero by moving the servomotors.

5.6.3 Telescope control unit

The general description of the control model is provided in Fig. 5.7. The model contains six main blocks. The comparator block delivers a difference between desired input and model output. The error in position estimation of the Pan-Tilt is passed to the controller block.

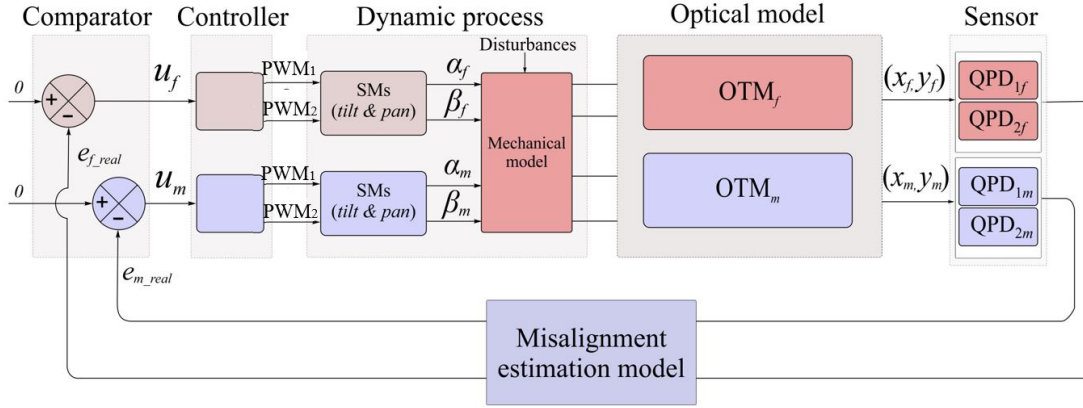


Figure 5.7: Control block diagram.

The controller block generates controlled voltage signals, PWM_1 and PWM_2 , corresponding to the desired pan and tilt angles. The angles generated by the servomotors (SMs) are passed to the mechanical block. The rotation angles are used by the mechanical model to locate the center and direction of the OTM in three dimensional space. The optical model consists of an Optical Ray Projection (ORP) model and an optical tracking function. With the help of this function, the projection point on the entry point of the OTM is located and passed to the QPD for detection. The coordinate (x, y, z) of the OTM's center is measured by the QPD model. Two QPD blocks for each PT have been used to detect angular and translational movements. The coordinate (x, y, z) delivered by the OTM to the QPD model is converted into a voltage and passed to the PT misalignment estimation model. This model's output is used to compare the input value as shown in Fig. 5.7.

In order to develop the control unit, a hybrid approach is adopted, as presented in Fig. 5.8. The voltage output signals V_{SUM} , V_{B-T} and V_{L-R} of the QPD₁ and QPD₂ are acquired using a USB NI 6009 DAQ module. Where V_{SUM} , as mentioned in 3.4.1, is equal to the summation of the four voltages generated by each quadrant of the QPD.

The main reason behind using the NI DAQ approach is to acquire QPD signals that ranges from $-5V$ to $+5V$. This range introduces limitations as PIC explorer/PIC32 module only accepts $0-3.3V$ analog voltages. Therefore, the conversion from analog $+/- 5V$ to analog $0 - 3.3V$ is performed in LabVIEW. More-

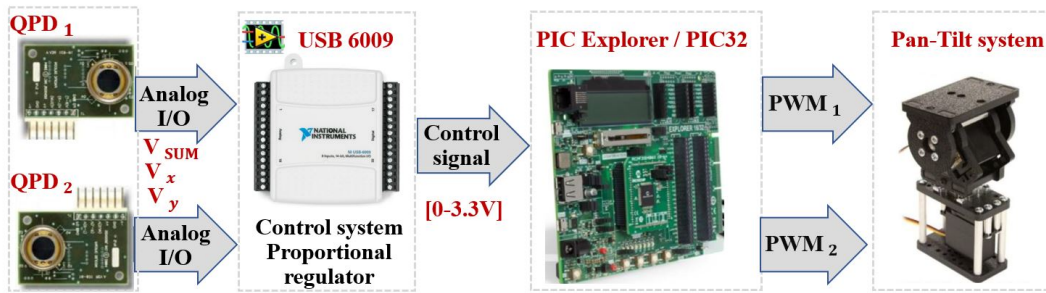


Figure 5.8: Block diagram of the connection layout of the hybrid control approach

over, a proportional control is developed in LabVIEW code to reduce the error between desired and measured angular values. It generates two control signals via USB6009 DAQ to the PIC32. As a result, the PIC32 generates appropriate PWM signals (i.e. PWM_1 and PWM_2) to drive the Pan-Tilt servomotors.

5.6.4 Experimental setup of the telescope block

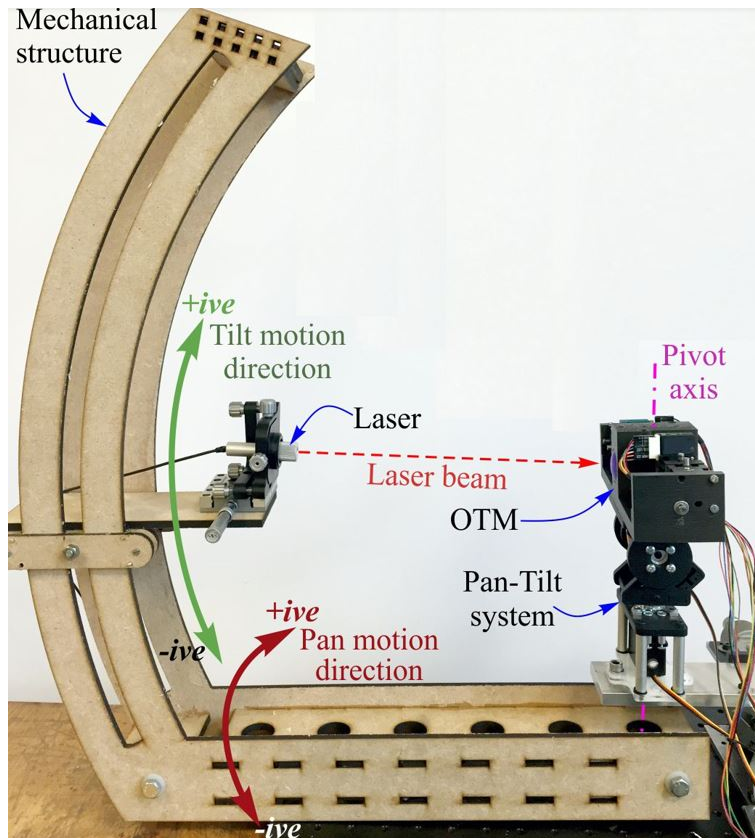
The telescope block of the OTM₁, from Fig. 5.1, was built and mounted onto a PT system, as shown in Fig. 5.9 (b).

To simplify the procedure, the mobile OTM₂ was replaced with a collimated laser source mounted over a mechanical structure capable of performing the required Pan and Tilt motions about the pivot axis of the PT system (Fig. 5.9 (a)).

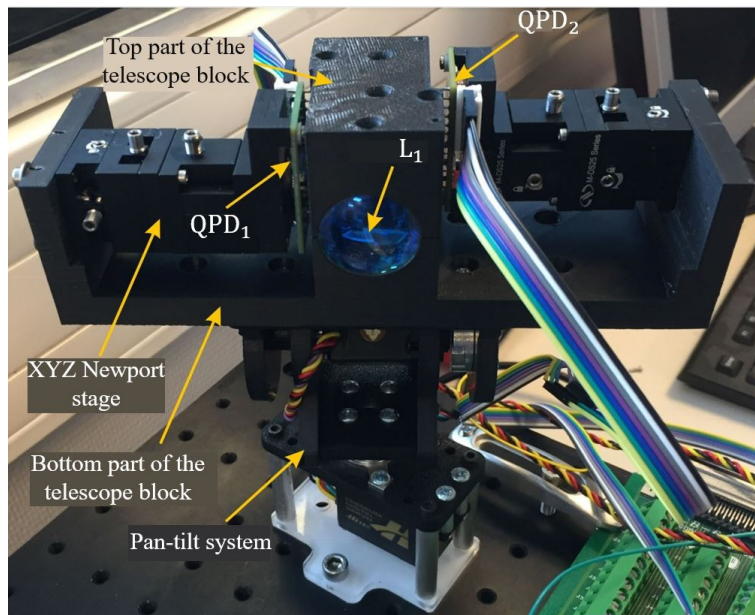
The objective of this experimental setup is to manually mimic the behavior of the mobile OTM₂ with the help of a laser source. As a consequence to the angular movement of the laser source in free space, the fixed telescope of OTM₁ will correct its angular position in order to align itself. Moreover, in a pre-step phase, the laser beam source and the telescope block are optically aligned relative to each other in order to calibrate the QPD₁ and QPD₂. During the calibration procedure, the two QPDs are centered with respect to the input laser beam using a XYZ Newport stage (see Fig. 5.9 (b)) by centering the output voltages acquired by QPD₁ and QPD₂, respectively. Afterwards the system is ready to be tested.

5.6.5 Experimental results of the telescope block

The tracking of telescope block of OTM₁ using a mobile laser is performed by manually moving the source in positive and negative pan directions. Fig. 5.10 represents the output voltages for one of the two QPDs during the tracking phase. The experiment begins by launching the tracking system with the laser being in front of the telescope block (see Fig. 5.9). Thus, the detector generates a significant value of V_{SUM} greater than a threshold value (V_{th}) and values of V_{B-T} and V_{L-R} are close to ε_0 . The values of V_{th} and ε_0 are chosen experimentally and, in this work, were equal to 2 V and 0.7 V, respectively. From $t = t_1$, the laser is



(a)



(b)

Figure 5.9: (a) Experimental setup with (b) enhanced view of the Telescope block mounted onto the pan-tilt system.

moved along the positive pan motion direction, causing a decrease in the value of V_{L-R} , which is greater than the absolute value of $|\epsilon_0|$, see figure 5.11 (a). By consequence, in a closed loop control system, the pan servomotor rotates in order to

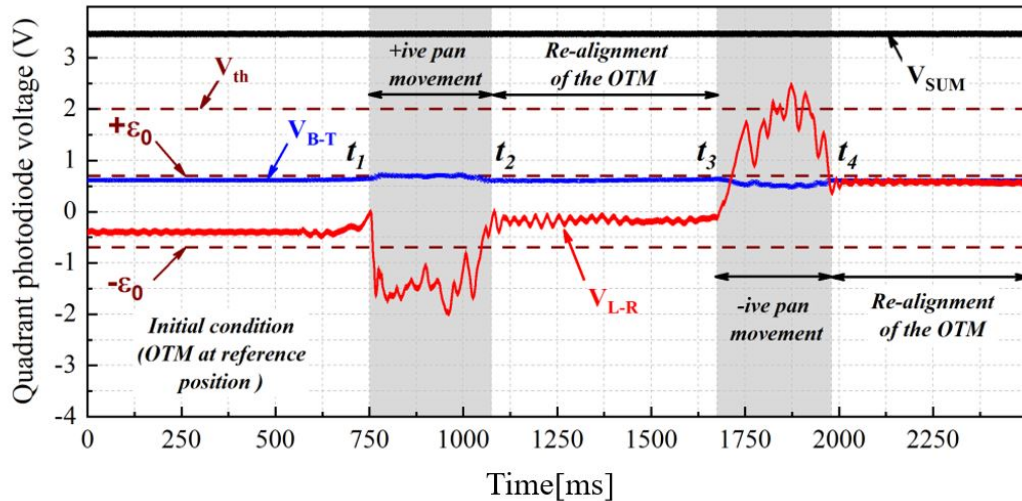
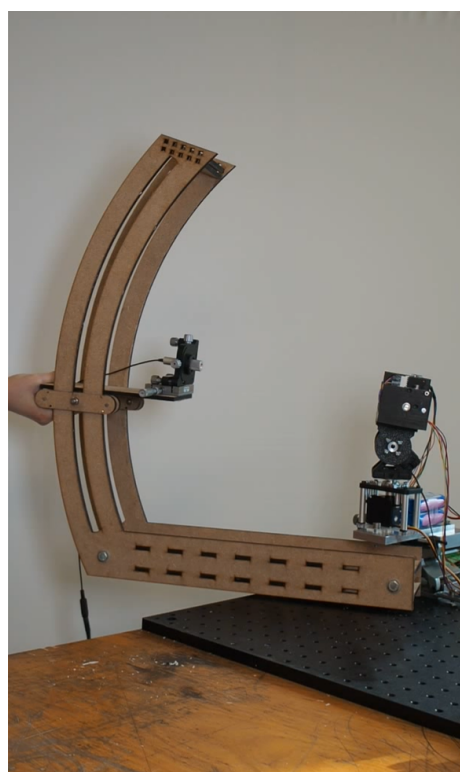
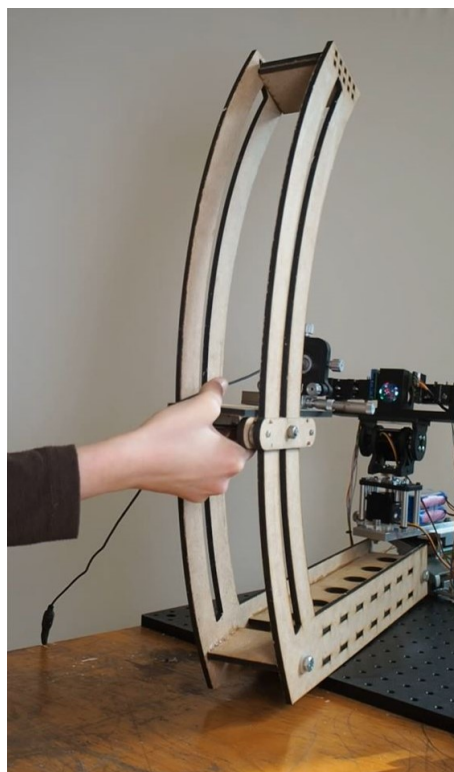


Figure 5.10: Output voltages of the quadrant photo-detector.

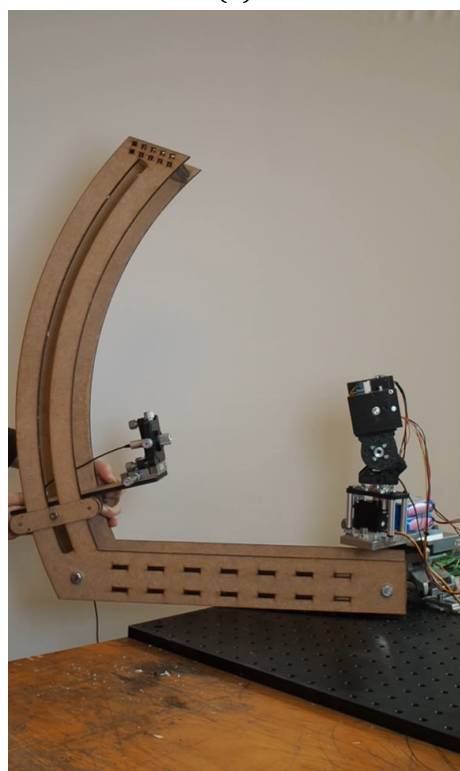
make the telescope block follow the laser displacement, to return the V_{L-R} value less than $|\epsilon_0|$. The time taken by the system to realign the telescope block with the laser source is $t_2 - t_1$. This value depends on the proportional controller used, which can be improved by using a PID controller. After a certain time, at $t = t_3$, another test was realized, where the laser turned in the negative pan motion direction, see figure 5.11 (b). By consequence, the generated V_{L-R} value increased to be greater than ϵ_0 . As shown in Fig. 5.10, at time $t = t_4$, the tracking system was able to correct this elevation by returning V_{L-R} to the desired range of values $[-\epsilon_0, +\epsilon_0]$. In the negative and positive pan movement, the variation of V_{B-T} value did not exceed the ϵ_0 value, thus the tilt servomotor didn't rotate and the telescope's tilting angle remained constant. The same interpretation can be obtained for the telescope block following the movement of the laser source, in the positive and negative tilt directions in order to maintain the LOS between them. In such a scenario, the V_{B-T} value will be corrected in a closed loop control with the tilt servomotor. By consequence, every movement of the laser, regardless of its direction can be detected by monitoring the QPD's output voltages, to be next followed by the telescope block. Figure 5.11 (c and d), represents two different positions of a coupled movement of the laser source, where the Pan-Tilt module continues to follow the laser to maintain the LOS between them. As a result, the telescope block of the OTM has been validated and has demonstrated its capacity to track the laser source that replaces the OTM₂, i.e, two telescope blocks of OTM₁ and OTM₂, respectively, are capable of maintaining the LOS between them when in motion. Next step is to validate and test the MEMS block of the OTM.



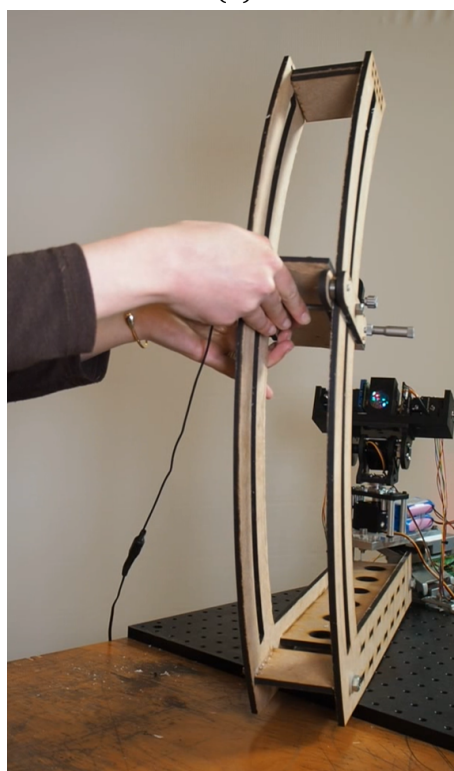
(a)



(b)



(c)



(d)

Figure 5.11: Four different positions of the pan-tilt system following the movement of the laser source

5.7 MEMS block of the OTM

A complete OTM design including telescope block and MEMS block as single platform is presented in this section. The design is 145 mm \times 160 mm \times 56 mm in dimensions holding all the needed optical elements. However, the main objective of this section is to validate the functionality of the MEMS block by injecting the received light beam entering the OTM into the fiber optic with minimal power loss. The MEMS mirror and its driver (the picoamp) are the same as those used in the previous chapters 3 and 4. In addition, the closed-loop control between QPD₃, see figure 5.4 and the MEMS mirror has the same principle as described in chapter 3. In this chapter, it is applied to another type of application.

5.7.1 Experimental prototype

After assembly of all optical and mechanical elements, the final OTM prototype is as shown in Fig. 5.12. This structure is duplicated in order to build a communicating system with two OTM modules.

Figure 5.13 is a capture of the experimental setup composed of two OTM modules placed in an L shape configuration, an intermediate fixed mirror, a fixed laser source, two lenses (L', L'') and a diaphragm. In this setup the OTM MEMS block will be validated separately from the telescope block by manually generating the angular and translation error. Each OTM system is fixed onto a Newport rotation stage to rotate it around its relation axis passing through lens L₁ (see Fig.5.13). Furthermore, to mimic the translation displacement a Newport translation stage is fixed beneath the rotational stage.

OTM₁ acts as an emitter when its optical fiber is injected by a light beam that will be directed towards the second OTM. To test the reception, the optical fiber of OTM₂ was connected to a photometer to measure the received light intensity. In the static phase, the systems are aligned and have the same LOS, giving a maximum power intensity measured at the receiver. The challenge is to maintain the LOS and the maximum power injection in the optical fiber, during motion of one of the OTMs, which is ensured by tracking phase. As mentioned before, large movements are corrected by the telescope block of the OTM in a closed loop with the servomotors, and small variations that the latter cannot correct due to servomotors resolution limitations are corrected by the MEMS block. The aim of this experimentation is to test the MEMS block of the OTM₂ in the case of small angular and translation motion with respect to the OTM₁. The reciprocal is also true, since the two OTMs are identical, i.e. OTM₂ can be the fixed transmitter and OTM₁ the mobile receiver whose MEMS block needs to be tested.

The calibration of the system is a mandatory pre-step in order to achieve, in the

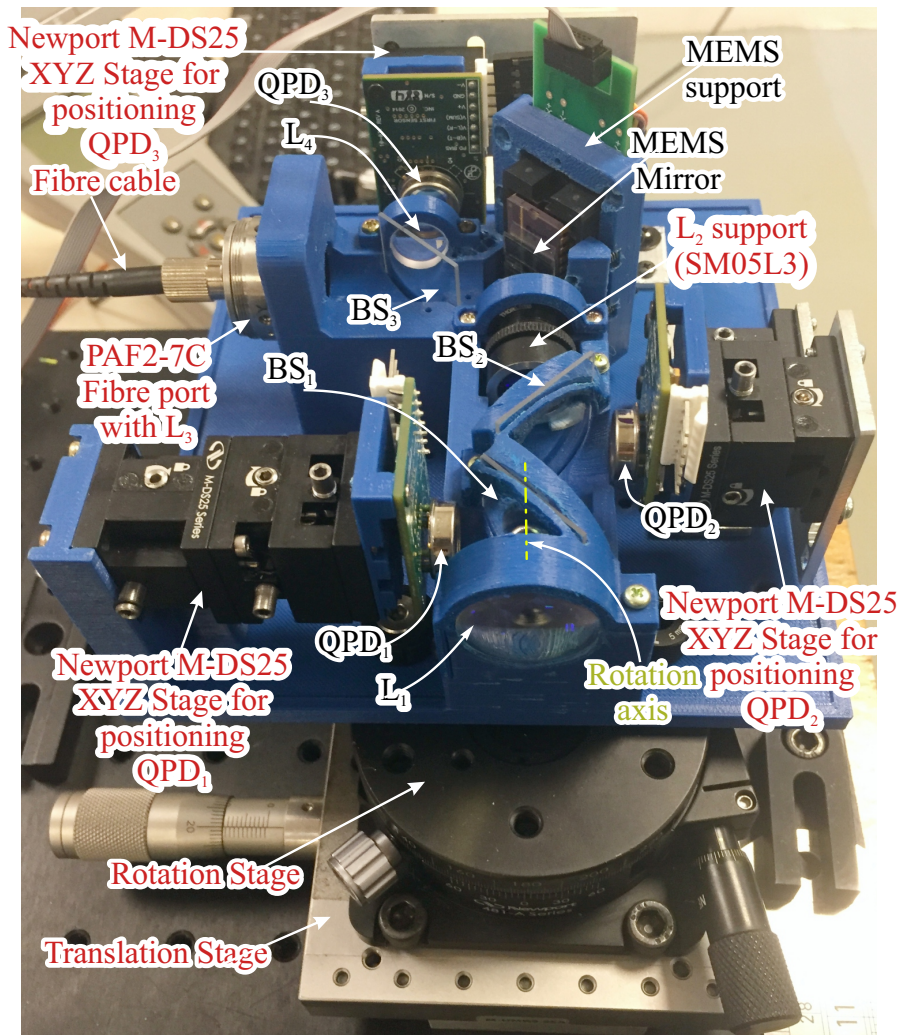


Figure 5.12: Real view of the assembled OTM design for experimental validation.

static phase, the best injection of the laser beam into the fiber located at PAF2-7C fiber port [PAF2]. The calibration is carried out in two phases. First, the fixed laser source, the lenses (L' and L'') and the diaphragm are aligned in front of OTM_1 for it to be calibrated. In this phase, the fixed mirror shown in figure 5.13 is not yet implemented. The position of the QPD_3 of the OTM_1 is adjusted to centralize the incident beam of the laser source on its active surface. This is achieved using a Newport M-DS25 XYZ stage, when $\|V_{(B-T)_1}\|$ and $\|V_{(L-R)_1}\|$ are less than ϵ_0 . The focal lengths of the L' and L'' lenses are chosen to obtain the desired incident beam width of 8 mm. This value is calculated according to the optical and opto-electronic components used in the OTM. The next phase is to calibrate the second OTM. The fixed mirror is placed between the two OTM at an angle of 45 deg. Then, the optical fiber of the OTM_1 is injected with a beam light source that is transmitted to the OTM_2 through the fixed mirror. Again, the position of the QPD_3 of the OTM_2 is adjusted to center the beam on its active surface. In this way, the

two OTMs are calibrated and experimental tests can be performed to evaluate the performance of the MEMS block.

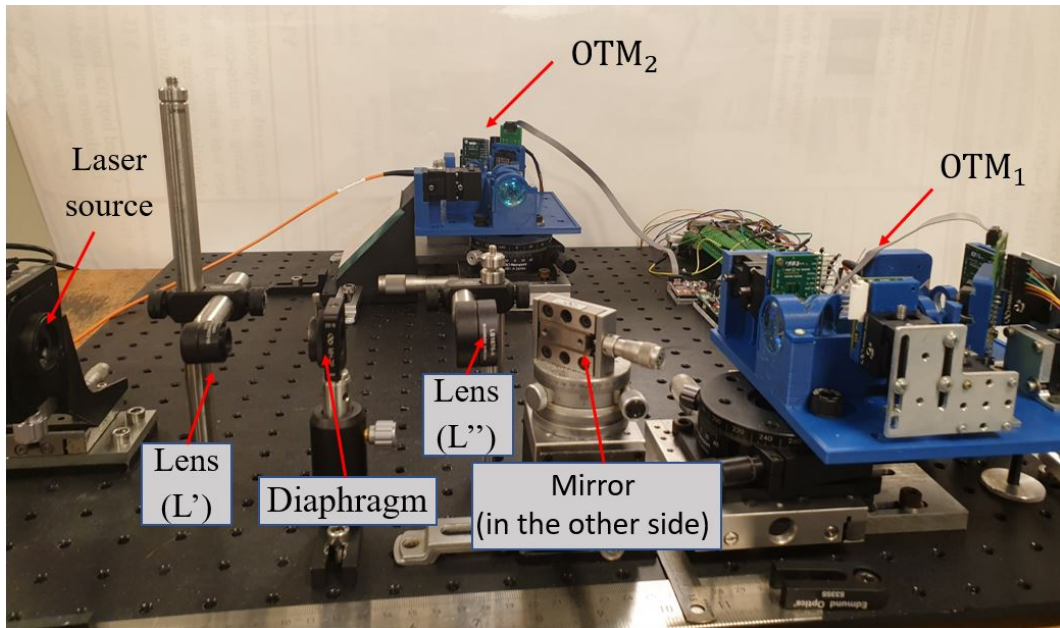


Figure 5.13: Experimental setup of two OTMs.

5.7.2 Results of optical fiber injection during rotation and translation

In the first setup, we considered OTM₁ as the static emitter and OTM₂ as the mobile receiver. The layout presented in Fig.5.14, is the pictorial view of the OTM acting as a mobile receiver (OTM₂). The light entering the center of module comes from OTM₁. The whole OTM₂ platform is manually translated and rotated

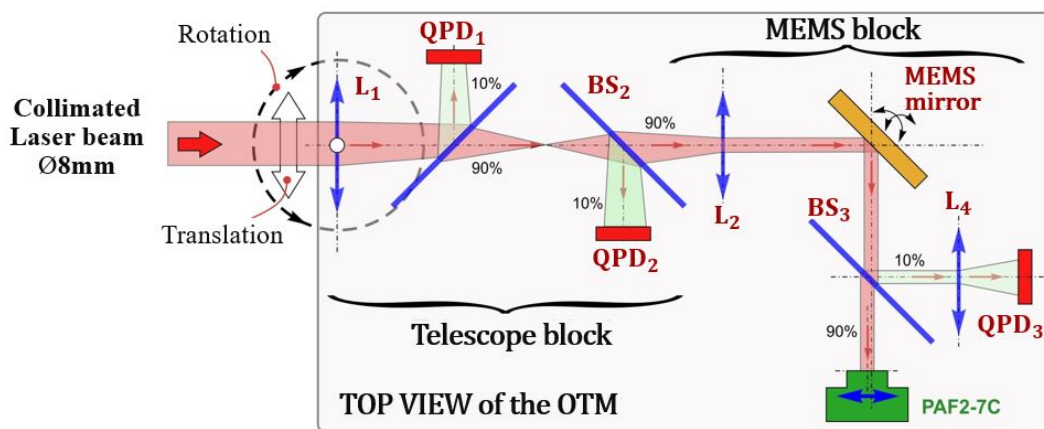


Figure 5.14: Pictorial view of the incident laser beam and rotation and translation of the OTM.

around L1. As a result, the incident collimated laser beam with a spot diameter of around 8 mm arriving from OTM₁ will angularly shift along the optical axis of the telescope block. By consequence, QPD₃, in the MEMS block, will observe this change and provide feed-back to the MEMS mirror control driver to orientate the MEMS mirror to correct this angular error to center the laser beam at the center of QPD₃ as well as fiber port (i.e., PAF2-7C). The angular and displacement variation of OTM₂ are tested simultaneously. Starting with the angular movement, figure 5.15 represents the variation of power loss measured in dB at the fiber mount (PF) of the OTM₂, with respect to the rotational angular variation of the entire OTM₂, as derived from the use of the Newport rotation stage. The experiment began with a 0 deg position corresponding to the initial static position of the OTM₂, giving the best power loss of -6.36 ± 0.02 dB. Then, the angular stage is manually rotated in the positive direction with steps of +0.2 deg. The system shows its stability by maintaining power loss close to -6.36 dB. Then, the steps are increased to +1 deg, to save more time in the execution of the experiment, where the zone of interest are for the angles close to zero. Larger angle values should be corrected by the telescope module. At an angle +6 deg, the power loss

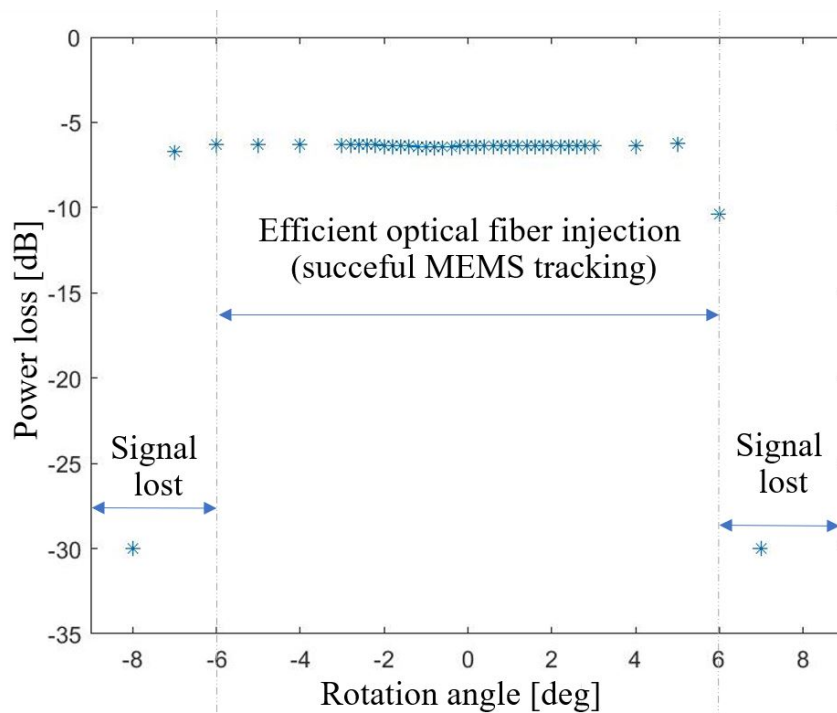


Figure 5.15: Measured output power loss in dB with respect to the angular rotation.

becomes greater than -30 dB, which means that the signal is lost and there is no longer any light injected into the optical fibered. This procedure is repeated for the negative direction of rotation, with initial steps of -0.2 deg, then steps of -1

deg. Similarly, it can be observed that for an angle greater than -7 deg, the system loses the optical connection with a power loss greater than -30 dB. The difference between the negative and positive limits (i.e. -7 degrees and +6 deg) can be interpreted as, the centralized position of the OTM was at -1 deg, caused by an initial misalignment between the OTMs.

As a conclusion, the MEMS mirror was able to steer the laser beam coming from OTM₁ to inject it into the optical fiber for angular movements of the OTM₂ within a range of +/- 6 deg.

The next phase of the experiment consists in testing the MEMS block tracking system of OTM₂, by translating the latter module with respect to the fixed OTM₁. Figure 5.16 illustrates the variation in the optical power loss received in dB, with respect to the displacement realized by OTM₂.

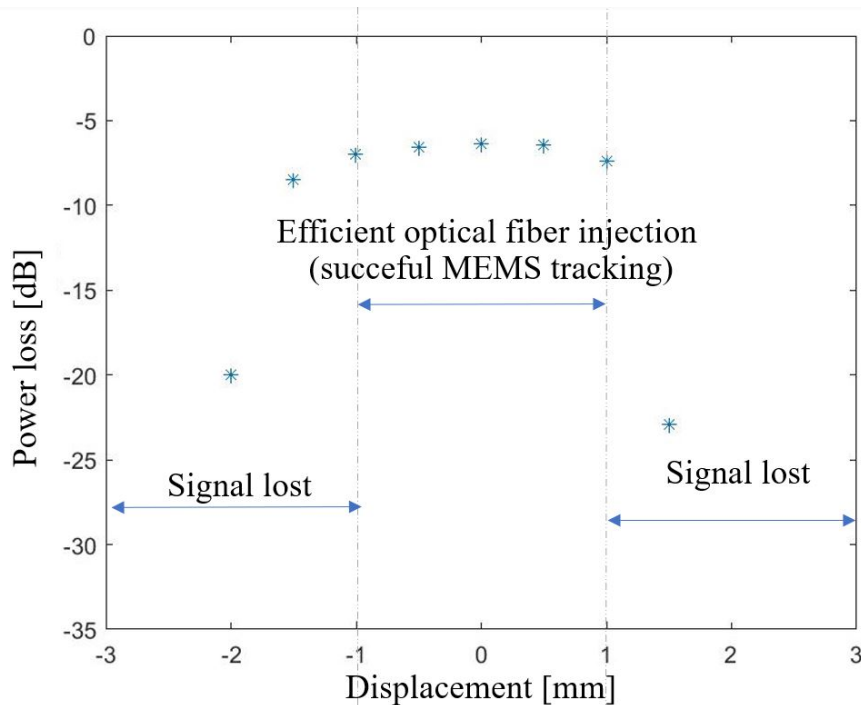


Figure 5.16: Measured output power loss in dB with respect to the displacement.

The optical measurement was taken on the output of optical fiber of the OTM₂. The system's initial position for 0 mm gives a power loss of -6.63 dB. The OTM₂ is manually translated in the positive direction, using the newport translation stage, with a step of 0.5 mm. The optical signal was lost for a displacement greater than 1mm giving a power loss greater than -25 dB. The same experiment for the translation in the negative direction was performed and it was observed that the optical signal was lost again in the optical fiber for a displacement greater than -1 mm. As a result, the MEMS mirror is able to correct an offset of the laser beam caused by the translation of the OTM₂ for a displacement range of +/-1 mm.

In the second setup, the same experimental work was repeated but with OTM₁ as the mobile emitter, and OTM₂ as the fixed transmitter. The fiber optic of OTM₂ was connected to a laser source, while the optical fiber of OTM₁ was connected to the photometer. The MEMS block of the OTM₁ was tested and validated to correct the angular and displacement variation of the entire module with respect to the OTM₂. In this way, our system was shown to be a bidirectional tracking communication system.

5.8 Conclusion

In this chapter, the description of the optical tracking module design and its closed-loop control were discussed. The two blocks of the OTM (MEMS block and telescope block) were presented and validated separately. The experimental test revealed that the telescope block was able to follow the movement of the laser in free-space. This was verified by maintaining the values of V_{B-T} and V_{L-R} of QPD₁ and QPD₂ close to zero even during laser movement. The MEMS block of the OTM module demonstrated its capability to correct small angles errors of +/-6 deg and sustain a constant laser beam injection into the optical fiber with -6.36 dB loss. Also, in a translation variation test, for a short range of +/-1 mm displacement variation, the OTM MEMS block is able to correct this displacement error. Outside these ranges, the telescope block will be in charge of tracking to maintain the LOS between the modules. Finally, by combining these two results, it can be concluded that the entire OTM system is functional.

Chapter 6

Conclusion

Main outcomes of the study

In this thesis, an optical remote method is presented to localize and track mobile targets moving over large spaces. The optical method is validated in this work for two applications: the first at the micro and the second at the macro scale. In the context of micro-factories the first application aims to localize and track micro-conveyors in order to monitor and control their displacement over a conveying surface. The second application aims to localize and track mobile systems to ensure a high bitrate wireless optical communication between them.

An electromagnetic conveying surface composed of 5×5 cells (dimension 15×15 cm) was adopted to test the first application to localize and track mobile micro-conveyors with high accuracy on the order of a tenth of μm . The movement of the micro-conveyor is based on Laplace force, between the supplied current injected into the coils of the surface and the permanent magnets distributed symmetrically over the micro-conveyor cross structure. The localization and tracking method is ensured by the interaction between a MEMS mirror and a quadrant photo-detector (QPD). A CCR is placed on the micro-conveyor, in order to obtain optical feedback of its position on the conveying surface. This is realized by reflecting the incident light coming from the MEMS mirror towards a QPD. The MEMS mirror steers the light beam coming from a fixed laser diode towards the conveying surface, in order to follow the displacement of the micro-conveyor. The orientation of the MEMS mirror is controlled in a closed loop system according to the QPD generated signals.

The first experimental test was performed to track a mobile micro-conveyor, in an open loop control, as seen in chapter 3. The micro-conveyor was tracked while moving in a horizontal and vertical path. The MEMS mirror orientation was controlled with a proportional regulator to keep the light spot centered on the photo-detector area with a CCR placed on the micro-conveyor. The MEMS

mirror was capable of tracking the micro-conveyor moving in complex trajectories and in all directions, where the micro-conveyor was moved by hand, due to the complexity to generate such paths in automatically. The limit velocity above which tracking no longer works was analyzed and experimentally measured to be 30 mm/s.

In chapter 4, experimental work was carried out to evaluate and test a closed loop tracking of the micro-conveyor with the conveying surface. A mandatory pre-use calibration of the conveying surface was realized based on the Homography principle. The purpose was to find the relation between the rotation angle of the MEMS mirror and the corresponding position of the laser illuminating the center of the micro-conveyor. In this exercise, the micro-conveyor only covered the functional region of the surface, i.e. the center 3×3 cells, which are linked to the current generators. As a result, only the region of interest composed of 3×3 cells was calibrated. The calibration consisted in calculating a matrix H obtained by acquiring n measurements of the coordinates in the conveying surface and the corresponding coordinates in the plane parallel to the MEMS mirror. The x , y coordinates in the conveying surface were measured using a camera placed above the surface. The field of view of the camera contains the zone of interest, i.e. the central 3×3 cells. For such a setup, the resolution of the camera system is equal to $45 \mu\text{m}/\text{pixel}$. The corresponding coordinates in the MEMS reference are calculated from the MEMS rotational angles, taking into account that these angles vary linearly according to the applied voltages sent to the MEMS driver. A study of the influence of these measurements on the accuracy of matrix H was carried out. Upon increasing the number n , the error between the measured and the recalculated points was reduced until reaching a limit of $n = 20 \times 20$. The average and root mean square of the distance error was equal to $267,4 \mu\text{m}$ and $159,4 \mu\text{m}/\text{pixel}$, respectively. The global homography method deploys a single homographic matrix to calibrate the 3×3 cell surface.

A local homography method was proposed to enhance the accuracy by configuring 9 matrices, each dedicated to the calibration of one cell. As a result, in order to calculate the coordinates of the micro-conveyor, the matrix H that corresponds to the cell on which the micro-conveyor is located is deployed.

With the local method average and root mean square of the error distance are reduced for each cell compared to the global homography results. The test of reducing the camera resolution to $20 \mu\text{m}/\text{pixel}$ in order to capture one cell, gives a similar result compared to the local homographic result with a camera having a $45 \mu\text{m}/\text{pixel}$ resolution. Thus, for the actual size we used and adopted the local homography method with a camera having a resolution of $45 \mu\text{m}/\text{pixel}$. However, if the zone of interest is expanded to include more cells, the camera then has to

move in order to cover the entire surface. In addition, new local homographies should be configured to maintain the same high accuracy. In experimentation, the global and local homography matrices were used to test and validate the closed loop tracking of the micro-conveyor. The step response on a horizontal path of 3 cm is determined by the maximum distance that could be travelled horizontally. Once the micro-conveyor reaches the desired position, a portion of 300 measurements for the error in the x-axis was analyzed to extract the average and root mean square errors that were found to be $24.2 \mu\text{m}$ and $18.1 \mu\text{m}$, respectively. Then to test the reliability of the system, a command was issued to make a round-trip trajectory on the conveying surface. The same experiment was repeated for the vertical y-axis, where the micro-conveyor traveled 3 cm vertically and 300 measurements resulted in average and root mean square errors equal to $31.4 \mu\text{m}$ and $22.8 \mu\text{m}$, respectively. Moreover, local homography was tested for a smaller version of the micro-conveyor used to perform a wider path on a scale of $5\text{cm} \times 5\text{cm}$ cells. The tracking system was able to track and adjust the trajectory of the micro-conveyor. The location and tracking of two micro-conveyors using a time multiplexing approach was also verified in this work. The trajectories of each micro-conveyor were reconstructed, each point of the path corresponding to one cycle of scanning. In fact, during one spiral scanning cycle, the MEMS mirror localizes the two micro-conveyors and records their position, in the next cycle the new position is recorded and so on, until the overall trajectory is obtained for each micro-conveyor.

The second application, of tracking two macro-scale terminals, was also evaluated and tested in this thesis. The two terminals work together in order to maintain an optical line of sight between them. Each terminal contains an optical tracking module (OTM) composed of two blocks: Pan-Tilt and MEMS block. The pan tilt block serves to correct a terminal's orientation for large angles variations during motion (coarse resolution), using two servo-motors controlled in a closed loop system with two QPDs. The MEMS block corrects small derivation angles and small translation variations by controlling a MEMS mirror in a closed loop signals form a third QPD. For simplicity each of the modules of mentioned above were tested and evaluated separately. The Pan Tilt block was tested to follow and track a mobile laser beam placed in front of it. Experimental work showed its capability to maintain the same LOS with the laser moving in 180 degrees in the pan and 180 degree over the tilt direction.

The MEMS block was tested by implementing two identical MEMS blocks facing each other. One acts as a fixed emitter and the second acts a mobile receiver, that receives the optical power to be injected into its optical fiber with a power loss of less than -6.36 dB.

The aim of the experimental work was to study the optical power budget of the system, during static evolution of angular and translation movements of the mobile module. The mobile OTM was able to correct the orientation of its integrated MEMS mirror to maintain laser beam injection into the optical fiber, while rotating the mobile OTM, with respect to the fixed OTM's axis, by an angular deviation of ± 6 degrees. In addition, it was capable of correcting errors during short translation variation tests of ± 1 mm displacement. As a result, by combining the mentioned results, the functionality of the complete OTM system could be deduced.

Perspectives

The first perspective of this work is to improve the resolution and speed of the closed loop by adapting a better corrector (e. g. a proportional-integral-derivative PID regulator) or by optimizing the number of local homographies to cover the entire conveying surface of conveying. In addition, optimization of the experimental set-up can would allow us to reduce the optical power loss and to find the best spot size for scanning the conveying surface. In order to increase the system capability to track micro-conveyors moving with a faster velocity, i.e increase the threshold velocity (V_{max}), where above this value the tracking is lost.

Another perspective is to locate and track more than two micro-conveyors. This will demand a larger conveying surface to handle a larger traffic. For a larger surface, the number of local homography zones would increase. The camera cannot have a field of view that covers the entire surface, with the sufficient resolution, thus it would have to be moved over the surface to calibrate each zone separately, to finally calibrate the entire surface. A study should also carried out on the number of micro-conveyors to be tracked by one MEMS membrane, since the system will be slowed when the number of micro-conveyors increases.

In addition, time multiplexing can be improved, by applying mathematical laws, such as kalman filter, to predict the new position of the micro-conveyor according to its previous position and velocity. In this case the new cycle of spiral scanning starts at the predicted point instead of the same origin point. Thus, the time of scanning reduces and tracking gets faster.

Frequency multiplexing is another possible approach to track multiple micro-conveyors. Several lasers of different wavelengths could be used and each micro-conveyor will carry an optical coated CCR to be treated for a single wavelength, which corresponds to one of the used lasers. Thus, each CCR has its own identification (ID) and can be tracked separately. In addition, each micro-conveyor would have a dedicated QPD and beam splitter. Under this condition, spectral filters should be placed in front of each QPD. The lasers can be combined using dichroic

mirrors in order to be directed to the MEMS mirror. In such a scenario, tracking would be based on continuously scanning the surface with a spiral pattern, as well as successively switching from one micro-conveyor to another to follow them. The perspective for macro scale application, presented in chapter 5, is to combine and test the Pan Tilt module and the MEMS block together by finding the center of gravity of the system and place it over the Pan Tilt axis. In addition, the implementation of a PID control of each module should accelerate the tracking and hence permit the fast and accurate alignment of the two systems.

List of publications

1. S. Malak, H. Al Hajjar, E. Dupont, M. U. Khan, C. Prella and F. Lamarque, "High resolution localization and tracking technique of a mobile micro-conveyor over a smart surface", journal IEEE/ASME Transactions on Mechatronics, In progress.
2. S. Malak, H. Al Hajjar, E. Dupont, M. U. Khan, C. Prella and F. Lamarque, "Closed loop tracking of a mobile micro conveyor over a smart surface", journal IEEE Sensors, In progress.
3. S. Malak, J.B. Lamour, E. Dupont, H. Al Hajjar, M.U. Khan, G. Nourdin, C. Prella, F. Lamarque and B. Fracasso, "Closed loop controlled optical tracking module for free-space optical communications", IEEE/ASME International Conference on Advanced Intelligent Mechatronics (AIM), Hong Kong, July 8-12, 2019.
4. S. Malak, H. Al Hajjar, E. Dupont, M. U. Khan and F. Lamarque, "Optical localization and open loop tracking of a microconveying system", IEEE/ASME International Conference on Advanced Intelligent Mechatronics (AIM), Auckland, New Zealand, July 9-12, 2018.
5. S. Malak, H. Al Hajjar, E. Dupont and F. Lamarque, "First approach of an optical localization and tracking method applied to a micro-conveying system", IEEE International Conference on Multisensor Fusion and Integration for Intelligent Systems, Daegu, Korea, November 16 - 18, 2017.
6. Saly Malak, Hani Al Hajjar, Erwan Dupont, Frédéric Lamarque, "High resolution optical localization and tracking method of mobile micro-conveyors over smart surface", International Symposium on Optomechatronic Technology 2017NCKU, Taiwan, November 06-08, 2017.

Bibliography

- [Agat 16] Y. Agata, J. Hong, and T. Ohtsuki. “Room-level proximity detection based on RSS of dual-band Wi-Fi signals”. In: *2016 IEEE International Conference on Communications (ICC)*, pp. 1–6, Kuala Lumpur, Malaysia, May 2016.
- [Al H 13] H. Al Hajjar, B. Fracasso, and D. Leroux. “Fiber-distributed indoor high bitrate optical wireless system”. *Wireless personal communications*, Vol. 72, No. 3, pp. 1771–1782, 2013.
- [Atsu 10] K. Atsuumi and M. Sano. “Indoor IR azimuth sensor using a linear polarizer”. In: *2010 International Conference on Indoor Positioning and Indoor Navigation*, pp. 1–5, IEEE, Zurich, Switzerland, 2010.
- [Bell 09] Y. Bellouard. *Microrobotics: methods and applications*. CRC Press, 2009.
- [Bhat 17] D. Bhatt, S. R. Babu, and H. S. Chudgar. “A novel approach towards utilizing Dempster Shafer fusion theory to enhance WiFi positioning system accuracy”. *Pervasive and Mobile Computing*, Vol. 37, pp. 115–123, 2017.
- [Boli 15] M. Bolic, M. Rostamian, and P. M. Djuric. “Proximity Detection with RFID: A Step Toward the Internet of Things”. *IEEE Pervasive Computing*, Vol. 14, No. 2, pp. 70–76, Apr 2015.
- [Bosc 16] M. Bosch-Mauchand, N. Arora, C. Prella, J. Daaboul, *et al.* “Electromagnetic modular Smart Surface architecture and control in a micro-factory context”. *Computers in Industry*, Vol. 81, pp. 152–170, 2016.
- [Bouc 16] K. Bouchard, R. Ramezani, and A. Naeim. “Features based proximity localization with Bluetooth emitters”. In: *2016 IEEE 7th Annual Ubiquitous Computing, Electronics & Mobile Communication Conference (UEMCON)*, pp. 1–5, IEEE, New York, NY, USA, 2016.

-
- [Bren 17] R. F. Brena, J. P. García-Vázquez, C. E. Galván-Tejada, D. Muñoz-Rodríguez, C. Vargas-Rosales, and J. Fangmeyer. “Evolution of indoor positioning technologies: A survey”. *Journal of Sensors*, Vol. 2017, 2017.
- [Chen 18] X. Chen, W. Zhong, C. Li, J. Fang, and F. Liu. “Development of a contactless air conveyor system for transporting and positioning planar objects”. *Micromachines*, Vol. 9, No. 10, p. 487, 2018.
- [Clar 16] L. Clark and B. Shirinzadeh. “Modeling of two-plate capacitive position sensing systems for high precision planar three DOF measurement”. *Precision Engineering*, Vol. 46, pp. 383–392, 2016.
- [Dabo 18] P. Dabove, V. Di Pietra, M. Piras, A. A. Jabbar, and S. A. Kazim. “Indoor positioning using Ultra-wide band (UWB) technologies: Positioning accuracies and sensors’ performances”. In: *2018 IEEE/ION Position, Location and Navigation Symposium (PLANS)*, pp. 175–184, Monterey, CA, USA, April 2018.
- [Dand 18] R. Dandoš, K. Mozdřeň, and H. Staňková. “A new control mark for photogrammetry and its localization from single image using computer vision”. *Computer Standards & Interfaces*, Vol. 56, pp. 41–48, 2018.
- [De S 15] C. W. De Silva. *Sensors and actuators: Engineering system instrumentation*. CRC Press, 2015.
- [Deak 12] G. Deak, K. Curran, and J. Condell. “A survey of active and passive indoor localisation systems”. *Computer Communications*, Vol. 35, No. 16, pp. 1939–1954, 2012.
- [Dubr 09] E. Dubrofsky. *Homography estimation*. Master’s thesis, THE UNIVERSITY OF BRITISH COLUMBIA, 2009.
- [Día 13] A. Díaz-Ramírez, F. N. Murrieta, J. A. Atempa, and F. A. Bonino. “Non-intrusive Tracking of Patients with Dementia Using a Wireless Sensor Network”. In: *2013 IEEE International Conference on Distributed Computing in Sensor Systems*, pp. 460–465, Cambridge, MA, USA, May 2013.
- [Edo 99] M. Edo, Y. Watanabe, O. Morita, H. Nakazawa, and E. Yonezawa. “Two-dimensional micro conveyor with integrated electrostatic actuators”. In: *Micro Electro Mechanical Systems, 1999. MEMS’99. Twelfth*
-

-
- IEEE International Conference on*, pp. 43–48, IEEE, Orlando, FL, USA, 1999.
- [Erog 15] Y. S. Eroglu, I. Guvenc, N. Pala, and M. Yuksel. “AOA-based localization and tracking in multi-element VLC systems”. In: *Wireless and Microwave Technology Conference (WAMICON), 2015 IEEE 16th Annual*, pp. 1–5, IEEE, Cocoa Beach, FL, USA, 2015.
- [Fari 13] Z. Farid, R. Nordin, and M. Ismail. “Recent advances in wireless indoor localization techniques and system”. *Journal of Computer Networks and Communications*, Vol. 2013, 2013.
- [Fuku 06] Y. Fukuta, Y.-A. Chapuis, Y. Mita, and H. Fujita. “Design, fabrication, and control of MEMS-based actuator arrays for air-flow distributed micromanipulation”. *Journal of Microelectromechanical Systems*, Vol. 15, No. 4, pp. 912–926, 2006.
- [Goze 12] B. A. Gozen and O. B. Ozdoganlar. “Design and evaluation of a mechanical nanomanufacturing system for nanomilling”. *Precision Engineering*, Vol. 36, No. 1, pp. 19–30, 2012.
- [Gozi 11] B. Gozick, K. P. Subbu, R. Dantu, and T. Maeshiro. “Magnetic maps for indoor navigation”. *IEEE Transactions on Instrumentation and Measurement*, Vol. 60, No. 12, pp. 3883–3891, 2011.
- [Grob 13] L. Grobe, A. Paraskevopoulos, J. Hilt, D. Schulz, F. Lassak, F. Hartlieb, C. Kottke, V. Jungnickel, and K.-D. Langer. “High-speed visible light communication systems”. *IEEE communications magazine*, Vol. 51, No. 12, pp. 60–66, 2013.
- [Guel 16] V. Guelpa, P. Sandoz, M. A. Vergara, C. Clévy, N. Le Fort-Piat, and G. J. Laurent. “2D visual micro-position measurement based on intertwined twin-scale patterns”. *Sensors and Actuators A: Physical*, Vol. 248, pp. 272–280, 2016.
- [Guel 17] V. Guelpa. *Mesure visuel de position par vision pour la microrobotique à l'aide de mires périodiques*. PhD thesis, Bourgogne Franche-Comté, 2017.
- [Guo 15] Z. Guo, Y. Tian, X. Liu, B. Shirinzadeh, F. Wang, and D. Zhang. “An inverse Prandtl–Ishlinskii model based decoupling control methodology for a 3-DOF flexure-based mechanism”. *Sensors and Actuators A: Physical*, Vol. 230, pp. 52–62, 2015.
-

-
- [Haus 10] D. Hauschildt and N. Kirchhof. “Advances in thermal infrared localization: Challenges and solutions”. In: *2010 International Conference on Indoor Positioning and Indoor Navigation*, pp. 1–8, IEEE, Zurich, Switzerland, 2010.
- [Holm 14] S. T. Holmström, U. Baran, and H. Urey. “MEMS laser scanners: A review”. *Journal of Microelectromechanical Systems*, Vol. 23, No. 2, pp. 259–275, 2014.
- [HS 5] “HS-5685MH High Voltage, High Torque, Metal Gear Digital Sport Servo”. Available at <https://hitecrd.com/products/servos/sport-servos/digital-sport-servos/hs-5685mh-high-torque-hv-metal-gear-servo-/product>.
- [Hu 16] Y. Hu, A. Vibhute, S. Foong, and G. S. Soh. “Autonomous docking of miniature spherical robots with an external 2D laser rangefinder”. In: *2016 IEEE Region 10 Conference (TENCON)*, pp. 3525–3529, Singapore, Singapore, Nov 2016.
- [Huan 09] C. Huang, C. Chiang, J. Chang, Y. Chou, Y. Hong, S. J. Hsu, W. Chu, and C. Chan. “Location-Aware Fall Detection System for Medical Care Quality Improvement”. In: *2009 Third International Conference on Multimedia and Ubiquitous Engineering*, pp. 477–480, Qingdao, China, June 2009.
- [Inc 16] M. Inc. “PicoAmp 4.6 User Guide”. November 2016. Available at <http://mirrorcletech.com/hva.html>.
- [Kamm 14] S. Kammoun, J.-B. Pothin, and J.-C. Cousin. “Principes et Challenges de la Localisation par Bluetooth”. *Les Journées Scientifiques*, pp. 117–121, 2014.
- [Khan 17] M. U. Khan, C. Prella, F. Lamarque, and S. Büttgenbach. “Design and Assessment of a Micropositioning System Driven by Electromagnetic Actuators”. *IEEE/ASME Transactions on Mechatronics*, Vol. 22, No. 1, pp. 551–560, 2017.
- [Koho 10] T. K. Kohoutek, R. Mautz, and A. Donaubaue. “Real-time indoor positioning using range imaging sensors”. *International Society for Optics and Photonics*, Vol. 7724, p. 77240K, 2010.
- [LAUR] G. LAURENT. *Contributions à la manipulation distribuée fluide et à la microrobotique référencée vision*. École nationale supérieure de mécanique et des microtechniques (ENSMM). HDR thesis, 2017.
-

-
- [Li 12a] B. Li, T. Gallagher, A. G. Dempster, and C. Rizos. “How feasible is the use of magnetic field alone for indoor positioning?”. In: *2012 International Conference on Indoor Positioning and Indoor Navigation (IPIN)*, pp. 1–9, IEEE, Sydney, NSW, Australia, 2012.
- [Li 12b] N. Li and B. Becerik-Gerber. “Assessment of a Smart Phone-Based Indoor Localization Solution for Improving Context Awareness in the Construction Industry”. In: *Congress on Computing in Civil Engineering*, Clearwater Beach, Florida, United States, 06 2012.
- [Li 14] L. Li, P. Hu, C. Peng, G. Shen, and F. Zhao. “Epsilon: A visible light based positioning system”. In: *11th USENIX Symposium on Networked Systems Design and Implementation (NSDI 14)*, pp. 331–343, Seattle, WA, USA, 01 2014.
- [Lian 13] J. Z. Liang, N. Corso, E. Turner, and A. Zakhor. “Image based localization in indoor environments”. In: *Computing for Geospatial Research and Application (COM. Geo), 2013 Fourth International Conference on*, pp. 70–75, IEEE, San Jose, CA, USA, 2013.
- [Liu 07] H. Liu, H. Darabi, P. Banerjee, and J. Liu. “Survey of wireless indoor positioning techniques and systems”. *IEEE Transactions on Systems, Man, and Cybernetics, Part C (Applications and Reviews)*, Vol. 37, No. 6, pp. 1067–1080, 2007.
- [Lu 11] Q. Lu, X. Zhang, and Y. Fan. “Micro-vision-based displacement measurement with high accuracy”. In: *Seventh International Symposium on Precision Engineering Measurements and Instrumentation*, p. 83210I, International Society for Optics and Photonics, Yunnan, China, 2011.
- [Magh 16] H. S. Maghdid, I. A. Lami, K. Z. Ghafour, and J. Lloret. “Seamless outdoors-indoors localization solutions on smartphones: implementation and challenges”. *ACM Computing Surveys (CSUR)*, Vol. 48, No. 4, p. 53, 2016.
- [Main 14] L. Mainetti, L. Patrono, and I. Sergi. “A survey on indoor positioning systems”. In: *Software, Telecommunications and Computer Networks (SoftCOM), 2014 22nd International Conference on*, pp. 111–120, IEEE, Split, Croatia, 2014.
- [Mala 17] S. Malak, H. Al Hajjar, E. Dupont, and F. Lamarque. “First approach of an optical localization and tracking method applied to a micro-
-

- conveying system”. In: *Multisensor Fusion and Integration for Intelligent Systems (MFI), 2017 IEEE International Conference on*, pp. 168–173, IEEE, Daegu, South Korea, 2017.
- [Mala 18] S. Malak, H. Al Hajjar, E. Dupont, M. Khan, and F. Lamarque. “Optical localization and open loop tracking of a micro-conveying system”. In: *2018 IEEE/ASME International Conference on Advanced Intelligent Mechatronics (AIM)*, pp. 322–327, IEEE, Auckland, New Zealand, 2018.
- [Mao 13] L. Mao, J. Chen, Z. Li, and D. Zhang. “Relative localization method of multiple micro robots based on simple sensors”. *International Journal of Advanced Robotic Systems*, Vol. 10, No. 2, p. 128, 2013.
- [Mart 15] F. Martinelli. “A robot localization system combining RSSI and phase shift in UHF-RFID signals”. *IEEE Transactions on Control Systems Technology*, Vol. 23, No. 5, pp. 1782–1796, 2015.
- [Mart 16] F. Martinelli. “Robot localization using the phase of passive UHF-RFID Signals Under Uncertain Tag Coordinates”. *Journal of Intelligent & Robotic Systems*, Vol. 82, No. 3-4, pp. 577–593, 2016.
- [Maut] R. Mautz. *Indoor positioning technologies*. ETH Zurich, Department of Civil, Environmental and Geomatic Engineering. Habilitation thesis, 2012.
- [Maut 11] R. Mautz and S. Tilch. “Survey of optical indoor positioning systems”. In: *2011 International Conference on Indoor Positioning and Indoor Navigation (IPIN)*, pp. 1–7, IEEE, Guimaraes, Portugal, 2011.
- [Medi 12] C. Medina, J. C. Segura, and S. Holm. “Feasibility of ultrasound positioning based on signal strength”. In: *2012 International Conference on Indoor Positioning and Indoor Navigation (IPIN)*, pp. 1–9, IEEE, Sydney, NSW, Australia, 2012.
- [MICR 16] MICROCHIP. “pic32”. 2016. Available at <http://www.microchip.com/wwwproducts/en/PIC32MZ2048EFH100>.
- [Mila 09] V. Milanovic. “Linearized gimbal-less two-axis MEMS mirrors”. In: *Optical Fiber Communication Conference*, p. JThA19, Optical Society of America, San Diego, California, United States, 2009.

-
- [Mila 13a] V. Milanović. “Device for optical imaging, tracking, and position measurement with a scanning MEMS mirror”. Apr. 23 2013. US Patent 8,427,657.
- [Mila 13b] V. Milanović and A. Kasturi. “Real-time 3D Tracking: The system “MEMSEye” can be used for optical 3D position and orientation measurement”. *Optik & Photonik*, Vol. 8, No. 4, pp. 55–59, 2013.
- [Mirz 12] R. Mirza, A. Tehseen, and A. V. Joshi Kumar. “An indoor navigation approach to aid the physically disabled people”. In: *2012 International Conference on Computing, Electronics and Electrical Technologies (ICCEET)*, pp. 979–983, Kumaracoil, India, March 2012.
- [Moda 10] M. Modabberifar, A. Yamamoto, and T. Higuchi. “An electrostatic induction actuator for dielectric sheet conveying”. In: *2010 IEEE/ASME International Conference on Advanced Intelligent Mechatronics*, pp. 551–556, Montreal, ON, Canada, July 2010.
- [Mogh 11] V. Moghtadaiee, A. G. Dempster, and S. Lim. “Indoor localization using FM radio signals: A fingerprinting approach”. In: *2011 International Conference on Indoor Positioning and Indoor Navigation*, pp. 1–7, IEEE, Guimaraes, Portugal, 2011.
- [Mont 16] R. Montoliu, J. Torres-Sospedra, and O. Belmonte. “Magnetic field based Indoor positioning using the Bag of Words paradigm”. In: *2016 International Conference on Indoor Positioning and Indoor Navigation (IPIN)*, pp. 1–7, IEEE, Alcalá de Henares, Spain, 2016.
- [Muff 10] M. Muffert, J. Siegemund, and W. Förstner. “The estimation of spatial positions by using an omnidirectional camera system”. In: *2nd International Conference on Machine Control & Guidance*, Bonn, Germany, 2010.
- [Mura 16] B. Muralikrishnan, S. Phillips, and D. Sawyer. “Laser trackers for large-scale dimensional metrology: A review”. *Precision Engineering*, Vol. 44, pp. 13–28, 2016.
- [MÄK 00] A. MÄKYNEN. *Position-sensitive devices and sensor systems for optical tracking and displacement sensing applications*. PhD thesis, Faculty of Technology, University of Oulu, Finland, 2000.
- [Naz 18] A. Naz, N. U. Hassan, M. A. Pasha, H. Asif, T. M. Jadoon, and C. Yuen. “Single LED ceiling lamp based indoor positioning system”. In: *Inter-*

-
- net of Things (WF-IoT)*, 2018 IEEE 4th World Forum on, pp. 682–687, IEEE, Singapore, Singapore, 2018.
- [Nguy 16] T.-S. Nguyen and T.-H. Huynh. “Experimental study of trilateration algorithms for ultrasound-based positioning system on QNX RTOS”. In: *Real-time Computing and Robotics (RCAR), IEEE International Conference on*, pp. 210–215, IEEE, Angkor Wat, Cambodia, 2016.
- [Njoy 17] A. N. Njoya, C. Thron, J. Barry, W. Abdou, E. Tonye, N. S. L. Konje, and A. Dipanda. “Efficient scalable sensor node placement algorithm for fixed target coverage applications of wireless sensor networks”. *IET Wireless Sensor Systems*, Vol. 7, No. 2, pp. 44–54, 2017.
- [PAF2] “PAF2-7C, Fiber port”. Available at <https://www.thorlabs.com/thorproduct.cfm?partnumber=PAF2-7C>.
- [Park 13] S. Park and H. Lee. “Self-Recognition of Vehicle Position Using UHF Passive RFID Tags”. *IEEE Transactions on Industrial Electronics*, Vol. 60, No. 1, pp. 226–234, Jan 2013.
- [Pole 18] K. Poletkin, A. Asadollahbaik, R. Kampmann, and J. Korvink. “Levitating micro-actuators: a review”. *Actuators*, Vol. 7, No. 2, p. 17, 2018.
- [Priy 00] N. B. Priyantha, A. Chakraborty, and H. Balakrishnan. “The cricket location-support system”. In: *Proceedings of the 6th annual international conference on Mobile computing and networking*, pp. 32–43, ACM, Boston, MA USA., 2000.
- [Quad] “Quad Sum and Difference Amplifier-Part Description QP50-6SD2”. Available at <https://www.first-sensor.com/en/products/optical-sensors/detectors/quadrant-pin-photodiodes-qp/>.
- [Raab 79] F. H. Raab, E. B. Blood, T. O. Steiner, and H. R. Jones. “Magnetic position and orientation tracking system”. *IEEE Transactions on Aerospace and Electronic systems*, Vol. AES-15, No. 5, pp. 709–718, 1979.
- [Saab 16] S. S. Saab and K. K. Saab. “A Positioning System for Photodiode Device Using Collocated LEDs”. *IEEE Photonics Journal*, Vol. 8, No. 5, pp. 1–14, Oct 2016.
- [Sakp 17] W. Sakpere, M. Adeyeye-Oshin, and N. B. Mlitwa. “A state-of-the-art survey of indoor positioning and navigation systems and technolo-
-

- gies”. *South African Computer Journal*, Vol. 29, No. 3, pp. 145–197, 2017.
- [Shar 17] R. Sharma, A. C. Kumari, M. Aggarwal, and S. Ahuja. “Performance analysis of LED based indoor VLC system under receiver mobility”. In: *2017 International Conference on Computing, Communication and Automation (ICCCA)*, pp. 945–950, Greater Noida, India, May 2017.
- [Shi 18a] Z. Shi, H. Al Hajjar, C. Prella, X. Liu, L. Ilou, and F. Lamarque. “Optimization of an optically controlled bistable micro-actuator”. In: *2018 IEEE/ASME International Conference on Advanced Intelligent Mechatronics (AIM)*, pp. 1148–1153, IEEE, Auckland, New Zealand, 2018.
- [Shi 18b] Z. Shi, B. Bélier, E. Martincic, L. Petit, J. Moulin, E. Lefeuvre, J. Terrien, C. Prella, and F. Lamarque. “Development of a 2D array of micro-machined electromagnetic digital actuators for micro-conveyance applications”. *Microsystem Technologies*, Vol. 24, No. 1, pp. 411–417, 2018.
- [SPT2] “SPT200H module by servoCity Corporation”. Available at <https://www.servocity.com/spt200>.
- [Stor 10] W. Storms, J. Shockley, and J. Raquet. “Magnetic field navigation in an indoor environment”. In: *2010 Ubiquitous Positioning Indoor Navigation and Location Based Service*, pp. 1–10, IEEE, Kirkkonummi, Finland, 2010.
- [Stre 06] D. L. Streiner and G. R. Norman. ““Precision” and “accuracy”: two terms that are neither”. *Journal of clinical epidemiology*, Vol. 59, No. 4, pp. 327–330, 2006.
- [Taja 18] F. Tajaddodianfar, S. R. Moheimani, J. Owen, and J. N. Randall. “On the effect of local barrier height in scanning tunneling microscopy: Measurement methods and control implications”. *Review of Scientific Instruments*, Vol. 89, No. 1, p. 013701, 2018.
- [Tana 01] M. Tanaka. “Development of desktop machining microfactory”. *Riken Review*, Vol. 34, 2001.
- [Tork 12] S. S. Torkestani, S. Sahuguede, A. Julien-Vergonjanne, and J.-P. Cancès. “Indoor optical wireless system dedicated to healthcare application in a hospital”. *IET communications*, Vol. 6, No. 5, pp. 541–547, 2012.

-
- [Tsai 17] Y.-T. Tsai, S.-C. Wang, K.-Q. Yan, and C.-M. Chang. “Precise positioning of marketing and behavior intentions of location-based mobile commerce in the internet of things”. *Symmetry*, Vol. 9, No. 8, p. 139, 2017.
- [Want 97] R. Want, A. Hopper, V. Falcao, and J. Gibbons. “The active badge location system”. *ACM Transactions on Information Systems*, Vol. 4, pp. 42–47, 1997.
- [Wood 10] O. J. Woodman and R. K. Harle. “Concurrent scheduling in the active bat location system”. In: *2010 8th IEEE International Conference on Pervasive Computing and Communications Workshops (PERCOM Workshops)*, pp. 431–437, IEEE, Mannheim, Germany, 2010.
- [Yan 10] Y. Yan, Z. Hu, X. Zhao, T. Sun, S. Dong, and X. Li. “Top-Down Nanomechanical Machining of Three-Dimensional Nanostructures by Atomic Force Microscopy”. *Small*, Vol. 6, No. 6, pp. 724–728, 2010.
- [Yang 13] P. Yang, W. Wu, M. Moniri, and C. C. Chibelushi. “Efficient object localization using sparsely distributed passive RFID tags”. *IEEE transactions on industrial electronics*, Vol. 60, No. 12, pp. 5914–5924, 2013.
- [Yasi 13] M. Yasir, S. Ho, and B. N. Vellambi. “Indoor localization using visible light and accelerometer”. In: *2013 IEEE Global Communications Conference (GLOBECOM)*, pp. 3341–3346, Atlanta, GA, USA, Dec 2013.
- [Yoha 18] A. Yohan, N.-W. Lo, and D. Winata. “An indoor positioning-based mobile payment system using Bluetooth low energy technology”. *Sensors*, Vol. 18, No. 4, p. 974, 2018.
- [Zafa 19] F. Zafari, A. Gkelias, and K. K. Leung. “A Survey of Indoor Localization Systems and Technologies”. *IEEE Communications Surveys Tutorials*, Vol. 21, No. 3, pp. 2568–2599, thirdquarter 2019.
- [Zeti 10] R. Zetik, G. Shen, and R. S. Thomä. “Evaluation of requirements for UWB localization systems in home-entertainment applications”. In: *2010 International Conference on Indoor Positioning and Indoor Navigation*, pp. 1–8, IEEE, Zurich, Switzerland, 2010.
- [Zhak 17] Z. Zhakypov, T. Uzunovic, A. O. Nergiz, E. A. Baran, E. Golubovic, and A. Sabanovic. “Modular and reconfigurable desktop microfactory for high precision manufacturing”. *The International Journal of Advanced Manufacturing Technology*, Vol. 90, No. 9-12, pp. 3749–3759, 2017.
-

-
- [Zhan 10] D. Zhang, F. Xia, Z. Yang, L. Yao, and W. Zhao. “Localization Technologies for Indoor Human Tracking”. In: *2010 5th International Conference on Future Information Technology*, pp. 1–6, Busan, South Korea, May 2010.
- [Zhan 17] C. Zhang, Y. Lu, S. Song, and M. Q.-H. Meng. “Shape tracking and navigation for continuum surgical robot based on magnetic tracking”. In: *2017 IEEE International Conference on Information and Automation (ICIA)*, pp. 1143–1149, IEEE, Macau, China, 2017.
- [Zhen 13] Y. Zheng, P. Li, N. Zhao, and Z. Hou. “Kinetics of molecular transitions with dynamic disorder in single-molecule pulling experiments”. *The Journal of chemical physics*, Vol. 138, No. 20, p. 05B616_1, 2013.
- [Zhu 15] L. Zhu, D. El-Baz, and H. Ning. “Survey on Air Levitation Conveyors with possible scalability properties”. In: *2015 IEEE 12th Intl Conf on Ubiquitous Intelligence and Computing and 2015 IEEE 12th Intl Conf on Autonomic and Trusted Computing and 2015 IEEE 15th Intl Conf on Scalable Computing and Communications and Its Associated Workshops (UIC-ATC-ScalCom)*, pp. 802–807, IEEE, Beijing, China, 2015.
- [Zhua 18] Y. Zhuang, L. Hua, L. Qi, J. Yang, P. Cao, Y. Cao, Y. Wu, J. Thompson, and H. Haas. “A survey of positioning systems using visible led lights”. *IEEE Communications Surveys & Tutorials*, Vol. 20, No. 3, pp. 1963–1988, 2018.